Controlling the Electromagnetic Properties of Magnetic Composites and Metamaterials

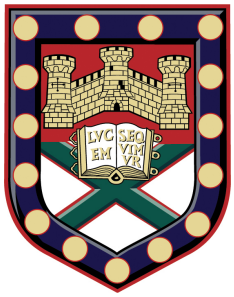

Laura Parke

School of Physics

University of Exeter

A thesis submitted for the degree of

Doctor of Philosophy in Physics

June 2015

Controlling the Electromagnetic Properties of Magnetic Composites and Metamaterials

Submitted by Laura Parke to the University of Exeter as a thesis for the degree of Doctor of Philosophy in Physics
June 2015

I certify that all material in this thesis which is not my own work has been identified and that no material has previously been submitted and approved for the award of a degree by this or any other University.

Laura Parke
June 2015

I would like to dedicate this thesis to my parents, Suzanne and Tim.

Acknowledgements

Firstly, I would like to thank my PhD supervisors Professor Roy Sambles, Professor Alastair Hibbins and Professor Ian Youngs.

Roy has been a hugely influential figure throughout my PhD. He has supported, inspired and certainly pushed me to reach my full potential. Alistair has been a fantastic supervisor who is very approachable and has put a huge amount of effort into making sure every piece of work is as good as it can be. Alistair has also been great company/entertainment on many QUEST outings and conferences, thank-you for making these such memorable experiences! I have had many useful and in-depth discussions about my work with my industry sponsor Ian Youngs, which have been so valuable. Ian has provided some fantastic ideas which have shaped the focus of my research.

I would like to thank Ian Hooper and Matt Lockyear for helping me so much through my PhD and for your hands on approach in the lab.

The day-to-day life as a PhD student would be empty without the following people;

Joe (Panda) has been by my side throughout my entire PhD. We have gone through a lot together; 12 QUEST trips, two trips to Austria, and Singapore! I am really going to miss my desk buddy. Although Rhiannon only joined the group in my third year, she became an instant friend, with the best sense of humor, I am going to miss her so much! Tom is a great friend and travel companion, thank-you for giving up your seat on that 12 hour plane ride and dedicating your sundays to watching Made In Chelsea with me. Pete, Ben, Gareth and Carl have made my PhD 'experience' incredibly sociable, they are all great fun. I will particularly remember the pub crawls and Synergy! Tim has been a source on endless support throughout my PhD. He has proof read every single chapter of my thesis, and has been a great friend. Thank-you Bug. Nina has been a great friend and has also helped me a huge amount with my work. Whether its proof reading or an SEM induction, Nina has always been there to help. Thank you Nina. Basement crew, namely Bug (Tim), Bug (Luke) and Bug (Ali)

have all made my time at Exeter great fun and I will miss them all. Previous PhD students who have all been great friends and very supportive include; Al, Simon, Nixon, Caz, Helen, Liz, and Celia. The QUEST project has been a big part of my PhD 'experience'. It has enabled me to collaborate, discuss my project with others in similar fields of research and meet some great people including. The technical workshop and Nick Cole in particular have tirelessly helped to make over 100 samples! There is no task too big for Nick, I'm sure I speak on behalf of all of us when I say the group could not function without you! Lastly, I would like to thank my family, my little sister Charlotte has been brilliant, and she always makes me laugh and my amazing Mum and Dad have supported me throughout my entire life.

Abstract

Ferrites are a class of magnetic oxides with superior electromagnetic (EM) properties at microwave frequencies when compared to conventional metallic magnetic materials for use in antenna miniturization and radar absorbers. Metamaterials are also a special group of materials, which are known to provide EM responses not found in nature due to subwavelength structuring. In this thesis, a range of ferrite composite materials and metamaterial structures are exploited to develop new methods for controlling permittivity and permeability up to 4 GHz with a view to producing high refractive index materials and to demonstrate broadband impedance matching to free space.

The first section of the thesis uses composites of powdered MnZn ferrite (as the filler) and PTFE (as the matrix), fabricated by a novel cold pressing technique, to produce composites for a range of volume fractions of MnZn ferrite (between 0-80% vol.). The EM properties for all composites were determined as a function of % vol. and the results were found to be in agreement with the Lichtenecker mixing formula. This study is the first convincing confirmation of the Lichtenecker mixing formula over a broad range of volume fractions (0-80% vol.). The cold pressing method was found to produce composites with reproducible EM properties, and was extended to use aluminium, barium titanate (as fillers) and also cellulose as an alternative matrix. Importantly, with regard to the study of cellulose composites, our work is the first to explore volume fractions of up to 85% and, the first to confirm the Lichtenecker mixing formula with these materials.

The ferrite particle size, as well as the volume fraction of ferrite, impacts the EM response of the composites. Both the permittivity and permeability increase as a function of ferrite particle size; however, the permeability increases at a much faster rate than the permittivity with particle size. It is shown that by controlling the ferrite particle size in conjunction with the volume fraction of ferrite, broadband impedance matching to free space can be realised for tailored values of refractive index. This is the first study that demonstrates independent control of the permittivity and permeability of ferrite composites by controlling the ferrite particle size. Alternatively, by adding a third component to the two part composite it is demonstrated

that broadband impedance matching to free space can also be realised with a refractive index of 16.1 (between 10-50 MHz). This is the first time, to the authors knowledge, that three part composites have been used to achieve high refractive index materials that are impedance matched to free space.

The second section of this thesis takes the concept of metamaterials to structure ferrite composite material with a further view to gain independent control over the permittivity and permeability. By tailoring the EM response of this metamaterial, which is comprised of anisotropic arrays of ferrite cubes, broadband impedance matching to free space is demonstrated. The refractive index over the impedance-matched frequency range is also very high (9.5). The metamaterial also acts as an excellent non-reflecting subwavelength thickness absorber up to 200 MHz. An analytical description of the permittivity and permeability dependence on the metamaterial parameters is developed to predict the EM response of this metamaterial, and of similar systems.

In the last part of this thesis, the concept of cubic metamaterials is extended to more complex metallic meta-atoms, where the permittivity and diamagnetic response of the metamaterial are independently tailored to demonstrate how the refractive index can be tuned over a broad frequency range. By understanding the role of individual cube parameters, the diamagnetic response can be controlled between near zero and unity, which greatly alters the refractive index. The results are the first experimental validation for showing 'design' control of the permittivity and permeability of these metamaterials via geometry tuning of the meta-atom design.

Contents

Contents

List of Figures

List of Figures

List of Tables

List of Tables

Chapter 1

Introduction

1.1 Aim of Research

The aim of the work presented in this thesis is to create artificial materials and composite structures with exotic electromagnetic (EM) properties for applications in the microwave regime. The magnetic composites and metamaterials designed posses properties such as being impedance matched to free space, having high refractive index as well as tunable EM properties to independently control the material's response to an externally electromagnetic field. The research fields of metamaterials and magnetic composites, specifically ferrite composites, are both relatively new. The concept of a metamaterial was first introduced in 1898 by J. C. Bose who researched materials with chiral properties [1]. Later the use of magnetic materials to control EM radiation came about with the creation of soft ferrites in the 1930's for commercial use in inductors, antennas and EM absorbers [2]. Although there have been many studies investigating the properties of ferrite composites on a theoretical and experimental basis, combining the concept of metamaterial structuring with conventional ferrimagnetic materials is less well researched. One topic covered in this thesis demonstrates broadband impedance matching of the metamaterial to free space by structuring magnetic composite material.

1.2 Outline of Thesis

1.2.1 Ferrimagnetic Materials

As ferrimagnetic materials are the main material investigated in experimental Chapters 3, 4 and 5, an overview of their electromagnetic properties is presented below.

In the 1930s, a group of researchers from the Tokyo Institute of Technology developed a class of magnetic oxides now commonly known as soft ferrites [3], however, it

was not until 1945 that J. L. Snoek succeeded in producing a soft ferrite for commercial applications [2]. Ferrites can be categorised into two distinct groups; those with a cubic crystal structure known as spinel ferrites, and those that possess a hexagonal crystal structure called hexaferrites. Spinel ferrites are a class of magnetic compound based on the chemical formula MFe_2O_4 where M is a divalent metal such as Nickel, Manganese, Zinc, Cobalt, Iron etc. [4]. Although magnetite, a naturally occurring mineral with the chemical formula Fe_2O_4 has been around for millions of years, its magnetic properties above a few kHz are poor [5] i.e. the permeability decreases rapidly to near unity in the kHz frequency range. In contrast, man-made spinel ferrites have superior electromagnetic properties that extend into the MHz frequency range allowing them to be used in electronic devices, radar absorbing materials, microwave antennas etc. The electromagnetic properties of ferrites, and indeed any material, are described in terms of complex permeability μ where $\mu = \mu' + i\mu''$ and permittivity ε where $\varepsilon = \varepsilon' + i\varepsilon''$. Spinel ferrites possess a high μ' value at DC and a cut-off frequency in the MHz frequency range (above which μ' falls to approximately 1) while the ε' value remains frequency independent and large from DC to the MHz frequency band. Such superior electromagnetic properties in the MHz frequency range are important for the development of communications systems and shielding devices.

1.2.2 Ferrites in composite and sintered form

Spinel ferrites in their powdered form are studied experimentally in Chapters 4, 5 and 6 and thus will be the focus of discussion for the next two subsections. Spinel ferrites can exist in 2 forms; bulk or powdered depending on the desired application. Bulk ferrite is a sintered piece of ferrite with a density of approximately 5 g/cm^3, and a real permeability of approximately 1000, but only up to a few MHz, which limits application. Powdered ferrite is the result of grinding the bulk ferrite down into a power. This ferrite powder is mixed with a matrix (usually a common plastic) to produce a ferrite composite. The DC permeability of these ferrite composites is linked to the frequency range over which this high permeability value may exist. Snoek's Law [6] describes this behavior, and states that there is an inverse relationship between the initial permeability and the cut-off frequency, i.e. the higher the permeability, the lower the frequency at which the permeability drops to near unity.

In Chapter 4, a new method for producing heavily loaded ferrite composites is introduced. It overcomes many of the problems with previous methods such as increasing the maximum ferrite loading to 80% vol. and allowing a single fabrication method to be used across all % vol. of ferrite (from 0 to 80%). A review of previous methods is outlined in the remainder of this subsection.

Powdered ferrites are often embedded in a polymer matrix e.g. Polytetrafluoroethylene (PTFE), Polyphenylene sulfide (PPS) or silicone elastomer to form solid samples. To produce low % vol. ferrite composites (below 50% vol.) ferrite powder is often set in a silicone elastomer by curing in a vacuum oven [7], however, this method can often be time consuming and if higher % vol. ferrite composites are required a different technique must be employed. Previous studies have used temperatures of approximately 350°C to melt PPS resin powder before mixing in the ferrite and compressing (at 1000 kg/cm^2) over a time period of 30 minutes [8], producing 75% vol. ferrite composite samples. Above this % vol., a sintering method proposed by Takanori [9] produces porous sintered ferrite sample when temperatures of approximately 1150°C are reached. Despite this range of techniques covering all % vols., they are often time consuming and require elevated temperatures. In Chapter 4, a cold pressing method for producing composite materials with 0-80 % vol. of filler is demonstrated, with the electromagnetic properties and densities of the final samples showing good reproducibility.

1.2.3 Controlling the electromagnetic properties of ferrite composites

Chapters 5 and 6 focus on the ability to independently tune the permittivity and permeability of ferrite based materials. The ability to control the electromagnetic properties of ferrite composites has been of great interest in recent years due to the prospect of broadband impedance matching to free space for applications such as antenna miniaturisation [10], as well as the ability to control the value of the refractive index at which the material is impedance matched. When matching of the complex wave impedance occurs at an interface between two different media, the reflection from the interface is zero, allowing for complete power transmission, which is achieved when μ and ε are equal. In general, ferrites do not have equal values of μ and ε, hence, modifications must be made to ferrite composites to achieve impedance matching. Varying the % vol. of the filler is a simple method of varying both μ and ε, however, this simple dilution rarely allows for independent control of the electromagnetic parameters, therefore further degrees of control of the EM properties must be found. In order to vary μ and ε independently, the chemical or physical structure of the ferrite must be altered. Previous studies have demonstrated that chemical doping, sintering conditions, the addition of a third component, filler particle size and shape as well as applying an external DC magnetic field all impact μ and ε differently, For example, in the case of chemical doping, Kong *et al.* independently controlled μ' of $Ni_{0.95x}Zn_xCo_{0.05}Mn_{0.02}$ ferrite epoxy composite by varying the proportion of zinc in the ferrite [11]. More recently, impedance matching has been achieved by controlling the sintering temperature of a NiCuZn ferrite [12]. Su *et al.* found that by utilising a 2 stage sintering process, equal-

ity of μ' and ε' at a value of 11.8 from 10 - 100 MHz was achieved. The effect of NiZn ferrite particle size as well as the addition of a third component (MnZn ferrite) have been studied in Chapter 5 to demonstrate independent control of the EM properties of NiZn ferrite composites. Rather than achieving impedance matching using ferrite composite materials, metamaterial structuring is utilised in Chapter 6 to independently control the EM properties of a simple MnZn ferrite-PTFE composite material. Structuring the composite into anisotropically spaced cubic elements, arranged in an array, provides a method for independently controlling the electromagnetic properties of any magnetic/dielectric material. The analytical description of this type of structuring reveals strong and weak permeability/permittivity dependencies on the metamaterial dimensions depending on the polarisation of the incident EM radiation.

1.2.4 Predicting the electromagnetic response of composite materials

Chapters 4 and 5 utilise the Lichtenecker mixing formula to predict the EM response of NiZn ferrite and MnZn ferrite composites, hence, this section aims to provide a background to the concept of mixing laws. The complex permittivity and permeability of composite materials can be predicted by applying effective medium approximations known as EMA's or mixing laws. There are a large number of mixing laws that have been proposed with reviews in the literature including the Maxwell-Garnett approximation, Bruggeman effective medium theory and the Lichtenecker mixing law, all of which attempt to describe the macroscopic properties of composites [13–16] with each being more or less accurate depending on the parameters of the composite. All mixing laws use information about each individual component e.g. initially permittivity/conductivity or permeability as well as the % vol. of each component, to predict the electromagnetic response of the composite. The Maxwell-Garnett approximation, first published in 1905, describes two-phase mixtures using the assumption that the sample is isotropic with a permittivity/permeability value that does not vary with frequency, the inclusions must also be small compared to the wavelength and separated by distances greater than their size [17]. The concentration of the inclusions (if conducting) must also be below the percolation threshold [18]. Due to the assumption that individual inclusions do not interact with each other, many comparisons drawn between this mixing law and experimental data have concluded that the Maxwell-Garnett approximation under predicts the permittivity or permeability of the composite, especially at higher loadings (above approximately 30 % vol.) [19, 20]. In this approximate model, one of the components is treated as the environment (usually the matrix) with the filler described as a perturbation from the background environment. The first big progression on from the Maxwell-Garnett approximation was taken in the 1930s by Bruggeman

who proposed a new way of describing heterogeneous media that was markedly different from previous studies. In the Bruggeman model, the matrix and filler are not separated [21]. The combined matrix and filler are the homogeneous background medium against which polarisations are measured, however, there are still a set of assumptions made about the composite e.g. the geometry is assumed to be spherical with absolute equality between the phases in the mixture. In Chapters 4 and 5, the Lichtenecker mixing law is used as the analytical fit to experimental data for MnZn and NiZn ferrite composites of varied % vol. of filler from 10 to 80. The Lichtenecker mixing law is a special case of a more general group of mixing laws known as power laws. These laws use a certain power of the permittivity/permeability that is averaged based on the % vol. of each component, this constant power is denoted β. In the case of Birchak's formula, the power is equal to a $\frac{1}{2}$ thus the square root of each permittivity (from the host and filler) sum to the square root of the composite permittivity [22]. The power used in the Lichtenecker mixing formula is 0, instead this formula is a weighted average of the natural logarithms of the permittivity which predicts an exponential rise of the effective permittivity with increasing % vol. of filler [23]. Full descriptions of the Maxwell-Garnett and Lichtenecker mixing laws are presented in the following chapter (Chapter 2).

1.2.5 Metamaterials

Chapters 6 and 7 both use the concept of metamaterials as a method for achieving high refractive index and impedance matched materials. Metamaterials are artificially created structures where the electromagnetic properties are dictated by geometry in addition to the composition of the material [24–26]. Such materials are comprised of pseudo-atoms arranged such that the interaction between individual atoms with the incident electric and magnetic field provide values of complex permeability and complex permittivity not found in nature. This has led to the creation of metamaterials with exotic properties such as negative refractive index [24, 27] and ultra-high refractive index [28], as well as metamaterials that possess a high refractive index whilst being impedance matched to free space [29]. Methods for realising phenomena such as negative refraction rely on resonances within the system and hence are narrow-band and lossy [24]. In comparison, metamaterials with a high refractive index can be realised over a broad frequency range [28] as well as being low-loss making their electromagnetic properties desirable for the creation of graded-index devices such as electromagnetic cloaks [30]. As previously mentioned, Chapter 6 applies the concept of metamaterial structuring to ferrite composite material to achieve broadband impedance matching to free space whilst maintaining a high refractive index. Chapter 7 uses a similar metama-

terial design to independently control the permittivity and permeability of structured copper cube arrays. Both metamaterial designs allow for independent control of the permittivity and permeability, however, in Chapter 7, as the metamaterial is comprised of metallic elements, the permeability is controlled between near 0 and unity.

Chapter 2

Background

2.1 Introduction

The purpose of this chapter is to discuss in depth some of the fundamental physics that underpin the electromagnetic response of the materials studied in this thesis. The first part of this chapter provides an introduction to the three main types of magnetism, a detailed description of ferrimagnetic materials (ferrites) including their crystal structure, chemical composition, magnetic properties, dielectric properties and frequency dependent electromagnetic (EM) properties is presented. Mixing laws are used to predict the EM properties of composite materials in subsequent experimental chapters, therefore a discussion of the Claussius-Mossotti relation, Maxwell-Garnet mixing formula and the Lichtenecker mixing formula are the focus of the second part of this chapter. The last section of this chapter introduces the Nicholson-Ross-Weir (NRW) extraction method for converting the complex reflection and transmission amplitude co-efficients to complex permittivity and pemeability, which is utilised in subsequent experimental chapters to deduce the EM properties of bulk materials and metamaterials.

2.2 Types of Magnetism

All materials can be broadly divided into three main categories depending on their magnetic properties; diamagnetic, paramagnetic or ferromagnetic. Permanent magnets i.e. ferromagnets can be also be subdivided into either ferromagnets, anitferromagnets or ferrimagnets depending on the interactions between magnetic moments as well as the interaction between the electrons with their crystal lattice.

2.2.1 Diamagnetism

The magnetic field induced within diamagnetic materials is in a direction opposite to the externally applied magnetic field. Diamagnetism is caused only by the orbital motion of electrons which create atomic current loops. These currents produce a magnetic field that opposes the applied magnetic field [31]. All materials have a diamagnetic response, however, in the case of ferromagnets, when there is a net magnetic moment or paramagnets, when there is some long range ordering of the magnetic moments, the diamagnetic contribution is negligible is size. Diamagnetic materials with a large diamagnetic response in the presence of an external magnetic field such as water, carbon, superconductors, mercury and bismuth possess a relative real permeability which is greater than 0 and less than unity [32].

2.2.2 Paramagnetism

In contrast to diamagnetic materials, paramagnetic materials contain unpaired electrons which are able to realign in the applied magnetic field associated with each unpaired electron orbital. While in ferromagnetic materials the magnetic moments interact to produce a net magnetic dipole moment in the absence of an external field, the magnetic moments in paramagnets do not interact and are randomly oriented. Although these dipoles can be aligned with the application of an external magnetic field, the remenance of a paramagnet is 0. Paramagnetic materials such as lithium, sodium, magnesium and aluminium possess a relative real permeability that is greater than or equal to unity ($\mu' \geq 1$) [32]. It should be noted that above a ferromagnetic material's Curie temperature, the material becomes paramagnetic, this transition is also be observed in antiferromagnets above the Néel temperature. Such elevated temperatures mean that the thermal energy supplied to the material is greater than the interaction energy between individual electron spins [33].

2.2.3 Ferromagnetism

Ferromagnetism is a form of permanent magnetism. The spontaneous alignment of the material's magnetic dipole moments produce a net magnetic dipole moment without the application of an external magnetic field. For a material to be ferromagnetic, an interaction must exist between electron spins which acts to align the electron spins. This phenomenon is known as the exchange interaction and is a result of orbitals of unpaired valence electrons from different atoms overlapping, thus distorting the electron cloud charge distribution. The distortions allow for the electrons to move further apart from each other by aligning their spins parallel, thereby decreasing the electrostatic

repulsion. The energy difference between aligning spins parallel to anti-parallel is the exchange energy. It is important to note that the exchange interaction is not the only contribution to a material's magnetic properties. Magnetic anisotropy, which is discussed in greater depth later in this chapter, is also another important property of magnetic materials since it is responsible for aligning the electron spins in a preferential direction.

2.2.4 Antiferromagnetism and Ferrimagnetism

Both antiferromagnetism and ferrimagnetism are forms of permanent magnetism that rely on long range interactions between neighbouring spins, and magnetic anisotropy. For both phenomena, neighbouring magnetic moments sit on two different lattice sites and point in opposite directions. In the case of antiferromagnetism, without application of an external magnetic field, the net magnetisation is zero since there is complete cancellation of the magnetic moments on the two different lattice sites. However, in the case of ferrimagnetism, the magnetic moments of the two different lattice sites do not cancel, hence, there is a net magnetisation. Ferrites are a common type of ferrimagnetic material, which can be naturally occurring in the case of magnetite, or man-made in the case of manganese-zinc ferrite. Although ferrites only possess a small saturation magnetisation (the magnitude of an applied magnetic field required to align all the magnetic dipoles) compared to ferromagnets, their resistivity at DC is three orders of magnitude larger due to insulating oxide barriers that significantly reduce eddy current losses. Ferrites are manufactured in specific sintering conditions whereby certain amounts of impurities are added, such as CaO to control grain growth and the width of the grain boundary layers (that separate grains) to increase resistivity and decrease the diamagnetic response of the ferrite by reducing eddy currents. These grain boundary layers inhibit the electron hopping process between grains As ferrimagnets (specifically inverse spinel ferrites such as MnZn ferrite and NiZn ferrite) are the focus of Chapters 4, 5, and 6, their microstructure, crystal structure and electromagnetic properties will be discussed in the following sections.

2.3 Spinel Ferrites

This section discusses the microstructure, crystal structure, magnetic and dielectric properties of ferrimagnetic materials. Ferrites can be separated into three different categories depending on their crystal structure and chemical composition. These are spinel ferrites, garnets and hexagonal ferrites. Spinel ferrites are the focus of this chapter since they are studied experimentally in subsequent chapters.

2.3.1 Manufacture of Ferrites

Ferrites can be sourced in either pre-sintered powder form, sintered-bulk form or sintered-powdered form. There are different sintering processes used, which depend on the desired final properties. The purpose of sintering is to: 1) complete the inter-diffusion of metal ions into the desired crystal structure, 2) to establish the valency of ions by proper oxygen control, and 3) develop the micro-structure most appropriate for the application. Once sintered, the bulk ferrite is ball-milled down to a powder, which then can be incorporated into a matrix material to form a ferrite composite. In subsequent experimental chapters, sintered-powdered ferrite used to form ferrite composites.

2.3.2 Inverse and Normal Spinel Structure

The normal spinel structure consists of cubic close-packed oxides with double the number of octahedral sites than tetrahedral sites per unit cell. Trivalent metal ions occupy half the octahedral holes, and divalent ions occupy one-eighth of the tetrahedral holes. Zinc ferrite is an example of a normal spinel ferrite, the tetrahedral sites, are occupied by zinc (Zn^{2+}) ions, which have no unpaired electron spins and hence does not produce antiferromagnetic ordering. The Fe^{2+} ions in zinc ferrite occupy octahedral sites, however, they do not interact strongly as the B-O-B interaction is very weak. This type of arrangement of ions means that zinc ferrite is not ferrimagnetic as there is not a net magnetic moment or antiferromagnetic ordering.

In an inverse spinel structure have a different distribution of ions when compared to the normal spinel structure, all of the divalent ions and half of the trivalent ions occupy octahedral sites, while the other half of the trivalent ions occupy tetrahedral sites. Nickel ferrite possesses an inverse spinel structure and contains trivalent ions which preferred to sit on tetrahedral sites. In the case of Ni ferrite, the Fe^{3+} ions preferentially fill the tetrahedral sites first, then fill the octahedral sites second (there is only room for half of the 16 Fe^{3+} ions at tetrahedral sites). The remaining 8 Fe^{3+} ions along with the 8 Ni^{++} ions sit at octahedral sites. The 8 Fe^{3+} ions at tetrahedral sites cancel exactly with the 8 Fe^{3+} ions at octahedral sites, meaning that the 8 Ni^{2+} ions on octahedral sites are unpaired and give rise to net magnetic moment.

More complicated configurations, such as nickel zinc ferrite, also possess an inverse spinel structure and have a net magnetic moment that is dominated by the positions of the nickel and zinc. Unlike zinc ferrite, the presence of the nickel ions (Ni^{2+}) at octahedral sites provides the net magnetic moment (as the Fe^{3+} ions on tetrahedral and octahedral sites once again cancel). [34–36].

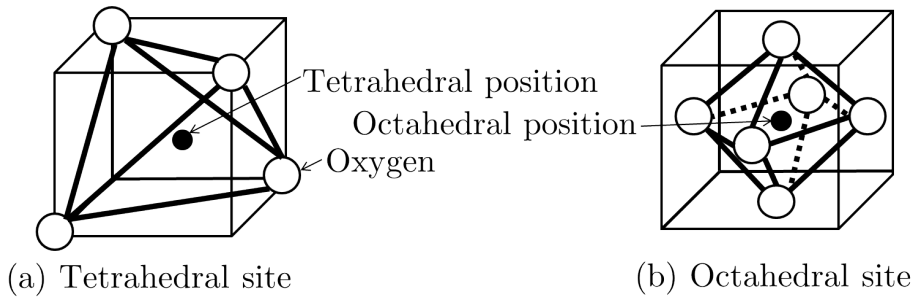

Figure 2.1: (a) the position of a metal ion at a tetrahedral site and (b) the position of a metal ion at an octahedral site.

2.3.3 Crystal Structure of Spinel Ferrites

As introduced previously, spinel ferrites have the chemical formula MFe_2O_4 (where M is a divalent metal). The oxygen ions form a cubic close packed arrangement while the metal ions sit amongst the oxygen ions. This is possible because the oxygen ionic radius (approximately 1.3 Å) is far bigger than the metal ionic radius (approximately 0.7 Å). The positions of the metal ions are either at tetrahedral or octahedral sites as shown in Figure 2.1.

The unit cell is comprised of 32 oxygen ions and 24 metal ions, which are positioned at either tetrahedral or octahedral sites. The reason for the two different types of site is due to the interstices between layers of oxygen not being the same; tetrahedral sites have 4 nearest neighbouring oxygen ions with the positions of these 4 oxygen ions forming a tetrahedron. Octahedral sites have 6 nearest neighbouring oxygen ions with the positions of the 6 oxygen ions forming an octahedron. There are 64 tetrahedral and 32 octahedral sites per unit cell, however, these sites are not necessarily all filled, in fact only 8 tetrahedral and 16 octahedral sites are occupied by metal ions [2]. The site preference of certain metal ions is determined by their ionic radius, as octahedral sites (approximately 70 Å) are larger than tetrahedral sites (approximately 66 Å), and the specific electron configuration [37]. Figure 2.2 is included for clarity and shows a schematic of the whole unit cell of a cubic lattice typical of spinel ferrites. The green spheres represent oxygen, the pink spheres are ions on tetrahedral sites and the purple spheres are ions on octahedral sites. Note that ions are only drawn in 2 of the 8 octants.

2.3.4 Crystal structure of Hexagonal Ferrites

Hexaferrites, developed during the 1930s, are commonly based on strontium or barium and possess the chemical formula $SrFe_{12}O_{19}$ (strontium ferrite) or $BaFe_{12}O_{19}$ (barium ferrite) [39]. They are classified into 4 main groups; M, Z, W and Y-types

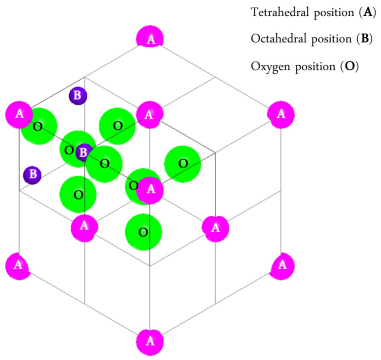

Figure 2.2: Unit cell of a cubic lattice typical of spinel ferrites. The green spheres represent oxygen, the pink spheres are ions on tetrahedral sites and the purple spheres are ions on octahedral sites. Note that ions are only drawn in 2 of the 8 octants. This figure is modified from [38].

depending on the ordering of the crystal layers and the concentration of the metal and oxygen ions in each of these layers. In contrast to spinel ferrites, hexaferrites have a lower permeability value at DC, however, the frequency range over which this permeability value extends is much higher in comparison to spinel ferrites and usually occurring within the GHz frequency band as described by Snoek's law. It should be noted that hexagonal ferrites are not investigated in this thesis and thus no detailed information is provided.

2.4 Properties of Spinel Ferrites

2.4.1 Domain Walls

Ferrites are composed of domain that are separated by domain walls. Within each domain, the magnetic moments are aligned, however, the magnetic moments in different domains are not necessarily aligned. The role of the domain wall is to provide a transition between different directions of magnetic moments in neighbouring domains. Within the domain wall, the magnetic moments reorientation gradually across a finite distance (dependent on the anisotropy of the material) equal to approximately 100-150 Å. Within the domain wall, the magnetic moments undergo an angular displacement of 180° or 90° depending on if the wall is a 3D Bloch wall (Figure 2.3(a)) or a 2D Néel wall (Figure 2.3(b)).

2.4.2 Formation of Domains

Domains are formed in ferrites to reduce the internal energy of the system. Within each domain the atomic moments are aligned such that there is a net magnetisation

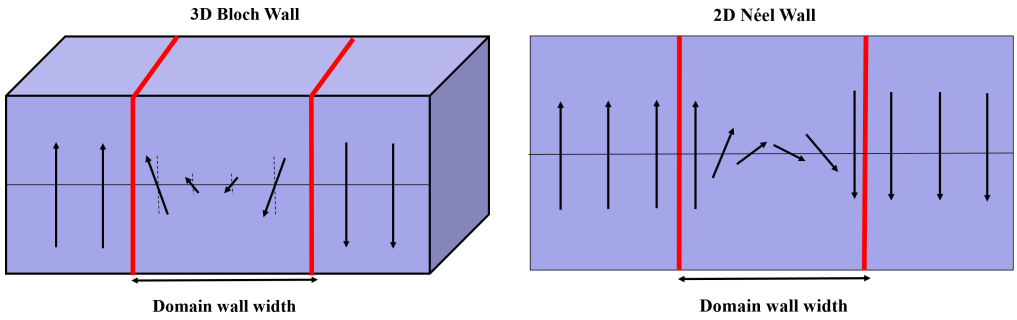

(a) (b)

Figure 2.3: Schematic of the two possible domain walls. (a) A 3D Bloch wall that switches the magnetic moments within the wall by 180° and (b) a 2D Néel wall that switches the magnetic moments within the wall by 90°.

and hence each domain can be considered a magnet with a 'north' and 'south' pole connected by flux lines. For a single domain particle, the flux lines extend outside the particle, which can become energetically unfavorable as the domain increases in size (see Figure 2.4(a)). This energy is known as the magnetostatic energy and is the magnetic potential energy contained in the field lines. A reduction of the length of the flux path can be achieved by splitting the single domain into two domains with associated net magnetic moments pointing anti-parallel to each other. Dividing the domain into n number of smaller domains decreases the magnetostatic energy to $1/n$ of the original single domain magnetostatic energy as shown in Figure 2.4. However, there comes a point where the energy cost of forming domain boundaries is greater than the magnetostatic energy change [40]. Although the splitting of domains reduces the magnetostatic energy, the associated magnetic dipole moments in adjacent domains are no longer aligned with each other, which increases the exchange energy. The exchange interaction acts to align magnetic dipoles parallel to each other as this minimises the exchange energy and forcing adjacent dipoles to point in different directions requires energy. Therefore the splitting of domains is energetically unfavorable when considering the exchange energy [41]. As the domains get smaller, the net energy saved by splitting decreases until the energy cost of creating an additional domain equals the field energy saved. In most materials the domain structure becomes stable when the individual domains are approximately between 10^{-4} and 10^{-6} m [42].

It is not just the magnetostatic energy and exchange energy that dictate the size and shape of the domains, there are three further energies to consider. These are outlined in the following subsections.

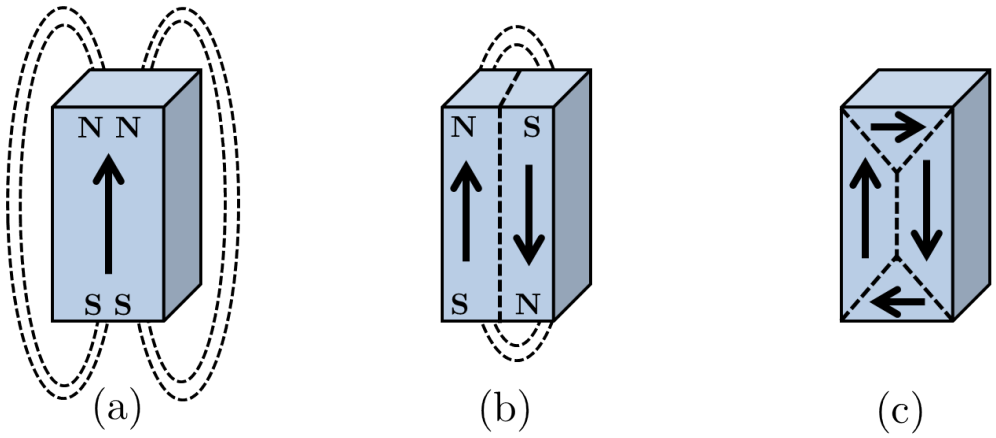

Figure 2.4: (a) A particle formed a single domain with lines of magnetic flux extending beyond the particle, (b) a particle formed of two domains to reduce the magnetostatic energy, and, (c) a single particle that has a completely closed domain structure and hence the magnetostatic energy has been eliminated.

2.4.3 Magnetocrystalline Anisotropy Energy

All permanent magnets are magnetically anisotropic i.e. they are easier to magnetise in certain directions than in others, these directions are referred to as the easy and hard axes of a crystal. The magnetocrystalline anisotropy energy is defined as the magnetostatic work done to rotate the net magnetic moment from the easy to the hard axis, and the field required to do this is known as the anisotropy field. The origin of the magnetocrystalline anisotropy arises from the interaction between the orbital motion of the electrons associated with individual ions and the crystal electric field (the crystal electric field is derived from neighbouring atoms in the crystal [43]). A single ion does not have a preferred direction to be magnetised in, however, introducing ions into the surrounding neighbourhood leads to the interaction of neighbouring ions and a preferred axis of magnetisation is established. The crystal structure dictates the easy and hard directions of magnetisation. For body centered cubic (bcc) Iron, the easy axis is in the [1,0,0] direction and the hard axis is in the [1,1,0] direction whereas in face centered cubic (fcc) nickel, the easy axis is in the [1,1,0] direction and the hard axis is in the [1,0,0] direction.

2.4.4 Magnetostrictive Energy

When a ferromagnet is placed in an external magnetic field, the domain walls move, the domains rotate and the material's dimensions are altered. This can either be an isotropic change in the material's dimensions (a volume change) or an anisotropic change in the material's dimensions (a change in the material's shape whilst maintaining

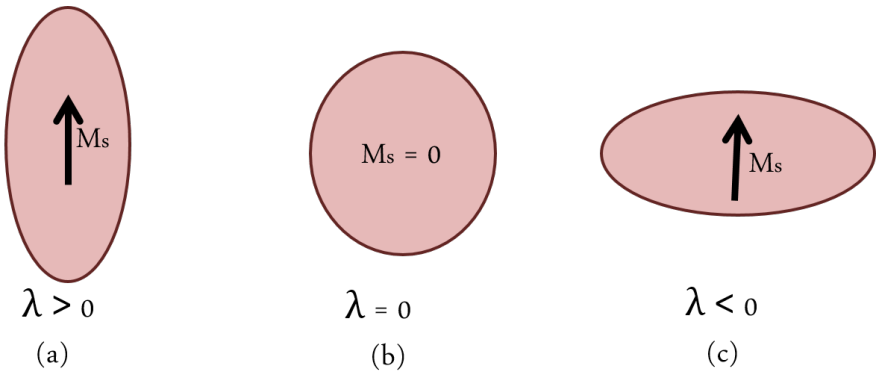

Figure 2.5: (a) A magnetic material expanding in the direction of the applied magnetic field (λ is positive), (b) a magnetic material in the absence of an applied magnetic field has a λ value of 0, and, (c) a magnetic material shrinking in the direction of the applied magnetic field (λ is negative).

a constant volume), however, the shape magnetostriction dominates and is far larger than the volume magnetostriction. The shape magnetostriction factor is the ratio between the change in the shape (δl) and the original unmagnetised shape (l) [43]:

$$\lambda = \frac{\delta l}{l}, \tag{2.1}$$

λ can be positive or negative depending on how the shape of the material distorts under the application of the applied magnetic field. If the material expands in the direction of the applied magnetic field, λ is positive. If the material shrinks in the direction of the applied magnetic field, λ is negative. These conditions are depicted in Figure 2.5.

2.4.5 Exchange Energy and Interactions

Ferromagnetic and antiferromagnetic materials all rely on a form of the exchange interaction to allow individual magnetic moments to couple together to form long range magnetic order to produce permanent magnetism. As electrons are fermions, the wave function describing two electrons has to be antisymmetric when two particles are exchanged. If two electrons are both spin up, the spatial part of the wave function must be antisymmetric. An antisymmetric wave function means that these two electrons have zero probability to be at the same place.The distribution of charge in space when the electrons have parallel spins are further apart than when antiparallel hence the parallel-aligned spin state is in lower energy (coulomb repulsion) than the antiparallel state. For simplicity, by considering the total energy of a system containing two

adjacent atoms, the expression is as follows;

$$E = E_1 + E_2 + Q + J_{\mathrm{EX}} \tag{2.2}$$

where E_1 and E_2 are the electron energies for each of the two individual atoms, Q is the electrostatic coulomb repulsion energy and J_{EX} is the exchange energy when the two electrons are indistinguishable i.e. when an electron associated with nucleus '1' orbits nucleus '2' and vice versa. The sign of J_{EX} is dependent on whether the spins align parallel or antiparallel, and will result in the material being either ferromagnetic or antiferromagnetic.

2.4.6 Indirect Exchange Energy and Interactions

Many ionic solids, including ferrites and some antiferromagnetic materials such as MnO rely on an indirect exchange (or superexchange) coupling mechanism that exists over relatively large distances [44]. As the magnetic ions in such materials are separated by non-magnetic ions, the short-ranged direct exchange interaction is not sufficient for producing the magnetic ordering is observed. As previously discussed in this chapter, the metallic ions sit on two different sub-lattices with the magnetic moments on each sub-lattice pointing in opposite direction. There are three different interactions that exist between these two lattice sites denoted A and B, which are; A-A, B-B and A-B interactions. The strength of each of these interactions is dictated by the distance between the two metal ions and the intermediate oxygen atom, as well as the angle subtended between them. The interaction between ions is strongest when the angle formed by the three ion system is 180° and when the inter-atomic distance between ions is minimised [2]. As the ions can only exist in specific locations in a lattice, there are only a finite number of configurations for the ions.

Figure 2.6 shows the inter-atomic distances and angles between the lines joining two metal ions and the intermediate oxygen ion for the three possible types of interaction. The best combination of distances and angles is found in the two possible AB interactions, for angles between ions of 125° and 154° [45].

2.4.7 Domain Wall Energy

As discussed earlier in this chapter, domain walls are regions where the direction of the magnetisation vector gradually switches direction to accommodate for two adjacent domains of differing directions of magnetisation. The energy of a domain wall is the difference between the magnetic moments before and after the domain wall was created, and is expressed as energy per unit wall area.The thickness of the domain wall is

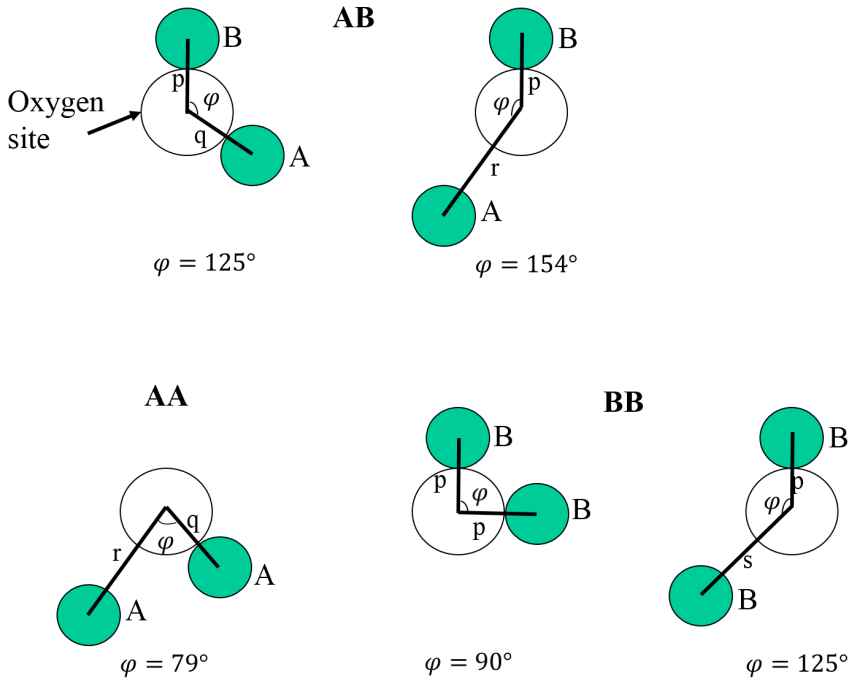

Figure 2.6: Schematic of inter-ionic distances and angles in a ferrite for the three different types of lattice site interaction [5]. Here, A and B denote the two different lattice sites where the metal ions sit (tetrahedral and octahedral respectively.) and p, q, r and s are corresponding between distances between different lattice sits (A-B, A-A and B-B.)

dictated by a trade-off between two different energy contributions; the exchange energy and the magnetocrystalline anisotropy energy. A thick wall, where the direction of magnetisation varies slowly as a function of distance, minimises the exchange energy as the exchange energy acts to keep magnetic moments parallel (as shown in Figure 2.7(a)). However, if the domain walls are thick, the magnetic moments within the wall are no longer aligned along an easy axis of magnetisation which increases the magnetocrystaline anisotropy energy. The magnetocrystalline energy is thus minimised by thin domain walls with an abrupt change in the direction of magnetisation (as shown in Figure 2.7(b)). Experimental studies have calculated that the domain wall thickness (δ) is on the order of 10^{-5} cm. The resulting domain structure is arranged to minimise the contained total of the domain wall, magnetostrictive, magnetocrystalline anisotropy and magnetostatic energies [46].

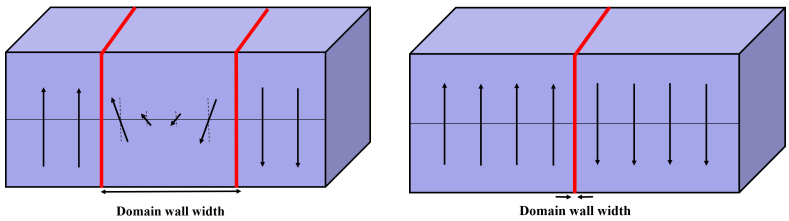

(a) (b)

Figure 2.7: Schematic of the two possible domain walls. (a) There is a gradual switch of the magnetisation vector from one direction to the other (it should be noted that each arrow represents several 10's of unit cells). The exchange energy price is lower, but there are more spins in unfavorable directions, increasing the magnetocrystalline energy. (b) There is a 180° switch in the magnetisation vector from one atom to the next. The domain wall is very thin, but the exchange price is very high.

2.5 Dielectric Properties of Spinel Ferrites

Sintered spinel ferrite (bulk ferrite) is composed of semi-conducting grains encapsulated by insulating grain boundary layers [47]. The semi-conducting grains contain the oxygen, tetrahedral and octahedral sites. In ferrites, an exchange of electrons takes place between Fe^{2+} and Fe^{3+} ions as well as the exchange of holes between M^{2+} and M^{3+} ions, where M is a divalent metal such as manganese or nickel. This electron hopping process occurs exclusively at octahedral sites and results in local displacement of charge carriers in the direction of the electric field, which leads to electric polarization. Although the grains are described as semi-conducting, the electrons do not occupy states in energy bands and the charge carriers are not free to move through the crystal lattice, instead they are localised at octahedral sites and jump from ion to ion. The electric properties of the semi-conducting grains depend on the distribution and amount of magnetic and non-magnetic ions as well as grain size (that is dictated by the sintering conditions during the ferrite manufacturing process).

2.5.1 Resistivity

The resistivity of ferrites can vary greatly from 10^{-3} to 10^{10} Ohm.cm depending on the distribution of metal ions on A (tetrahedral) and B (octahedral) sites. To obtain low values of resistivity, all B sites must be filled with trivalent iron ions and divalent metal ions. Both Fe^{2+} and Fe^{3+} ions are at B sites and conduction takes place when electrons move from Fe^{2+} to Fe^{3+} ions.

2.5.2 The hopping model

The probability of electron hopping is related to vibrations in the lattice, thus the conduction process is dependent on the lattice vibrations and in consequence the carrier mobility shows a temperature dependence characterized by the energy required to transfer an electron from a divalent metal ion to a trivalent iron ion and vice verca ($\triangle$E). The electron hopping process can be represented as the following;

$$Fe^{2+} + Fe^{3+} \leftrightarrow Fe^{3+} + Fe^{2+} + \triangle E \tag{2.3}$$

$$M^{2+} + Fe^{3+} \leftrightarrow M^{3+} + Fe^{2+} + \triangle E \tag{2.4}$$

When an electric field is applied, it is this hopping process that constitutes the flow of current. In ferrites, the distance between B sites is smaller than the distance between both A sites and the distances between an A site and a B site. Despite this, even the distance between B sites is much larger than the sum of ionic radii of the ions involved, indicating that the d wave functions of ions on adjacent octahedral sites do not overlap. This results in the electrons remaing fixed on B- sites necessitating a hopping process and inhibiting the electrons to move freely through the crystal.

2.5.3 Permittivity of Ferrites

The permittivity of ferrites depends strongly on frequency and can depend upon the method of preparation, chemical composition and substitution, grain structure or size and sintering temperature [48]. The dispersion of the permittivity is based on the Maxwell-Wagner Theory (The Interfacial Polarisation Model) which models a first layer of semi-conducting ferrite grains and a thin second layer of insulating grain boundary [49]. A phenomenological theory by Koop [50] describes this model in terms of parallel resistors and capacitors for good conducting grains and poorly conducting grain boundaries, resulting in an equivalent to the solid state model that obeys the dispersion formulas. V. Loyau *et al.* [51] have found that while the permittivity of a MnZn sintered ferrite (containing both the semi-conducting grains and insulating grain boundary layers) was as high as 50,000 at 0.1 MHz, the permittivity of the semi-conducting grain itself was only 350. The large increase in permittivity arises from the internal grain boundary layers acting like capacitors, which gives rise to a 'giant dielectric phenomenon' as there is significant build up of charge at the boundaries due to the electron hopping process being halted at this insulating boundary layer [52–54]. The hopping frequency is dictated by the frequency of the applied electric field, as the frequency of the applied AC electric field is increased, a phase lag develops between the

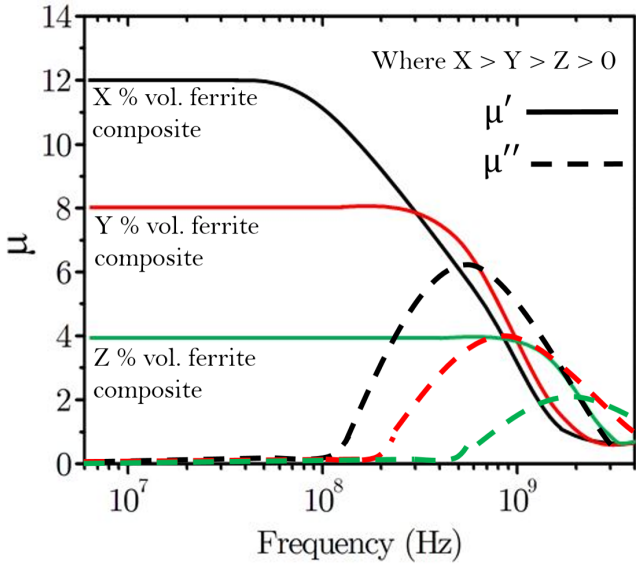

Figure 2.8: Schematic of complex permeability as a function of frequency for three different % vol. fractions of ferrite in a dielectric matrix, where X, Y and Z are three different % vol. fractions of the ferrite.

field and the electron hopping frequency which reduces the ability for the ferrite grains to become polarised and hence the permittivity decreases.

2.6 Frequency Dispersion of Complex Permeability in Ferrites

Soft magnetic materials such as spinel ferrite composites posses a high real permeability and near zero imaginary permeability at DC and up to approximately 100 MHz (depending on the %vol. of ferrite filler in the dielectric matrix). Above 100 MHz, the imaginary permeability increases rapidly while the real permeability drops rapidly as a result of a heavily damped relaxation phenomena related to the dynamics of the domain walls. The domain wall motion involves the rotation of the magnetic moments within the domain wall as the wall moves to a new position. While the dynamics of the domain walls takes place at radio-frequencies (1 MHz - 1 GHz), the natural ferromagnetic resonance (gyromagnetic spin resonance) occurs at higher frequencies (1 - 100 GHz).

Figure 2.8 shows the frequency dispersion of the complex permeability for a ferrite composite for three different % vol. fractions of ferrite filler. It can be seen that as the magnitude of the initial real permeability is inversely proportional to the frequency position of the peak of the imaginary permeability loss peak i.e. the higher the initial

real permeability, the lower the frequency of the peak imaginary permeability and the larger the imaginary permeability is at this frequency point. Although the frequency dispersion of the permeability in spinel ferrites follows the Snoek's Law relation, this model describes the ferromagnetic resonance only [6]. In reality, it is the domain wall motion that contributes exclusively to the frequency dispersion of the permeability at MHz frequencies. This indicates that the microstructure (arrangement of domains and domain walls) of the ferrite has a significant effect on the frequency dependent permeability described by Snoek's law [55].

The relative complex permeability is defined by the ratio of the magnetic field or magnetic induction ($\underline{B}$) to the magnetic field strength ($\underline{H}$);

$$\underline{\underline{\mu}} = \frac{\underline{B}}{\underline{H}}. \tag{2.5}$$

When the frequency of the AC magnetic field is small, the magnetisation process that takes place in the ferrite are in phase with the applied field, however, as the frequency of the applied AC field is increased, the magnetisation process in the ferrite becomes out of phase with the applied AC field and a phase delay is introduced (δ). The permeability (which is now assumed to be isotropic) can more generally be described as the following;

$$\mu(\omega) = \frac{\underline{B}(\omega)}{\underline{H}(\omega)} = \frac{\underline{B}_0 e^{-i\omega t + i\delta}}{\underline{H}_0 e^{-i\omega t}} = \frac{\underline{B}_0}{\underline{H}_0} e^{i\delta} \tag{2.6}$$

By separating the real and imaginary components of the permeability it can be seen that;

$$\mathrm{Re}[\mu(\omega)] = \frac{\underline{B}_0}{\underline{H}_0} \cos\delta, \tag{2.7}$$

$$\mathrm{Im}[\mu(\omega)] = \frac{\underline{B}_0}{\underline{H}_0} \sin\delta. \tag{2.8}$$

The value of the permeability is dependent on two mechanisms for magnetisation which can be in phase or out of phase with the applied AC magnetic field depending on the frequency. These two mechanisms are domain wall motion and gyro-magnetic spin precession are are discussed in the following sections.

2.7 Gyromagnetic Spin Resonance-Snoek's Law

The gyromagnetic spin resonance occurs within magnetic domains when an external magnetic field interacts with the magnetic moments within the domains and is described

by the Landau-Lifshitz-Gilbert equation [56, 57]. This resonance occurs when the frequency of precession of the magnetic moments about the direction of the internal magnetic field is equal to the frequency of the applied AC magnetic field.

Unlike bulk ferrites, ferrite composites have a non-uniform distribution of the magnetisation across the sample. This is due to the magnetic particles in composites being isolated by a non-magnetic layer that separates them, allowing for inter-phase polarisation and the formation of magnetic dipoles within the sample. This increases the demagnetising field effects, which not only arise from the shape of the sample (as in the case of bulk ferrite), but also the structural inhomogeneity of the composite. The increase in demagnetising fields for ferrite composites lowers the value of the low frequency permeability, which, in accordance with Snoek's law, extends the frequency range over which the permeability remains constant.

2.7.1 Snoek's Law

Figure 2.8 shows a graphical representation of Snoek's Law [6], and, as previously discussed, this law relates the DC value of the real permeability (μ') and the resonant frequency (f_r), which is determined by the peak of the imaginary permeability (μ''). This trade-off between the magnitude of the low frequency (from DC up to kHz/MHz frequencies) permeability and the frequency range over which this high permeability value remains and is given by Equation 2.9 (Snoek's Law):

$$f_r(\mu' - 1) = \frac{2}{3} g \mathrm{M_s} \tag{2.9}$$

where $g = 2.8$ MHz/Oe is the gyromagnetic ratio (for a cubic magnetocrystalline anisotropy) and $\mathrm{M_s}$ is the saturation magnetisation. Equation 2.9 shows that there is a limited bandwidth over which ferrites can be used due to this trade-off. In Snoek's original paper [6], it is the gyromagnetic spin resonance (introduced at the beginning of this section) that is described analytically. In order to derive Equation 2.9, the gyromagnetic spin ratio of a spinel ferrite is firstly deduced empirically. The gyromagnetic ratio is the ratio between the magnetic moment of a material and it's angular momentum. Snoek found through experiment that this ratio was approximately equal to that of a spinning electron, i.e;

$$\frac{\mu_b}{j} = \frac{eh}{4\pi mc} : \frac{1}{2}\frac{h}{2\pi} = \frac{e}{mc}, \tag{2.10}$$

where μ_b is the value of a unit of magnetic moment of an electron, called the Bohr magneton and j is the angular momentum. Therefore, the gyromagnetic ratio is equal

to the following;

$$g = \frac{e}{mc} = -1.76 \times 10^6 \text{rads}^{-1}\text{T}^{-1}. \tag{2.11}$$

Following the deduction of the gyromagnetic ratio of a spinel ferrite, the gyromagnetic resonant frequency of a spinel ferrite can be found. The elementary magnet is considered to be an isotropic and homogeneous ferromagnetic-sphere that possesses a constant magnetic moment ($\underline{\mathrm{M}}$) under the application of a constant magnetic field ($\underline{\mathrm{H}}_{p,z}$) which is in the $\underline{z}$ direction. At time t_0, a second magnetic field ($\underline{\mathrm{h}}_{0,x}$) is then applied in the $\underline{x}$ direction, which shifts the direction of the magnetic moment by an angle ϕ (assuming small angles) given by;

$$\phi = \frac{\underline{\mathrm{h}}_{0,x}}{\underline{\mathrm{H}}_{p,z}}. \tag{2.12}$$

The magnetic moment now precesses in a circular motion around the new position due to the application of $\underline{\mathrm{h}}_{0,x}$ as shown in Figure 2.9 (a). The undamped circular motion of the magnetisation vector is assumed to precess with a frequency that is directly proportional to the applied magnetic field ($\underline{\mathrm{H}}_{p,z}$);

$$f_r = 2\pi g \underline{\mathrm{H}}_{p,z} \tag{2.13}$$

Due to the initial magnetic suseptibility in the $\underline{\mathrm{x}}$- direction ($\underline{\underline{\chi}}_{x,x}$) being equal to the ratio of the magnetic moment ($\underline{\mathrm{M}}_x$) to the external magnetic field ($\underline{\mathrm{H}}_{p,z}$), i.e.

$$\underline{\underline{\chi_{x,x}}} = \frac{\underline{\mathrm{M}}_x}{\underline{\mathrm{H}}_{p,z}} \tag{2.14}$$

it follows that:

$$f_r = 2\pi g \frac{\underline{\mathrm{M}}_x}{\underline{\underline{\chi_{x,x}}}}. \tag{2.15}$$

Equation 2.15 clearly shows the inverse relationship between the frequency of undamped precession for a magnetic moment (f_r) and the initial magnetic susceptibility ($\chi_{x,x}$).

In reality, ferrites are not always fully magnetised in a way that has been artificially created in the situation above by the polarising field $\underline{\mathrm{H}}_{p,z}$. The presence of $\underline{\mathrm{H}}_{p,z}$ provides an energy minimum at $\phi = 0$, independent of the azimuth (θ). If the static magnetic susceptibility is denoted $\underline{\underline{\chi}}_{\mathrm{st}}$, then;

$$\underline{\underline{\chi}}_{x,x} = \underline{\underline{\chi}}_{\mathrm{st}} \sin\theta. \tag{2.16}$$

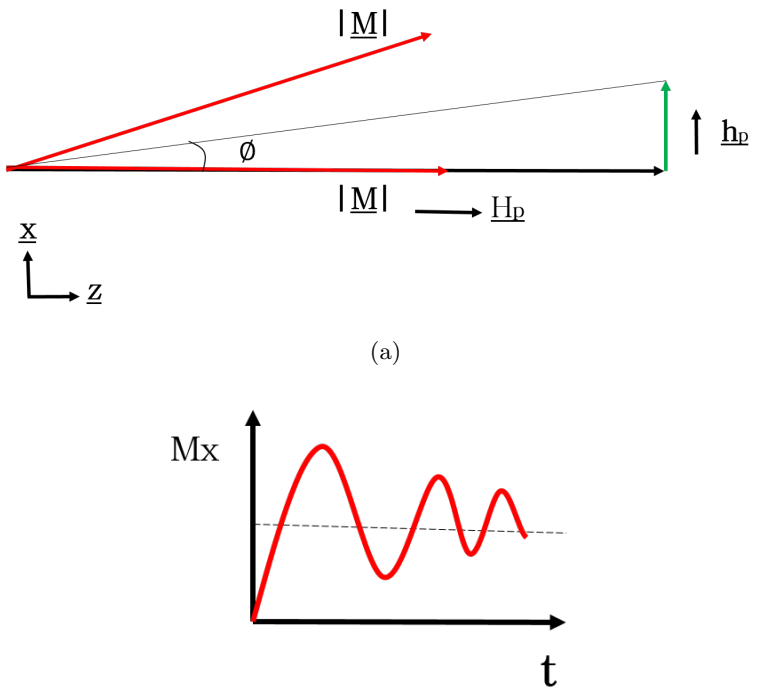

Figure 2.9: Graphical representation of the magnetisation vector after the application of a magnetic field ($\underline{h}_{0,x}$) at right angles to $\underline{H}_{p,z}$ with (a) the new position of the magnetisation vector set up as a result of $\underline{h}_{0,x}$ and (b) The oscillation of the magnetisation vector between zero and twice the equilibrium value.

If the ferrite is magnetised in a random direction, the ratio of the susceptibility $\underline{\underline{\chi}}_{x,x}$ to the susceptibility $\underline{\underline{\chi}}_{st}$ as defined by equation 2.15 is;

$$\frac{\underline{\underline{\chi}}_{x,x}}{\underline{\underline{\chi}}_{\mathrm{st}}} = \frac{\int_0^{\pi} 2\sin^3\theta d\theta}{\int_0^{\pi} \sin\theta d\theta} = \frac{2}{3}. \tag{2.17}$$

The factor of $\frac{2}{3}$ is added to Equation 2.15 to account for a polycrystalline ferrite that is randomly orientated (instead of a single crystal which is fully magnetised) giving;

$$f_r = \frac{4}{3}\pi g \frac{\underline{M}_x}{\underline{\underline{\chi}}_{x,x}}. \tag{2.18}$$

Although Snoek found that Equation 2.18 provided an estimate (to within the correct order of magnitude) for predicting the resonant frequency of a polycrystalline ferrite, it is not exact. The discrepancy arises from many factors such as internal stresses

and damping that have not been accounted for. Despite this, Snoek verified that in order to increase the operational frequency of ferrites, either the saturation magnetisation of the ferrite must be increased, or the component of the magnetic susceptibility perpendicular to the applied magnetic field must be reduced. More recent work has found that using highly anisotropic materials such as hexagonal ferrites can extent the Snoek's limit [58].

2.7.2 Domain Wall Resonance

As previously discussed, ferrites are composed of domains separated by domain walls. Under the application of an external magnetic field, the domains with a net magnetisation in the same direction as the external field grow in size while the domains with a net magnetisation in the opposite direction to the external field shrink. The domain size changes as a result of the movement of the domain walls, which bulge (reversibly) and vibrate in response to an AC magnetic field below the resonant frequency of the domain walls. Because the domain wall vibrations have a characteristic frequency, the ferrite has a frequency dependent permeability arising from the domain walls. There is a relaxation phenomena associated with the domain wall resonant frequency which is dependent on the microstructure of the ferrite, i.e. the width, mass and stiffness of the domain wall [59].

2.8 Electromagnetic Mixing Laws

This section analyses the simplest model for dielectric mixtures (the Maxwell-Garnett formula [17]) before analysing the Lichtenecker mixing law [23]. To begin with, the polarisability of a dielectric sphere (a single scatterer) will be derived before being applied to a mixture of many inclusions. The result of this derivation is known as the Clausius-Mossotti formula that relates the effective permittivity of a composite to microscopic quantities such as polarisability and the number of inclusions in the composite. However, a mixing formula in this form is not of much practical use as knowledge of quantities like the number of inclusions is not usually known. Therefore, the Clausius-Mossotti formula is modified to replace such microscopic quantities with macroscopic quantities. The resulting equation is called the Maxwell-Garnett formula which links the effective permittivity of the composite to the permittivities of the individual components. To obtain this, the Clausius-Mossotti formula is combined with an expression for polarisability, yielding a far more convenient relation to compare to experimental results. Lastly, a logarithmic mixing law known as the Lichtenecker formula is introduced and derived from Maxwell's equations. The Lichtenecker mixing law is

used in subsequent experimental chapters as a theoretical fit to the experimental data points for ferrite-PTFE and ferrite-cellulose composites (see Chapter 4).

2.8.1 Clausius-Mossotti formula

The Clausius-Mossotti formula describes the effective permittivity of a composite with a distribution of filler particles, with each particle treated as an electric dipole moment. The average of all these electric dipole moments is taken to obtain the net average electrical polarisation of the collection of particles. It is assumed that the particles are much smaller than the wavelength of the incident radiation. The effective permittivity ε_{eff} of this heterogeneous sample is defined by the average electric field $\underline{\text{E}}$ and the electric flux density $\underline{\text{D}}$.

$$< \underline{\text{D}} >= \varepsilon_{\text{eff}} < \underline{\text{E}} >= \varepsilon_m < \underline{\text{E}} > + < \underline{\text{P}} > \tag{2.19}$$

Here, ε_{m} is the permittivity of the matrix and $< \underline{\text{P}} >$ is the the average polarisation density induced by the collection of particles. $< \underline{\text{P}} >$ is equal to the dipole moment of a single particle $\underline{\text{P}}_{\text{mix}}$ multiplied by the number of particles n;

$$< \underline{\text{P}} >= n\underline{\text{P}}_{\text{mix}}, \tag{2.20}$$

The next step is to calculate the field that excites a single particle. To achieve this, the matrix along with the filler particles are expressed by an average polarisation. The single particle of interest is then removed to leave behind a fictitious void, where the local electric field within the void is expressed as $\underline{\text{E}}_{\text{L}}$, this situation can be visualised by Figure 2.10.

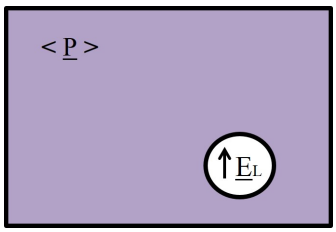

Figure 2.10: Fictitious void in a location of the single particle of interest within a composite composed of a distribution of particles in a background matrix. $< \underline{\text{P}} >$ denotes the average polarisation and $\underline{\text{E}}_L$ is the field exciting the single particle.

Assuming that all the particles and the fictitious void are spherical in shape, $\underline{\text{E}}_{\text{L}}$ can be expressed as the following;

$$\underline{\text{E}}_L =< \underline{\text{E}} > + \frac{1}{3\varepsilon_m} < \underline{\text{P}} >, \tag{2.21}$$

where $\frac{1}{3}$ is the depolarisation factor for a sphere. The dipole moment of the single particle that has been removed ($\underline{\mathrm{P}}_{\mathrm{mix}}$) is directly proportional to the product of the local electric field ($\underline{\mathrm{E}}_{\mathrm{L}}$) field and the polarisibility of that particle (α);

$$\underline{\mathrm{P}}_{\mathrm{mix}} = \alpha \underline{\mathrm{E}_L} \tag{2.22}$$

Combining these equations provides us with the Clausaus-Mossotti formula [60, 61] linking the effective permittivity $\varepsilon_{\mathrm{eff}}$ with the polarisabily of a single particle (α), the number of particles (n) and the permittivity of the matrix (ε_{m}).

$$\frac{\varepsilon_{\mathrm{eff}} - \varepsilon_m}{\varepsilon_{\mathrm{eff}} + 2\varepsilon_m} = \frac{n\alpha}{3\varepsilon_m}. \tag{2.23}$$

2.8.2 Maxwell-Garnett formula

As previously mentioned, the Clausius-Mossotti formula is limited to microscopic applications as the formula expresses the effective permittivity as a function of microscopic quantities such as the number of inclusions (N_i) and their individual polarisibilities (α). Therefore, in order to make it applicable to macroscopic applications, α and N_i must be replaced with information about the proportion of the filler to matrix i.e. the fill fraction f and the permittivities of the filler and matrix, ε_{i} and ε_{m} respectively. The Maxwell-Garnett formula provides this macroscopic relation by combining the Clausius-Mossotti formula with the expression for the polarisability of a single particle in a homogeneous background and takes the form:

$$\alpha = \mathrm{V}(\varepsilon_i - \varepsilon_m)\frac{3\varepsilon_m}{\varepsilon_i + 2\varepsilon_m}. \tag{2.24}$$

The Maxwell-Garnett formula can thus be written as the following:

$$\frac{\varepsilon_{\mathrm{eff}} - \varepsilon_m}{\varepsilon_{\mathrm{eff}} + 2\varepsilon_m} = f\frac{\varepsilon_i - \varepsilon_m}{\varepsilon_i + 2\varepsilon_m}, \tag{2.25}$$

where $f = N_i V$ denotes the volume fraction of the filler. This formula satisfies both limits of v, i.e. when the filler approaches 0% vol., $\varepsilon_{\mathrm{eff}}$ tends to ε_{m}, and when the filler approaches 100% vol., $\varepsilon_{\mathrm{eff}}$ tends to ε_i.

The Maxwell-Garnett formula is however limited to the following cases;
1) The particles are spherical,
2) The volume occupancy of the filler is below percolation (in the case of conducting inclusions),
3) The particles do not interact with each other,
4) The limiting case of v tending to unity is not achievable in reality as the upper fill

fraction of irregularly packed identical spheres is 64%.
Theoretically, however, a fill fraction approaching $v = 1$ is achieved by a fractal filling process.

Although the Maxwell-Garnett mixing law is widely used, it is not suitable for dense materials and in practical random medium theory and applications [62]. An alternative set of mixing rules known as the 'power laws' have been introduced, which is the focus of discussion in the next subsection.

2.8.3 Power-Law Models

Power laws were first suggested by Lichtenecker [23], however, the different background and a lack of analytical support resulted in power laws being generally considered as only an empirical tool for a long time. In 2010, Simpkin demonstrated that the Lichtenecker mixing formula (which is a specific type of power law) can be derived analytically from Maxwell's equations[63].

Power laws are a group of EM mixing laws that are described by the following approximation;

$$\varepsilon_{\text{eff}}^{\beta} = f\varepsilon_i^{\beta} + (1-f)\varepsilon_m^{\beta} \tag{2.26}$$

where ε_{eff} is the permittivity of the two part composite, f is the fraction of the filler material, β is the power that the permittivity is raised to, ε_i is the permittivity of the filler and ε_m is the permittivity of the matrix. The power that the permittivities are raised to varies in order to fit experimental data to a mixing law. For example, in Birchak's formula, $\beta = \frac{1}{2}$, which means that the square root of both ε_i and ε_m add up to the square root of ε_{eff} [64]. Other examples include the Looyenga formula, where $\beta = \frac{1}{3}$ [65] and the Silberstein formula, where $\beta = 1$, providing a linear relationship between ε_{eff} and f [13].

The Lichtenecker mixing formula can be deduced from Equation 2.26 by performing a power series expansion about the point $\beta = 0$. If Equation 2.26 is rearranged to the following;

$$\varepsilon_{\text{eff}} = (f\varepsilon_i^{\beta} + (1-f)\varepsilon_m^{\beta})^{\frac{1}{\beta}}. \tag{2.27}$$

The first two terms of the expansion of ε_{eff} are given below;

$$\varepsilon_m^{1-f}\varepsilon_i^{f} - (\frac{1}{2}(-1+f)f\varepsilon_m^{1-f}\varepsilon_i^{f}(\ln\varepsilon_m - \ln\varepsilon_i)^2)\beta + ... \tag{2.28}$$

In the limit of $\beta \to 0$, only the first term in the expansion remains, which is the

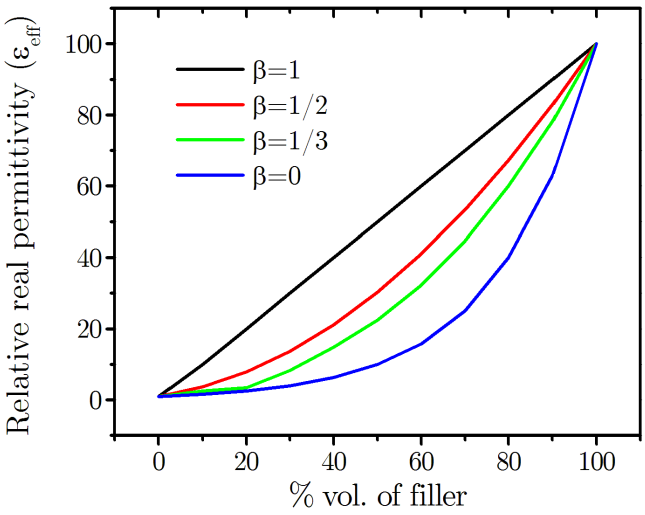

Figure 2.11: The relative real permittivity of a composite (ε_{eff}) containing a filler permittivity (ε_i) equal to 100 and a matrix permittivity (ε_m) equal to 1 as a function of % vol. of the filler. The highest curve corresponds to $\beta = 1$, then $\beta = \frac{1}{2}$, $\beta = \frac{1}{3}$, and the lowest one is $\beta = 0$ (the Lichtenecker mixing law).

Lichtenecker mixing law. The power-law used in the experimental chapters of this thesis is the Lichtenecker mixing formula [23]. This law averages the logarithms of the permittivities, and is a special case of the power-law mixtures that predicts an exponential relationship between ε_{eff} and f as shown in Equation 2.29;

$$\varepsilon_{\text{eff}} = \varepsilon_i^f \varepsilon_m^{(1-f)} \tag{2.29}$$

Figure 2.11 shows shows the effective relative real permittivity as a function of % vol. for each of the 4 variations of the power law stated in Equation 2.26 when $\beta = 1, \frac{1}{2}, \frac{1}{3}$ and 0.

The Lichtenecker mixing formula (Equation 2.29) is based of the following assumptions;

1) The filler and matrix particles are randomly distributed in the matrix,

2) The filler and matrix particles are both randomly orientated and of random shape (so the charge density of the particles can be replaced by the mean charge density of the mixture), this allows for the direct interchange between charge fractions and % vol. fractions.

3) The particle size is much smaller than the wavelength of the incident radiation so the two part mixture can be treated as an effective medium.

The validity of this formula is dependent on how well the particles are dispersed and how random their orientation/shape is (i.e. how statistically random the mixture is). If this assumption is satisfied, the Lichtenecker mixing formula is more likely to provide an accurate method in predicting the effective permittivity of dielectric mixtures. Although this derivation focuses on predicting the permittivity from a dielectric mix, an equivalent equation can be used for deducing the effective permeability from a two part mixture [66];

$$\mu_{\text{eff}} = \mu_i^f \mu_m^{(1-f)} \tag{2.30}$$

Equations 2.29 and 2.30 will be used in Chapters 4 and 5 to predict the effective permittivity and permeability of two part ferrite-PTFE and ferrite-cellulose composites in the more familiar form;

$$\ln\varepsilon_{\text{eff}} = f\ln\varepsilon_i + (1-f)\ln\varepsilon_m \tag{2.31}$$

and

$$\ln\mu_{\text{eff}} = f\ln\mu_i + (1-f)\ln\mu_m \tag{2.32}$$

2.9 Nicholson-Ross-Weir Derivation

The original results presented in experimental chapters in this thesis (Chapters 4-7) rely on the ability to extract complex permittivity and complex permeability for a material sample under test from the complex reflection and transmission amplitude coefficients (known as the complex S-parameters). This method is used for the extraction of complex permittivity and permeability of both bulk samples and metamaterial samples, using both experimentally and numerically deduced complex S- parameters. This section focuses on this extraction, which is known as the Nicholson-Ross-Weir extraction method [67, 68]. The following derivation is described in Figure 2.12 which shows an air-material-air system whereby a beam of incident radiation onto the material is reflected (multiple times) and transmitted.

The first stage in deducing the complex permittivity and permeability is to sum all the reflection occurring at the air-sample interfaces. The sum of these reflections is equal to the total reflection (r_{13}) and is expressed in Equation 2.33;

$$r_{13} = r_{12} + t_{12}t_{21}r_{23}e^{2i\alpha} + t_{12}t_{21}r_{23}^2r_{21}e^{4i\alpha} + \text{.....} \tag{2.33}$$

By summing over n number of reflections, Equation 2.33 can be simplified to the

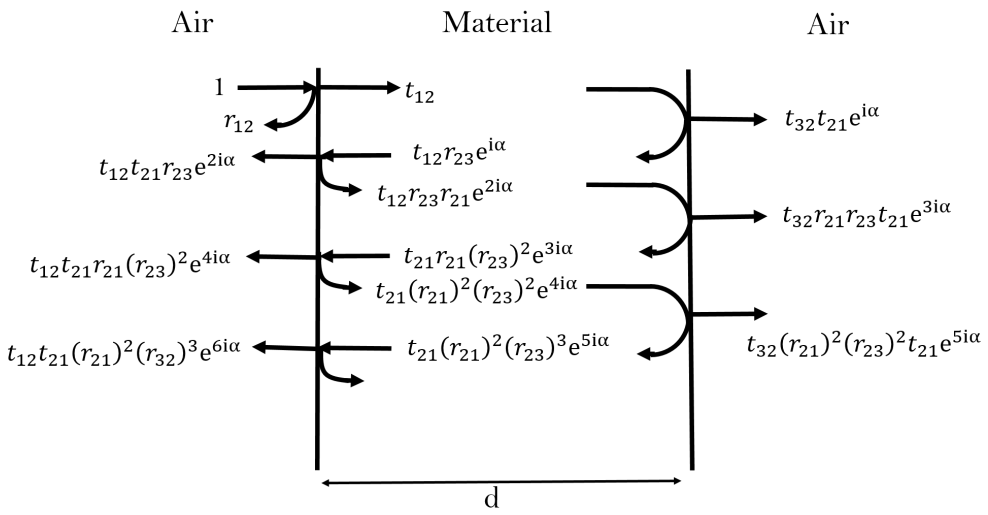

Figure 2.12: Diagram showing multiple reflection and transmission amplitudes that occur when an incident wave (travelling through air) strikes a sample. This system consists of two interfaces separating three layers denoted Air-Material-Air.

following;

$$r_{13} = r_{12} + t_{12}t_{21}r_{23}e^{2i\alpha}\sum_{n=0}^{\infty} r_{21}^n r_{23}^n e^{2i\alpha}. \tag{2.34}$$

Equation 2.34 can be further simplified by using the identity:

$$\sum_{n=0}^{\infty} x^n = \frac{1}{1-x}. \tag{2.35}$$

Giving a final equation (Equation 2.36) for r_{13} equal to the following:

$$r_{13} = t_{12} + \frac{t_{12}t_{21}r_{23}e^{2i\alpha}}{1 - r_{21}r_{23}e^{2i\alpha}}. \tag{2.36}$$

Equation 2.36 for the total reflection is in terms of the phase factor $e^{2i\alpha}$ and single interface Fresnel reflection co-efficients. In order to write the total reflection (r_{13}) in terms of the single interface reflection coefficients but for an infinitely thick slab, a set of identities must be used and are given by Equations 2.37 to 2.40. Here, a complex exponential is used to represent the propagation constant inside the material.

$$r_{21} = r_{23} = -r_{12} \text{ where } r_{12} = \frac{Z-1}{Z+1} \tag{2.37}$$

$$\beta^2 = e^{2i\alpha} \text{ where } \alpha = 2\pi\gamma d \tag{2.38}$$

$$t_{12} = 1 + r_{21} \tag{2.39}$$

$$t_{21} = 1 + r_{12}. \tag{2.40}$$

Here Z is the characteristic impedance, β is a complex exponential described by Equation 2.38, γ is the material's propagation constant and d is the sample thickness in the propagation direction. Equations 2.37 to 2.40 are used in combination with Equation 2.36 to find an equation for r_{13}, which is equivalent to the experimentally measured reflected S-parameter, S_{11}.

$$r_{13} = S_{11} = \frac{r_{12}(1 - \beta^2)}{1 - r_{12}^2\beta^2} \tag{2.41}$$

Now the sum of all the reflected wave components has been deduced, the sum of the transmitted wave components (transmitted completely through the material) must be found i.e. t_{13} (total transmitted) in terms of the transmitted wave amplitude coefficients. The total transmission coefficient t_{13} is equivalent to the following (found using the same method as for finding the reflection coefficient r_{13});

$$t_{13} = \frac{t_{12}t_{23}e^{i\alpha}}{1 - r_{21}r_{23}e^{2i\alpha}} \text{ where } t_{23} = 1 + r_{23} \tag{2.42}$$

$$t_{13} = S_{21} = \frac{\beta(1 - r_{12}^2)}{1 - r_{12}^2\beta^2}. \tag{2.43}$$

Once again, t_{13} is equivalent to the transmitted S-parameter measured experimentally and numerically (S_{21}). By comparing Equations 2.41 and 2.43, it is clear that both contain two unknown quantities (r_{12} and β). These two terms are determined by the complex permittivity and permeability of the material, therefore, Equations 2.41 and 2.43 must be treated as a pair of simultaneous equations in order to deduce the values of r_{12} and β. To find these two unknowns, both the sum and the difference between S_{11} and S_{21} must be calculated;

$$V_1 = S_{21} + S_{11} \text{ and } V_2 = S_{21} - S_{11}, \tag{2.44}$$

$$V_1V_2 = S_{21}^2 - S_{11}^2 = \frac{\beta^2 - r_{12}^2}{1 - r_{12}^2\beta^2}, \tag{2.45}$$

$$V_1 - V_2 = 2S_{11} = \frac{2r_{12}(1 - \beta^2)}{1 - r_{12}^2\beta^2}, \tag{2.46}$$

$$X = \frac{1 - V_1 V_2}{V_1 - V_2} = \frac{1 + r_{12}^2}{2r_{12}}, \tag{2.47}$$

$$\sqrt{X^2 - 1} = \frac{r_{12}^2 - 1}{2r_{12}}, \tag{2.48}$$

$$r_{12} = X \pm \sqrt{X^2 - 1}. \tag{2.49}$$

Note that in Equation 2.49, there is both a positive and a negative root however, it is clear that the modulus of r_{12} must be less than or equal to 1. Now that r_{12} is determined, it is possible to calculate β (the value of the complex exponential);

$$V_1 - r_{12} = \frac{(1 - r_{12}^2)(\beta - \beta^2 r_{12}^2)}{1 - r_{12}^2 \beta^2} \tag{2.50}$$

$$1 - V_1 r_{12} = \frac{1 - \beta r_{12} + \beta r_{12}^3 - r_{12}^2}{1 - r_{12}^2 \beta^2}. \tag{2.51}$$

By dividing Equation 2.50 by Equation 2.51, it is possible to gain an expression for x, the complex exponential, in the simplest form;

$$x = \frac{V_1 - r_{12}}{1 - V_1 r_{12}} = \frac{x(1 - x r_{12})}{1 - x r_{12}} \tag{2.52}$$

Now that expressions for both r_{12} and β have been deduced, it is possible to find vales for the complex permittivity and permeability. However, the complex exponential term β must be calculated in terms of γ (complex propagation constant) and d (the sample thickness) using Moivre's theorem:

$$x^n = (\cos\theta + j\sin\theta)^n, \tag{2.53}$$

$$\frac{1}{x^n} = (\cos\theta + j\sin\theta)^{-n}, \tag{2.54}$$

$$\frac{1}{x} = e^{d\gamma}, \tag{2.55}$$

$$\ln\frac{1}{x} = d\gamma, \tag{2.56}$$

$$\frac{1}{d}\ln\frac{1}{x} = \gamma. \tag{2.57}$$

If a free space measurement is assumed, consisting of an infinitely long material

sample, the normalised impedance can be expressed in terms of the relative complex permittivity and permeability as given by Equation 2.58;

$$Z_m = \sqrt{\frac{\mu}{\varepsilon}}. \tag{2.58}$$

The propagation constant (γ) expressed in Equation 2.57 can also be expressed in terms of the complex permittivity and permeability as shown in Equation 2.59;

$$\gamma = j\frac{2\pi}{\lambda_0}\sqrt{\mu\varepsilon} \text{ where } N = \sqrt{\mu_r\varepsilon_r} \tag{2.59}$$

where N is the refractive index of the material. Combining Equations 2.58 and 2.59, the material's complex permittivity and permeability can be expressed in terms of N_m and Z_m;

$$\mu_r = NZ_m \text{ and } \varepsilon_r = \frac{N}{Z_m} \tag{2.60}$$

This extraction method is used for deducing the complex permittivity and permeability from the complex S-parameters in numerical modelling, using Finite Element Method (FEM) modelling and imposing the neccesary boundary conditions in the model itself (master-slave boundary conditions) to effectively emulate the stripline measurement technique, which is described in Chapter 3.

2.9.1 Stripline correction factor

In order to employ this derivation for experimental stripline measurements, information about the stripline's electrical length must be included to account for a phase shift in the transmitted EM radiation due to the presence of the stripline. The electrical length of the stripline is the length in terms of the phase shift introduced by the transmission of EM radiation. The stripline electric length is included in the phase term associated with the complex reflection coefficient (r_{13}), and in the complex propagation constant in the material (γ). The calculation to deduce the stripline electric length experimentally is described in Chapter 3.

2.10 Conclusions

In this chapter, the three different types of magnetism, namely; diamagnetism, paramagnetism and ferromagnetism have been introduced, with a specific type of permanent magnetism, known as ferrimagnetism being the focus of the discussion. This type of magnetism relies on the magnetic moments from metallic ions being positioned

on two lattice sites and in opposing directions. The net magnetic moment from this arrangement gives a ferrimengnetic material its permanent magnetisation.

Spinel ferrites, a class of magnetic oxides which have unique EM properties, have been found to posses an inverse spinel structure, consisting of tetrahedral and octahedral sites (for metallic ions) which are separated by oxygen sites. Spinel ferrites are formed of magnetic domains separated by domain walls. The size and shape of these domains are dictated by a trade off between two conflicting energy contributions, namely the magnetocrystalline energy and the exchange energy. The physical structure of the polycrystalline ferrite consists of semi conducting grains (where electron hopping between iron ions occurs) and insulating grain boundaries, which act to inhibit the movement of electrons from grain to grain and the movement of domain walls. It is the electron hopping mechanism which dictates the dielectric properties of the ferrite.

The frequency dispersion of the complex permittivity and permeability were then discussed. The real permittivity decreases with increased frequency due to a dielectric relaxation process while the complex permeability undergoes a broad, heavily damped resonance known as the domain wall resonance. The frequency dispersion of the complex permeability was explained in terms of Snoek's Law which links the value of the static permeability to the resonant frequency. This law is based on the magnetic resonant behavior of a fully magnetised sphere, which is placed in an AC magnetic field. The magnetic susceptibility of the sphere is then written in terms of the ferromagnetic resonance, the saturation magnetisation and the gyromagnetic ratio.

As mixing laws are used in the experimental chapters of this thesis, they were introduced in this chapter. The Clausius-Mossotti relation describes the relationship between the permittivity of two different media and microscopic quantities such as the molecular polarisability, however, expressing the EM properties of the composite in terms of microscopic quantities is not practical, hence the Maxwell-Garnett mixing formula was introduced as a more useful relation. The Maxwell-Garnet mixing formula uses the Clausius-Mossotti relation to arrive at a far more practical mixing law involving the EM properties of the two constituent materials and their relative volumes. It was found in subsequent experimental chapters that the Lichtenecker mixing formula agreed with experimental data. The Lichtenecker mixing formula averages the natural logarithms of the permittivity and permeability, predicting an exponential rise in the permittivity/permeability with increasing % vol. of the filler.

Lastly, the Nicholson-Ross-Weir extraction method for deducing the complex permittivity and permeability from the complex reflection and transmission coefficients was derived in full as it is used throughout all experimental chapters in this thesis. This extraction method sums these reflection and transmission coefficients to deduce expressions for the total transmission (S_{21}) and the total reflection (S_{11}), along with

knowledge of the sample thickness, and the propagation constant (which is a property of the permittivity and permeability).

Chapter 3

Methods

3.1 Introduction

This chapter is broken down into three key areas; the fabrication of composite materials and cubic metamaterials, the electromagnetic characterisation of composite materials and cubic metamaterials and lastly, the numerical modelling techniques used to model the cubic metamaterials. In the first section, the structural properties of the ferrite powders (used to produce the composites) are discussed before moving on to the manufacturing technique used to fabricate these composites. The process used to fabricate the cubic metamaterials is also explained here. Following the fabrication techniques, the methods used to electromagnetically characterise composite materials and cubic metamaterials are described. These techniques include the experimental stripline set-up and two separate parameter extraction methods. Lastly, the Finite Element Method (FEM) modelling technique used to simulate the experimental measurements of the cubic metamaterials is described, and details of the boundary conditions, excitation sources and material assignment requirements are provided.

3.2 Polymers

In order to produce composite samples, a dielectric matrix is needed to bind the constituent materials, in this thesis, a polymer is used. Polymers are long chain molecules that form many types of plastics as well as natural materials such as DNA. In this thesis the polymer polytetrafluoroethylene (PTFE) is used as the matrix material to fabricate ferrite composite materials. Although alternative polymers such as epoxy resin, polyurethane, polypropylene and polyphenylene sulfide (PPS) were tested as potential matrix materials, the highest percentage loading of filler material in the composite was achieved with PTFE, hence this material was used. The PTFE powder was supplied

by Sigma Aldrich Ltd with a uniform particle diameter of 35 μm (as specified by the manufacturer).

3.3 Magnetic Fillers

The ferrite powders used throughout this study are commercially available products supplied by MagDev, namely F44 fully sintered MnZn ferrite powder and F16 fully sintered NiZn ferrite powder. While the F44 powder has extremely high static values of relative real permeability and permittivity of approximately 1.5×10^3 and 1.0×10^5 respectively, the F16 powder is manufactured for higher frequency applications and hence has comparably lower static values of permeability and permittivity which are approximately 125 and 100 respectively. This section analyses the properties of the sintered ferrite powders including the chemical composition (deduced from X-ray diffraction measurements), the distribution of particle sizes found by laser diffraction measurements, and the particle morphology of individual particles imaged using a scanning electron microscope.

3.3.1 X-ray diffraction patterns

X-ray diffraction measurements were performed on both the MnZn ferrite and the NiZn ferrite powders to deduce the chemical composition (including any impurity phases). The principle of X-ray diffraction involves measuring the angle and intensity of the diffracted X-ray beam, providing direct information about the crystal lattice spacing by applying Bragg's Law;

$$n\lambda = 2d \sin\theta \tag{3.1}$$

where n is an integer, known as the order of the diffracted beam, λ is the wavelength of the incident radiation (which is on the order of 1 Å), d is the distance between crystal planes and θ is the angle of the diffracted wave [69]. The characteristic X-ray diffraction (XRD) pattern for a crystal structure (described in Chapter 2) can be matched to a known structure by fitting the intensity peaks. The ferrite powder was measured by Miss Yunqi Wang for the University of Oxford and Dr Claire Dancer from the University of Warwick (as part of a collaborative QUEST project) using a Siemens D5000 X-ray diffractometer with Cu Kα radiation with $\lambda = 1.5406 \times 10^{-10}$ m which provided a series of intensity peaks that fitted to a cubic spinel structure as shown in Figure 3.1. This process involves matching the intensity peaks with specific known crystal structures, and then this crystal structure is deposited in a crystallographic database to determine the chemical composition. The exact chemical composition

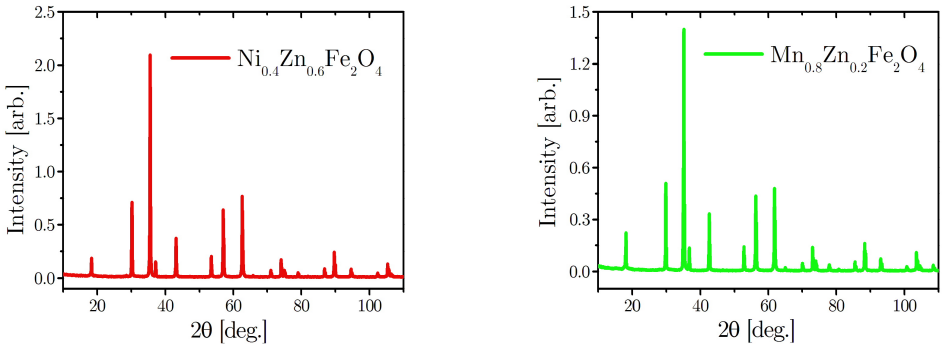

Figure 3.1: X-ray diffraction pattern of (a) NiZn ferrite powder and (b) MnZn ferrite powder supplied by MagDev Ltd. The chemical composition deduced for each of the ferrite powders is also given. The X-ray diffraction and the laser diffraction measurements were taken by Dr Claire Dancer from the University of Warwick and Miss Yunqi Wang from the University of Oxford (as part of a collaborative QUEST project).

of MnZn ferrite was determined to be $Mn_{0.8}$ $Zn_{0.2}Fe_2O_4$ with some minor impurity phases Fe_3O_4, Fe_2O_3, MnO while the chemical composition of the NiZn ferrite was $Ni_{0.4}Zn_{0.6}Fe_2O_4$ with minor impurity phases NiO_2, ZnO_2, and Fe_2O_3 and Fe_3O_4.

3.3.2 Laser diffraction measurements

Laser diffraction analysis is a method used to determine the particle size spread of powdered materials, in this study NiZn and MnZn ferrite powders were measured by Miss Yunqi Wang for the University of Oxford and Dr Claire Dancer from the University of Warwick (as part of a collaborative QUEST project). The laser beam produces a diffraction pattern as it passes through the suspended ferrite particles. This unique diffraction pattern is used to deduce the particle size and particle size range using Fraunhofer diffraction theory [70]. This states that the intensity of the scattered radiation is directly proportional the size of the scattering particles (assuming the particles to be perfectly spherical in shape). Although the ferrite particles used are not perfectly spherical, they do not possess a high aspect ratio that would alter the measured results. This is due to the flow of the particle suspending medium (typically deionised water) is not turbulent but laminar [71]. As a result, the flow alignment of the suspended particles causes the non-spherical particles orient themselves in the direction of the flow. Thus, when the aligned particles pass the laser beam, their measured volume is overestimated. This occurs when the aspect ratio of particles is

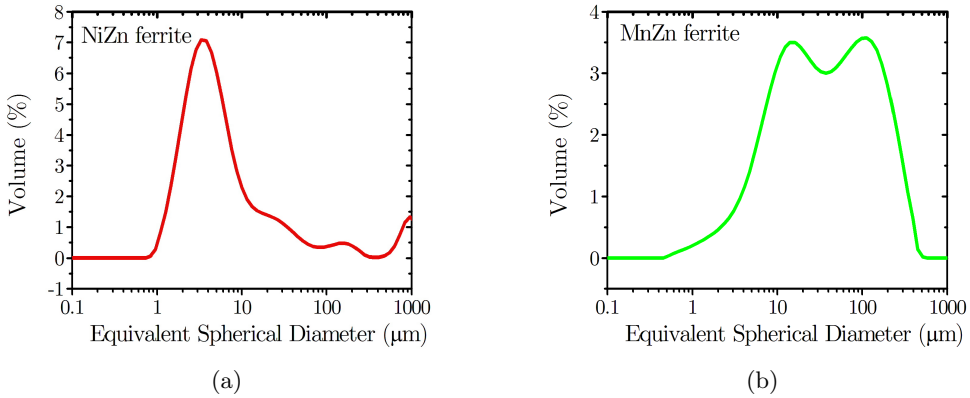

Figure 3.2: The ferrite particle size distribution determined by laser diffraction measurements for (a) NiZn ferrite powder and (b) MnZn ferrite powder. This data was taken by Miss Yunqi Wang for the University of Oxford and Dr Claire Dancer from the University of Warwick (as part of a collaborative QUEST project)

larger than 5:1 [72].

The Mastersizer2000 supplied by Malvern Instruments Ltd, UK was used to determine the median ferrite particle diameter for both the MnZn ferrite and the NiZn ferrite powder. Before any ferrite powder is added to the system, a background level was measured to remove any dirt particles inherent in the beaker or the suspending medium (in this case deionized water). The ferrite powder is then added to the beaker of deionized water which also contained a feed tube, a propeller and an ultrasonic probe. The propeller acts to keep the particles in constant suspension while the ultrasonic probe is used to break up any particle clusters. The feed tube pumps water and the suspended ferrite particles from the beaker into a test cell where the laser and detector were positioned. In total, the experiment is ran 5 times with the mean values taken to plot the final graph of number percent vs. equivalent spherical diameter as shown in Figure 3.2. The diffraction pattern obtained by the system (Mastersizer2000, Malvern Instruments Ltd, UK) the median MnZn ferrite particle diameter was found to be 35 μm while the range of particle sizes spanned from less than 1 μm to 500 μm as shown in Figure 3.2. The median NiZn ferrite particle size was found to be 4 μm also shown in Figure 3.2.

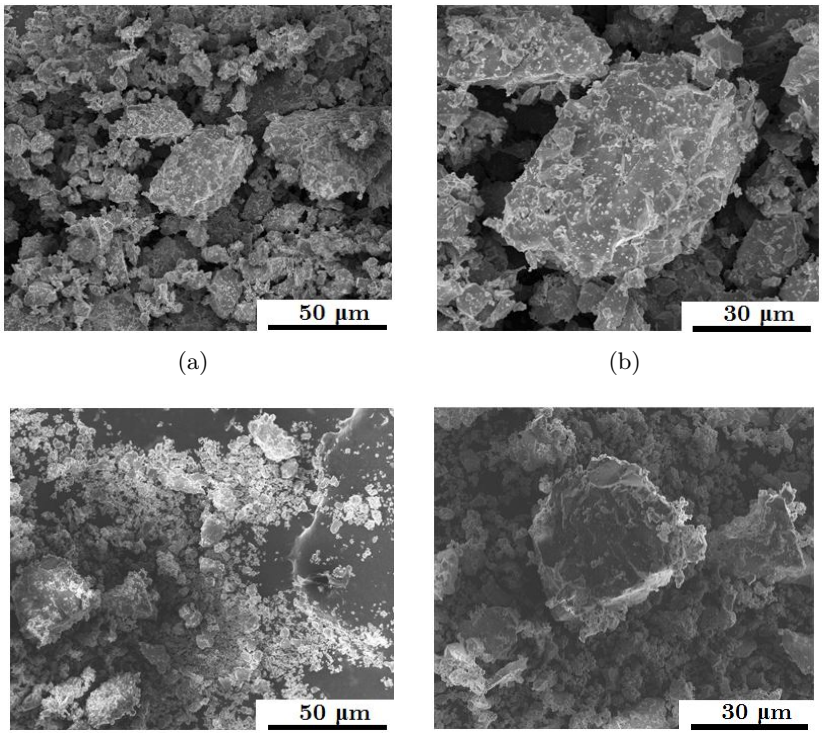

Figure 3.3: Backscattered scanning electron microscopy images of MnZn ferrite (a-b) and NiZn ferrite (c-d) powders. Images (a) and (c) show a collection of particles of varying size while images (b) and (d) focus on a single particle within the collection.

3.3.3 Scanning electron microscopy of pre-sieved MnZn and NiZn ferrite powder

The composites studied in Chapter 5 require sieved NiZn ferrite powder in a variety of size ranges to study how the ferrite particle size affects the magnetic and electric properties of the composites.

Both the MnZn and NiZn ferrite powders were imaged to look for signs of clustering and trends in the particle shape. Figure 3.3 shows that there is a large range in the particle sizes for both powders, with evidence of very fine material clustering with larger particles as shown in Figure 3.3 (a), as well as obvious non-uniformity in the particle shape.

Sieve size a (µm)	Average particle size from laser diffraction measurements (µm)	Maximum particle size, $\sqrt{a^2+a^2}$ (µm)
125	120	154
93	100	119
75	90	98
63	80	82
53	60	69
45	45	59
38	30	41
20	5	28

Table 3.1: Comparison between the sieve size, the average particle size deduced from laser diffraction measurements and the maximum particle size based on the sieve size in (µm).

3.3.4 Properties of sieved NiZn ferrite powder

The NiZn ferrite powder was sieved using a conventional sieving method whereby the sieves are stacked on top of each other in increasing mesh size and attached to a vibrating plate. The pre-sieved NiZn ferrite powder was placed in the top sieve, and over a time period of 3 hours the sieves collected the powder in 4 fractions. The larger mesh sizes were sourced in-house and possessed mesh sizes of 53 - 63 µm, 63 - 75 µm, 75 - 90 µm and 90 - 125 µm. To access smaller size ranges, MagDev sieved the same powder batch in the following sizes: less than 20 µm, 20 - 38 µm, 38 - 45 µm and 45 - 53 µm. The powders were imaged using scanning electron microscopy (SEM) to determine the particle size uniformity, and laser diffraction measurements were taken to deduce the particle size variation within each sieve range. It should be noted that the average mesh size e.g. 63 µm refers to the length of the side of a square mesh, however, it is the diagonal length of the square mesh that dictates the maximum particle diameter and can be calculated from $\sqrt{a^2+a^2}$, where a is the length of the side of the square mesh (as shown in Table 3.1). This table shows that the laser diffraction measurements are all below maximum particle diameter that is allowed to pass through the sieve.

Figure 3.4 shows that the sieving method is an effective way of separating ferrite particle sizes into narrow size ranges (above 38 µm) as single peaks are observed with the peak fitting into the sieve mesh size. However, it is clear that very small particles (5 µm) are present in the size range 20 - 38 µm: a double peak is observed in the data. Following these results, the powers were imaged using scanning electron microscopy to observe any uniformity of particle size within each size range.

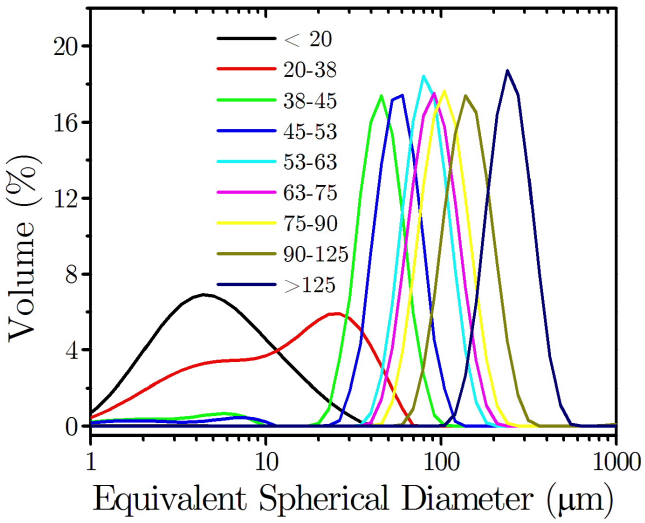

Figure 3.4: Laser diffraction measurements showing the volume % of particle size as a function of the equivalent spherical diameter for sieved NiZn ferrite powder.

Figures 3.5 and 3.6 show both a low magnification image (for each size range) as well as an image of a single particle, or particle cluster for each of the particle size ranges. While the fine particles (less than 45 μm) have a tendency to clump together to form large clusters, the larger particles (45 - 125 μm) appear more evenly distributed. It should also be noted that fine particles (1 μm) also have the tendency to cluster around the larger particles creating a fine coating around these larger particles. This can be observed in Figure 3.6(d) and (f) in particular. The particle shape for all size fractions is not uniform and in some cases, individual particles are formed of many small particles. Despite evidence of clustering for some of the smaller particle sizes, the size of the majority of the particles imaged are in accordance with both the laser diffraction measurements and the sieve sizes. It is also evident that all the size ranges contain some very fine material, however, as the combined volume of the fine material is very small in comparison to the combined volume of the larger particles, this feature is not reflected in Figure 3.4.

3.4 Fabrication of ferrite composites

The ferrite composite samples used in the following experimental chapters were all fabricated via the following cold pressing method. The cold pressing technique provides a time efficient way of producing composite samples for a range of volume fractions of filler material that vary from 0% to 80%. The ferrite and PTFE powders were mixed

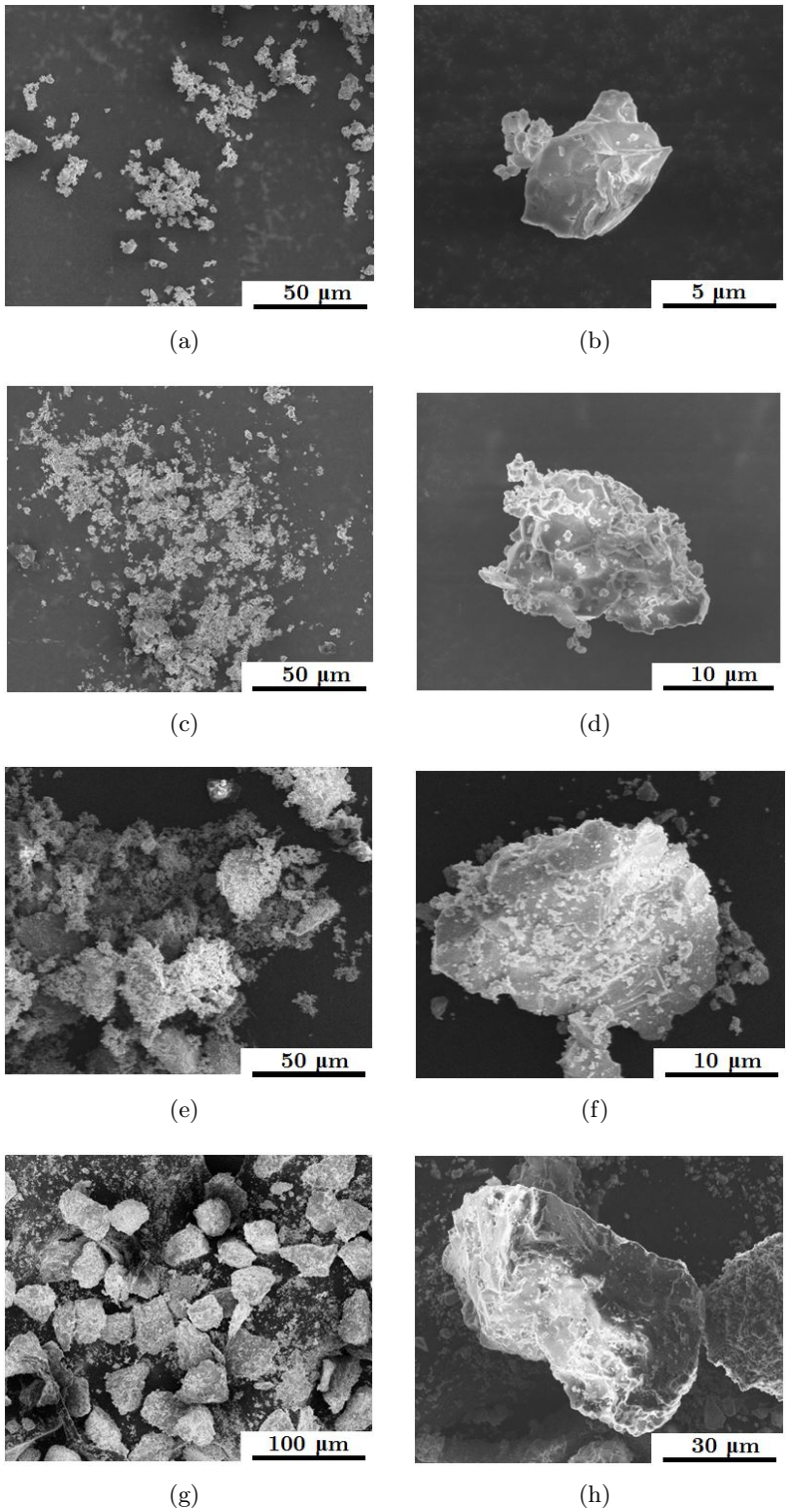

Figure 3.5: Backscattered scanning electron microscopy images for NiZn ferrite for particle size ranges: (a-b) less than 20 µm, (c-d) 20 - 38 µm, (e-f) 38 - 45 µm and (g-h) 45 - 53 µm.

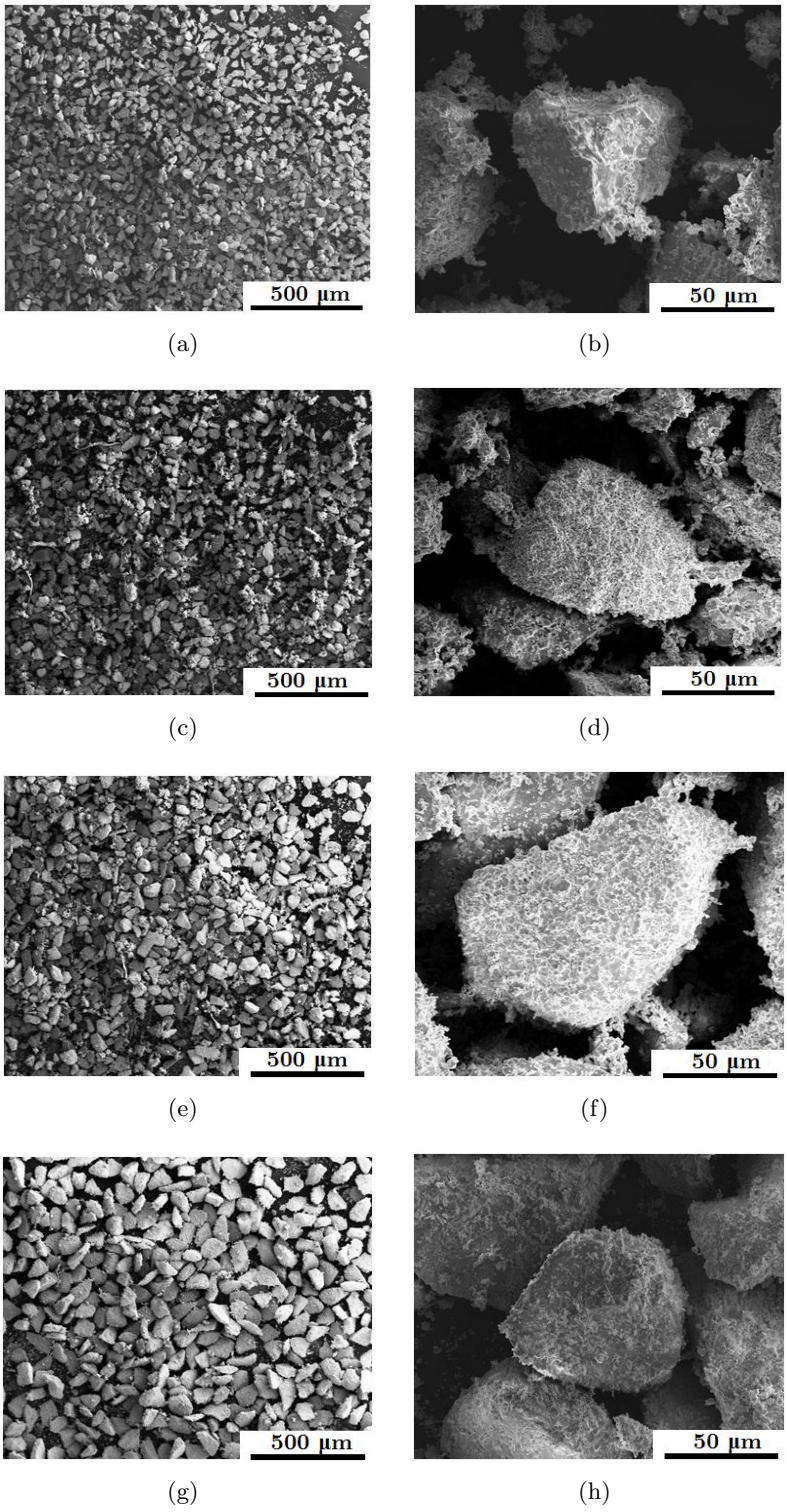

Figure 3.6: Backscattered scanning electron microscopy images for NiZn ferrite for particle size ranges: (a-b) 53 - 63 µm, (c-d) 63 - 75 µm, (e-f) 75 - 90 µm and (g-h) 90 - 125 µm.

by hand in the desired % vol. fraction until all visible evidence of phase separation was removed. The two phase powder mix was placed in a cylindrical, hardened steel mould which had been sprayed with silicone mould release spray. The mix was then pressed in the mould under 55 MPa for 300 s to produce millable composite samples. Each cylindrical sample was then milled into two identical cuboid shapes for material characterisation measurements. Chapter 4 describes the exact sample shape and size along with sample modifications to overcome the problem of air gaps in the stripline. A study of the reproducibility of density measurements and electromagnetic properties is also discussed in Chapter 4. Although ferrite powder and PTFE are used as the filler and matrix materials in this study, the method can also be extended to other inclusions, barium titanate for example as the filler materials and also cellulose powder was tried as an alternative matrix material.

3.5 Fabrication of cubic metamaterials

In Chapters 6 and 7 cubic shaped sub-wavelength metamaterial elements were fabricated to gain independent control of the complex permeability and permittivity. In the following section the fabrication process used to produce both ferrite cube metamaterials and metallic metamaterials is described.

3.5.1 Ferrite cube metamaterial

The metamaterial is a structured form of the MnZn ferrite-PTFE composite material (described earlier in this chapter). The MnZn ferrite and PTFE powders were mixed together with a ferrite volume of 70% and pressed into samples using a steel mould at 55 MPa for 300 s to produce $1 \times 1 \times 1$ cm cubic ferrite composite elements. The cubic elements were placed in two 6×5 arrays with the cube spacing in the x- and y-directions equal to 0.1 mm using double sided polyester adhesive tape. The array is made anisotropic by altering the spacing in the z-direction. It is set between 0.75 and 1.25 mm using a combination of PTFE (0.75 mm thick) and polyester films (each of thickness 0.1 mm). Figure 3.7 shows a schematic of the anisotropic metamaterial stack, it should be noted that in reality only two arrays are fabricated as the ground planes of the stripline in the experimental set-up act as mirror planes.

3.5.2 Metallic cube metamaterial

In Chapter 7, three different metallic cubic metamaterials are used to demonstrate independent control of complex permeability and permittivity. The first, and simplest metallic cubic metamaterial is an array of solid copper cubes which was fabricated by

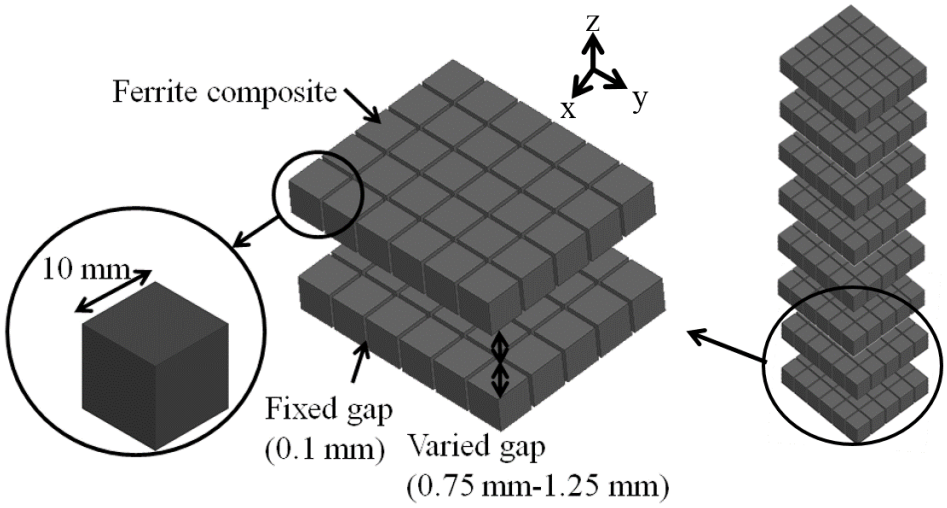

Figure 3.7: Anisotropic array of cubes comprised of ferrite composite material. The cubes are spaced in the x- and y-directions by adhesive tape ($\delta_x = \delta_y = 0.1$ mm), and in the z-direction from the ground plane and signal line using polyester film ($\delta_z = 2 \times 0.75$ mm to 2×1.25 mm).

spacing $10 \times 10 \times 10$ mm solid copper cubes with etched FR4 laminate ($\varepsilon_r = 4.4 + 0.02$i) of thickness 0.8 mm to produce two 6×5 cube arrays. The second and third types of metamaterial contained arrays of hollow structured cubic elements hence a different fabrication method was used. The design of a single element is shown in Figure 3.8 for clarity, however, the details of these structures are discussed in Chapter 7.

To construct an array of these cube elements, the face structure of each element was first etched onto copper-clad FR4 circuit board to produce arrays of 8×8 mm square patches (for the second metamaterial) and 8×8 mm arrays of fifteen electrically connected (0.3 mm) wide rods (for the third metamaterial). The boards were assembled to form two 6×5 arrays. The opposite cube faces were electrically connected through the center of the cube (shown in Figure 3.9).

Two arrays are required for each type of metamaterial due to the stripline measurement geometry, the stripline characterisation is described in the following section. It is noted that the plated and structured cubic metamaterial arrays were fabricated by Nick Cole from the Electromagnetic Materials Group Mechanical Workshop.

3.6 Stripline measurements

In this section the measurement procedure used for deducing the reflection and transmission amplitude coefficients (and ultimately the complex permittivity and per-

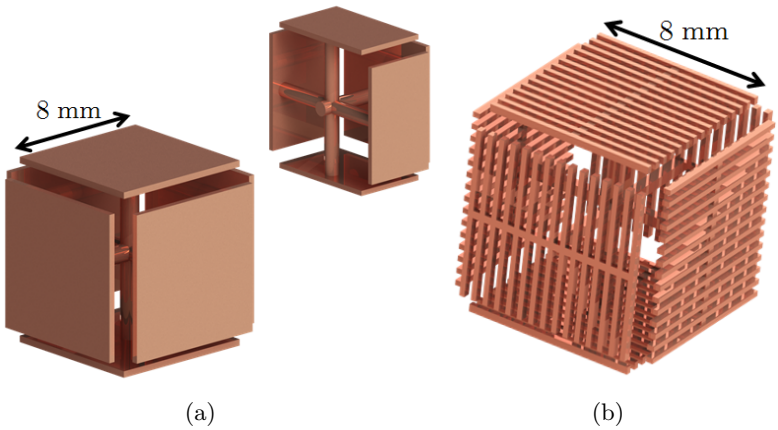

Figure 3.8: Schematic of single structured cube elements; (a) a single structured cube with solid faces with an inset on the internal structure and (b) a single structured cube with faces that have been cut into individual rods.

meability) of metamaterials and composite samples is discussed. Firstly, the stripline geometry is described before moving on to explain the calibration process of the stripline using a Vector Network Analyser (VNA) (VectorStar MS4640A). Later on in this chapter, the extraction method for converting the transmitted and reflected amplitude coefficients to complex permittivity and permeability is discussed.

3.6.1 The stripline geometry

All composite materials and metamaterials in this thesis are electromagnetically characterised using a stripline based on the design by Barry [73], which was developed in 1986. Although the stripline design by Barry was for a fixed height, the stripline used in this study is a variable height stripline, which is shown in Figure 3.10 and consists of a conducting signal line that sits in between a dielectric layer and two conducting ground planes. Each end of the signal line is tapered to a point where the pins and adapters are fitted, allowing the signal line to be electrically connected to the coaxial cables and the VNA as shown in Figure 3.10 (a). Tapering the signal line reduced the reflection amplitude coefficient at the interface between the pin and the signal line in comparison to a rectangular signal line. The dimensions of the stripline are designed to give an impedance of 50 Ohms to match to the coaxial cable impedance and hence minimise reflections at the cable stripline interface. There are three parameters that can be varied to alter the impedance of the stripline; the width of the signal line, the thickness of the signal line, and the height of the stripline. These were all adjusted to maintain the 50 Ohms condition. When the sample height is altered, a new signal

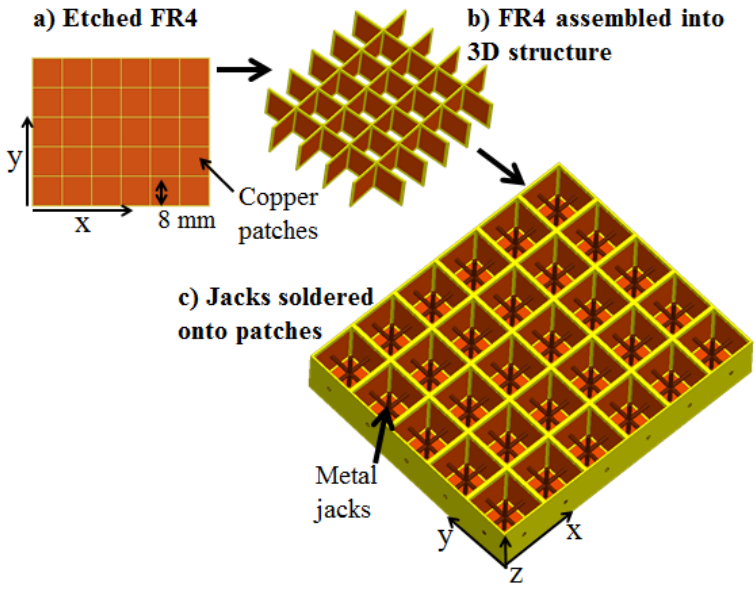

Figure 3.9: Fabrication of structured cubic metamaterials. (a) Single sided FR4 circuit board with 8×8 mm copper squares etched onto the metallic side, (b) etched circuit board cut and assembled into a 3D structure, and (c) central rods are soldered to opposing cube faces, and the top and bottom sheets are attached.

line is used along with four spacers (positioned away from the sample) that can hold the ground planes at a specific distance above and below the signal line to adjust for the new height as shown in Figure 3.10(d). The ability to vary the stripline height allows both the metallic cubic metamaterials and ferrite cubic metamaterials to be electromagnetically characterised in the same stripline. Figure 3.10 (a), (b) and (c) shows the stripline dimensions required for the arrays of metallic copper cubes, the ferrite cubes require spacers to alter the height of the stripline to (71 - 76 mm) as well as the width of the signal line (26 - 21 mm) to maintain the 50 Ohm impedance. The altered stripline system for the ferrite cube arrays is shown in Figure 3.10 (d).

3.6.2 The Vector Network Analyser

The VNA is a device used specifically to measure both the amplitude and phase of reflected and transmitted waves within the frequency range 70 kHz to 70 GHz. The VNA is comprised of a built-in excitation source (provided by the signal generator), a test set and an analyser. The test set takes the output signal from the generator and sends it out of the VNA from either port 1 or port 2, down the phase stable cables to the stripline and sample under test. This signal is either detected back at the same port from which it was sent by an analyser (in the case of a reflected signal) or detected at the opposite port by the analyser (in the case of a transmitted signal). There are

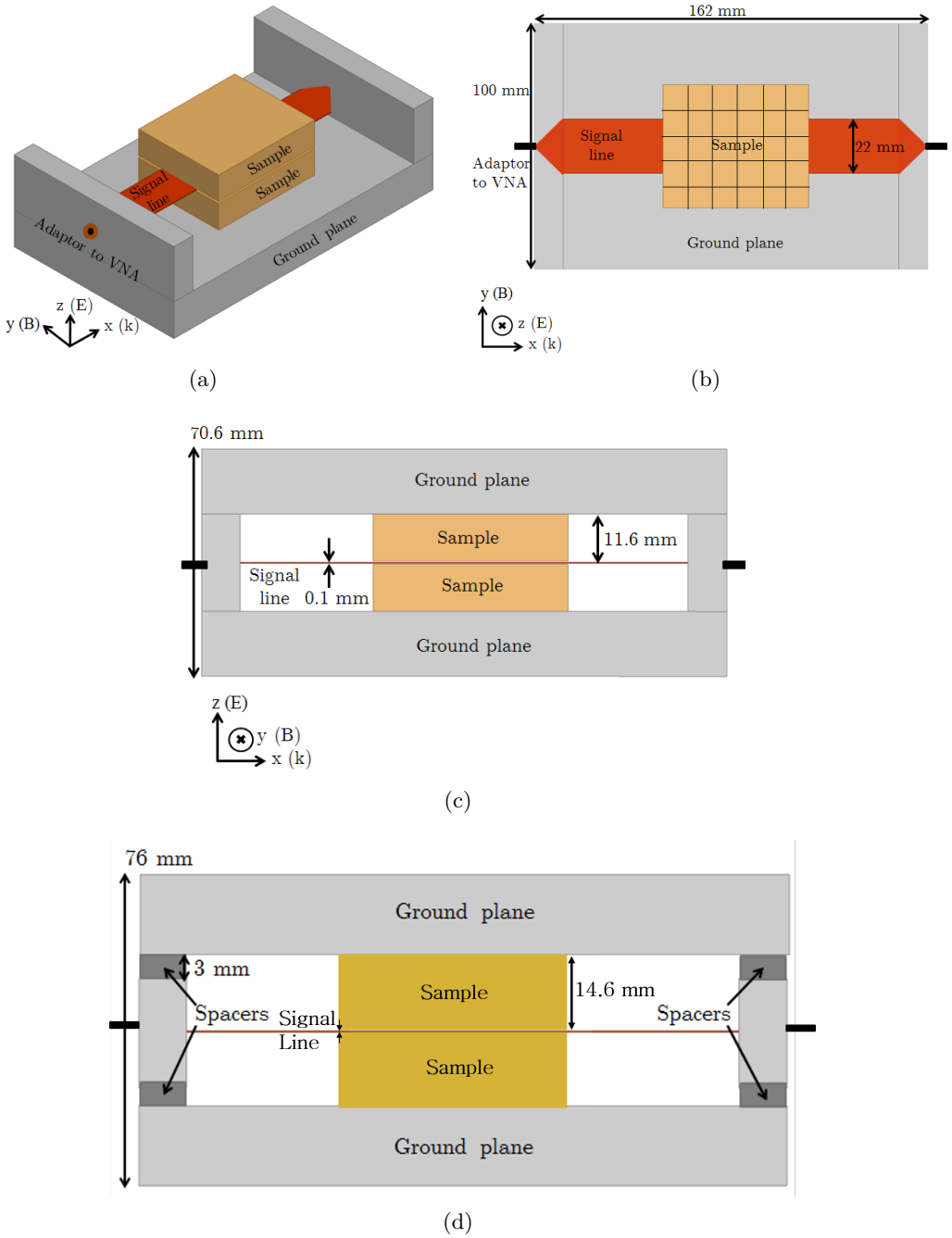

Figure 3.10: Schematic of the stripline set up containing a metamaterial sample: (a) angled view without the upper ground plane shown in order to see inside the stripline, (b) top-down view, (c) side-on view, and (d) side on view with the spacers included. The dimensions of the stripline set-up refer to the metallic cube metamaterial samples.

four S-parameters measured by the VNA; S11, the reflection from port 1 to port 1, S22, the reflection from port 2 to port 2, S12, the transmission from port 2 to port 1 and S21, the transmission from port 1 to port 2. For each of these parameters, the linear magnitude and phase or real and imaginary parts of the wave (the reflection and transmission amplitude coefficients) are measured as a function of frequency. In order to measure phase, the VNA requires a reference channel (R) which is set at the same frequency as the emitted signal. When the VNA receives a reflected or transmitted phase signal, it is compared to the phase of the reference signal. The linear magnitude signal detected at the receiver is given by the % of the original signal.

3.6.3 Calibration of the stripline

The purpose of the calibration is to move the measurement plane recorded by the VNA from the end of the two ports to the end of the two cables, by taking into account the cables and adapters. Before any measurements on samples are performed, the VNA must first be calibrated with four well-defined materials or calibration standards/adapters called the 'short', 'open', 'load' and 'through' with the entire calibration process commonly referred to as the SOLT calibration method. The 'short', 'open' and 'load' are all reflection measurements and are performed on both ports 1 and 2, the 'short' represents a perfectly reflecting boundary (100% reflection), the 'open' represents free space and the 'load' represents a 50 Ohm resistance. The 'through' is the only transmission measurement whereby ports 1 and 2 are directly connected to measure 100% transmission from port 1 to 2 and port 2 to 1. All calibration standards are screwed into the cables and tightened with a torque wrench to a specific torque for consistency between each of the four standards. As the measurements performed are within a stripline placed between the measurement planes, the standard calibration is not sufficient. Introducing a stripline into the system after calibration causes unwanted reflections detected at the ports therefore the stripline is used as a second through measurement as part of the calibration. When the stripline is connected to the calibrated system between the measurement planes, the transmitted phase as a function of frequency observed changes from a horizontal line at zero to a sawtooth which varies between $-180°$ and $+180°$. The gradient of this line is related to the electrical length of the sample, the steeper the gradient, the smaller the spacing between individual peaks and the larger the electrical length. The frequency difference associated with a full cycle in phase (from $-180°$ to $+180°$), provides the necessary information required to deduce the stripline electrical length. The reciprocal of the frequency difference is multiplied by the speed of light to deduce the electrical length. Once the electrical length of the stripline has been calculated, the stripline is calibrated out by setting it as the updated

'through' measurement, this ensures that any reflections observed after calibration are due to the presence of a sample and not the stripline. This completes the calibration, however, a calibration standard (usually PTFE) of known complex permittivity and permeability is measured in the stripline to verify the calibration is correct. Following this, the set-up is then ready for EM characterisation of unknown samples. The VNA measures the reflection and transmission amplitude coefficients (S-parameters) as a function of frequency for the specific material under test. The reflection and transmission amplitude coefficients, along with information about the thickness of the sample (in the propagation direction) and the electrical length of the stripline, are used in the Nicholson Ross Weir extraction method (discussed in the previous chapter) to deduce the complex permittivity and permeability of the sample.

3.7 Extraction of EM parameters

There are two valid methods used in this thesis to electromagnetically characterise composite materials and metamaterials; the Nicolson Ross Weir (NRW) extraction method [67] [68] and a three-layer Fresnel fitting algorithm [74]. For the composite materials and ferrite cube metamaterials the NRW extraction method is used, however, in the case of the metallic cubic metamaterials, both a fitting algorithm based on the three layer Fresnel equations and the NRW extraction method is used to confirm the validity of each methods in the regime of extreme impedance mismatch (where Z is close to 0 or 1).

3.7.1 Nicolson Ross Weir extraction method

The Nicolson Ross Weir extraction method is one of a number of methods that can be used for deducing the electromagnetic parameters from bulk materials. From the complex reflection and transmission amplitude coefficients (S11 and S21 or S22 and S12) together with the frequency and the thickness of the sample, the complex permittivity and permeability can be obtained [75], [76], [77]. The NRW method is used in experimental Chapters 4, 5, 6, and 7 for both parameter extractions in free space and stripline geometries. A Matlab script [74] (programming software language) is used to run the NRW algorithm, with the full NRW derivation located in the previous chapter. The MATLAB script was originally written by Professor Robert Hicken from Exeter University.

Figure 3.11 provides an example of raw experimental linear magnitude and phase data (for both the reflected wave (S11) and the transmitted wave (S21)) recorded by the VNA. The system consists of a stripline connected to a calibrated VNA. The stripline

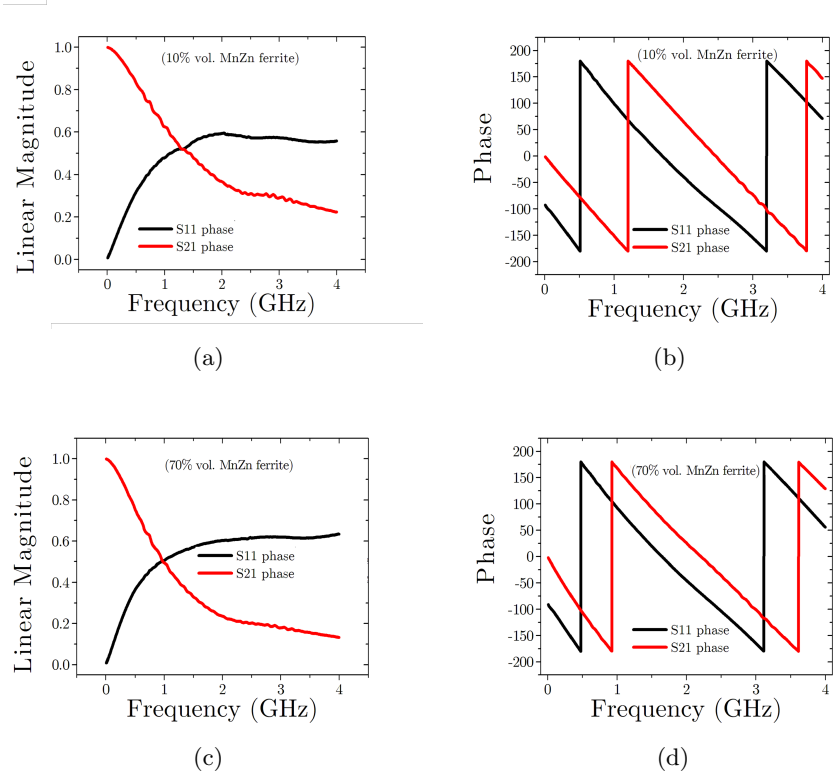

Figure 3.11: (a) Linear magnitude, and (b) phase of both the reflected (S11) and transmitted (S21) wave as a function of frequency for a 10% vol. MnZn-ferrite composite. (c) Linear magnitude for S11 and S21, and (d) phase for S11 and S21 as a function of frequency for a 70% vol. MnZn-ferrite composite. This experimental data was taken via stripline measurements.

is filled with 10% vol. MnZn-ferrite composite (corresponding to Figure 3.11 (a) and (b)) and filled with a 70% vol. MnZn-ferrite composite (corresponding to Figure 3.11 (c) and (d)).

Using the NRW extraction method, the complex permittivity and permeability for both samples were extracted from the linear magnitude and phase. The extracted parameters are shown in Figure 3.12.

3.7.2 Three-layer Fresnel fitting algorithm

The three layer Fresnel fitting algorithm is an alternative method for EM parameter extraction to the well-known NRW method and is used when a system exhibits a large impedance mismatch. Traditionally when solving for complex permittivity and permeability (which are effectively four unknowns), the complex reflection and transmission (four knowns) are manipulated. However, when dealing with the metallic cubic meta-

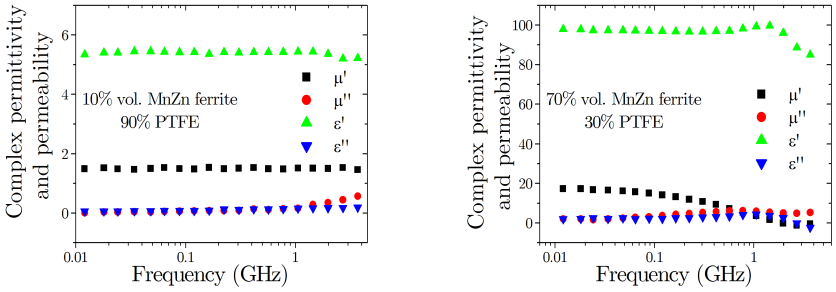

Figure 3.12: Complex permittivity and permeability as a function of frequency for (a) a 10% vol. MnZn-ferrite composite, and (b) a 70% vol. MnZn-ferrite composite. This data was extracted from linear magnitude and phase information using the stripline.

materials, the complex transmission can fall to zero due to Fabry-Perot modes, leading to an impedance mismatch. In this case, uncertainties in the measurement begin to dominate the extracted permittivity and permeability values. Since the impedance of some of the samples used in this thesis was much smaller than that of the empty strip line, both the NRW and the fitting algorithm were used and compared. An important point to note about the three layer Fresnel fitting algorithm is that the effective permittivity and permeability of the samples under test must be non-dispersive in the frequency range of interest. As the copper cubes were not dispersive in the frequency range 10 to 500 MHz the fitting algorithm could be used. The fitting algorithm works by implementing the fmincon function in Matlab [78] and simultaneously fits the real and imaginary parts of the S-parameters to the well-known three layer Fresnel equations for reflection and transmission through a thin slab using the sum of squares difference between the experimental and calculated values as the objective function. The fitting process starts by providing initial guess values of permittivity and permeability, with each iteration the unknown parameters are replaced with a new estimate. The MATLAB script was originally written by Dr Ian Hooper from Exeter University. It was found that results from the NRW method and the fitting routine were consistent with each other for all cubic metamaterial samples with the results shown in Chapter 7.

3.8 Finite element method (FEM) modelling

The finite element method modelling technique used throughout the work presented in this thesis is implemented with Ansoft's commercially available high frequency structure simulator (HFSS) [79]. Finite element modelling (FEM modelling) is a type of

numerical modelling used to simulate EM structures such as antenna designs and radio frequency electronic circuit elements by inputting specific material parameters and geometries. Finite Difference Time Domain (FDTD) is another means to solve EM problems, however, owing to the inherent requirements of the technique (i.e. approximately having cell edge lengths less than or equal to $\lambda/10$ coupled with the need to have at least two cells spanning the finest geometric feature in a geometry to model the structure) it is computationally intensive for the modelling of some metamaterials. FEM model simulations are solved by dividing the 3D space surrounding the model objects as well as the objects themselves into small volumes/cells known as tetrahedra. Each tetrahedron (as illustrated in Figure 3.13 (a)) has a continuous EM field within it's volume which is determined by interpolating the EM field at the tetrahedron's nodes and midpoints between the vertices. The tetrahedra fill the whole model to form a continuous mesh, Figure 3.13 (b) shows an example of the mesh distribution in the FR4 that surrounds an array of copper cubes (as the EM fields do not penetrate the metal a mesh is not required in this region). Although the mesh is generated automatically by HFSS, manual mesh operations are often required to ensure an adequate number of tetrahedra are positioned in small volumes where rapidly spatially varying EM fields are present. A specific example of mesh modifications to the copper cube arrays is shown in Figure 3.13 (c) where mesh operations have been applied to both FR4 and the air box to restrict the maximum size of each tetrahedron in the two separate regions (the maximum size of a tetrahedron in the air box was set to be 10 mm while in the FR4 the maximum tetrahedron size was 2 mm). To match the mesh density at the boundary between the FR4 and the air box, the mesh density gradient in the air box increases up to the boundary, this can also be observed in Figure 3.13 (c).

Once the 3D model has been divided into tetrahedra, HFSS solves Maxwell's equations for each individual tetrahedron and the mesh as a whole. The model is solved many times (up to 10 times in the case of the cubic metamaterials) with each iteration increasing the total number of tetrahedra until the model is converged. As the convergence is based on the user's specification of the number of iterations and the total number of tetrahedra required, errors in the electric and magnetic field distributions may arise when these values have been set too low. The tetrahedra are not added equally throughout the volume, higher densities of tetrahedral are added to areas of high electric/magnetic field intensity. Once the fields have been calculated an S-matrix is produced, which provides information about the transmissivity and reflectivity.

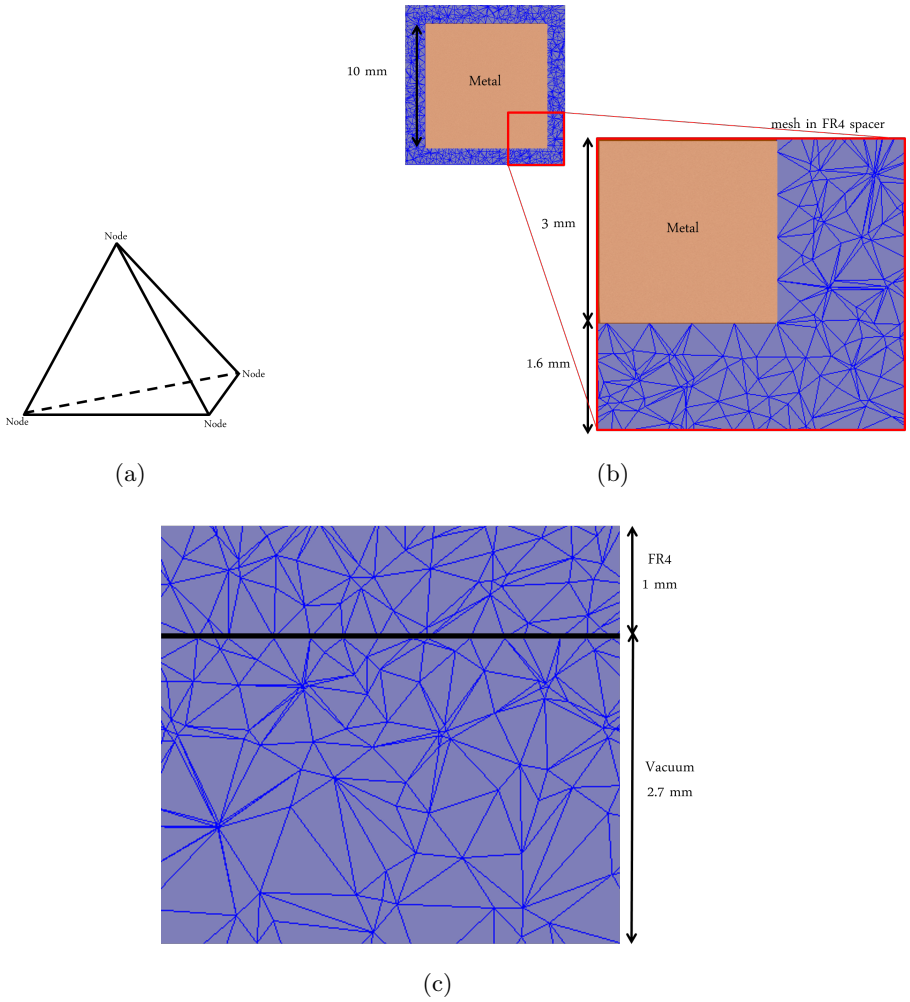

Figure 3.13: (a) An example of a single tetrahedron, (b) cross-section of a single unit cell of an infinite array of copper cubes (metal), surrounded by FR4 circuit board (purple) and (c) the mesh distribution in vacuum and in FR4. Mesh operations are applied in the vacuum to grade the mesh size to match to the FR4.

3.8.1 Assigning materials

HFSS has a library of materials with frequency dependent EM properties. In the case of the metallic cube arrays where copper, FR4 and vacuum were required, the library of materials is adequate. However, when bespoke materials are required, such as the 70% vol. ferrite, 30% vol. PTFE composite material used to model the ferrite cube arrays, the material parameters must be entered manually. Either fixed single frequency material parameters or frequency dependent material parameters can be added to the library which are defined by their complex permittivity (ε) and complex permeability (μ).

3.8.2 Boundary conditions

In this thesis, master slave boundaries are used which impose a repeating boundary condition to the structure which produces an infinite periodic structure. The master-slave boundaries are used in pairs where the incident field applied at the master boundary is the same as the incident field applied at the slave boundary therefore the mesh on the master boundary has to be the same as the mesh on the slave boundary. Master/slave boundary pairs can only be assigned to outer planar faces of the solution space, as well as the geometry that contacts the master boundary being identical to the geometry that contacts the slave boundary. Importantly, master/slave boundaries work for all angles of incidence as the electric field vector does not have to be tangential or normal to these boundaries, the only condition is that the fields on the two boundaries must have the same magnitude and direction.

The location of the master slave boundaries can be seen in Figure 3.14 (b).

3.8.3 Excitation sources

In order to model the cubic metamaterials, Floquet ports are chosen as the excitation source as they can be used in conjunction with master-slave boundaries. The Floquet ports use a set of modes to represent the incident EM field at the port boundary, the modes are dictated by the input solution frequency and produce plane waves that propagate in a direction dictated by the frequency and geometry of the sample. The Floquet ports in this study are positioned at the top and bottom of the air box as shown in Figure 3.14 (b). As Floquet ports can only be used on a structure that is repeated periodically, the structure must be surrounded by the master-slave boundary conditions discussed previously.

3.9 FEM modelling of metamaterials

In this section, the HFSS design used to model metamaterials is described. The same boundary conditions, excitation sources and sample geometry are used to model all the metamaterial samples in this thesis (the exact metamaterial geometries are discussed in Chapters 6 and 7).

The arrays of cubic metamaterials are simulated as 6 cubic elements in the propagation direction and infinitely repeating cubic elements in both the electric and magnetic field directions (imposed by using two sets of master slave boundaries). Two identical Floquet ports are placed at the start and at the end of the array (in the propagation direction) which both emit and detect the incident radiation (see Figure 3.14 (b)). Both the ports are de-embedded to ensure a full number of wavelengths is cycled through before reaching the sample, this is important when it comes to extracting the EM properties as it ensures the radiation from the Floquet port samples only the material of interest i.e. the cube array and not the surrounding air box.

In the case of the ferrite cube array, a combination of library materials (PTFE and air) and manually added materials (ferrite composite material). As the ferrite composite material is dispersive in the MHz frequency range, experimental data for the electromagnetic properties of 70% vol. ferrite composite as a function of frequency was imported into the HFSS materials library (this data is displayed in Chapter 6).

The design used to model the metallic cube metamaterials is very similar to the design of the ferrite cubic metamaterials previously described. This model uses master-slave boundary conditions and Floquet ports as the excitation source. This design was used as the numerical modelling is equivalent to the experimental stripline set-up where the metamaterial is 6 elements long (in the propagation direction) and infinitely long in the electric field direction (achieved in the stripline by the ground planes and central conductor and in the model using the master slave boundary condition). In the magnetic field direction the metamaterial is 5 elements long in the stripline which is greater than the width of the signal line and associated magnetic fields and is approximated to an infinitely wide sample for the model hence a second pair of master-slave boundaries are applied.

The HFSS model was used to calculate both the reflection and transmission amplitude coefficients (the real and imaginary parts of S11, S21, S12 and S22) which were used to extract the effective complex permittivity and permeability of the cubic metamaterials.

Figure 3.14 shows a schematic of the HFSS model used to deduce the reflection and transmission from an array of copper cubes (the same design is used for both types of structured cube visualised in Figure 3.8.

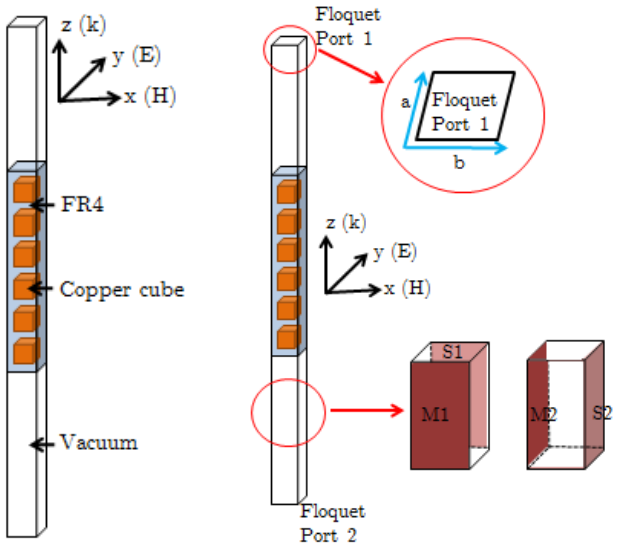

Figure 3.14: Schematic of HFSS model of solid copper cubes; (a) material assignment of the HFSS model, and (b) the location of master-slave boundaries and excitation sources.

3.10 Concluding remarks

In this chapter, some properties of the two different ferrite powders utilised later in this thesis (NiZn ferrite and MnZn ferrite) were described. SEM imaging of the powders was used to look for evidence of clustering and uniform sizing, X-ray diffraction measurements were used to deduce the chemical compositions for each of the powders; and laser diffraction measurements confirmed the particle size distribution. A method for producing ferrite composite materials was outlined before moving onto a description of how the composite materials can be utilised to produce ferrite cube metamaterials. The theme of cubic metamaterials was then extended to discuss the fabrication process of copper cube metamaterials before moving on to the stripline technique used for electromagnetic characterisation of all materials. Finally, a numerical modelling design used to simulate the electromagnetic response of such materials was described in full. The following four chapters will now discuss the experimental work undertaken using these composite materials and cubic metamaterials.

Chapter 4

Heavily loaded ferrite-polymer composites to produce high refractive index materials at centimetre wavelengths

4.1 Introduction

The following chapter investigates the electromagnetic (EM) properties of MnZn ferrite powder in a PTFE (Polytetrafluoroethylene) matrix and in a cellulose matrix. A cold-pressing technique was developed for fabricating such composites with a % vol. of MnZn ferrite which was varied from 0 to 80% for a PTFE matrix and 0 to 85% for a cellulose matrix. The study found that the EM properties at centimetre wavelengths of all prepared PTFE composites exhibited good reproducibility, with the most heavily loaded composites possessing simultaneously high real permittivity ($\varepsilon' = 180 \pm 10$) and real permeability ($\mu' = 23 \pm 2$) at 10 MHz. The permittivity of the cellulose composite at 85% loading was 310 ± 10 at 10 MHz. The complex permittivity and permeability values obtained for the MnZn ferrite composites were then plotted as a function of the % vol. in accordance with the Lichtenecker mixing formula producing an approximately linear dependence. As part of the material characterisation method, the implication of air gaps between the sample and stripline on the extracted EM properties is investigated. The impact of these micron-sized air gaps has led to sample modifications and an analytical description for the system which describes the real permittivity and permeability dependence on the gap size. Lastly, the EM properties of three part composites containing aluminium, MnZn ferrite and PTFE were investigated

with a view to independently controlling the permittivity and permeability of composite samples.

4.2 Background

4.2.1 Electromagnetic Properties of Ferrites

Commercial soft ferrites were introduced in Chapter 1 as ferrimagnetic materials first produced in the 1940s by J. L. Snoek and co-workers [2]. Such materials have been widely used since their production due to their high permeability at low frequencies and low loss (at MHz frequencies) in areas as diverse as telecommunications and antenna systems [80]. Due to their mass production and wide availability commercial ferrites, such as spinel ferrites and garnets, have been investigated extensively in both sintered and composite form [81–85]. The magnetic properties of both ferrite composites and sintered ferrites are strongly dependent on frequency and obey Snoek's law (discussed in Chapter 2) [6] which states that an increase in the static permeability leads to a decrease in the cut off frequency, and vice versa. While Snoek's law is based on the assumption that the particles are single domain and that the enhanced permeability is due to the gyromagnetic spin precession alone, in reality, the enhanced permeability in ferrite composite materials arises from two separate phenomena: gyromagnetic spin precession and domain wall motion. In contrast, the dielectric properties of ferrite composites are dictated by the hopping frequency of electrons within the semiconducting ferrite grains; [86, 87] hence, it is possible to obtain non-dispersive high permittivity values over a greater frequency range in comparison to the permeability.

4.2.2 Fabrication of Ferrite Composites

Although there have been many investigations into ferrite powder-polymer composites [88, 89], PTFE (Polytetrafluoroethylene) and cellulose are infrequently used matrix materials. Both PTFE and cellulose are unusual when compared with other common polymers such as nylon, Perspex, PPS (polyphenylene sulphide) and polypropylene, due to their ability to form compact solids when the powdered form is compressed at room temperature. Whilst previous workers have used PTFE as the polymer matrix for forming MnZn ferrite composites, they have not exploited this solidifying property, and have instead heated the powder mix. For example, Yang *et al.* [90] heated a 45% vol. mixture of ferrite in a PTFE matrix to 350°C for 6 hours before compressing the mixture to form a compacted solid. Cold pressed PTFE composites have been exploited by Youngs [91] to produce dielectric composites; however the % vol. of filler was only varied between 1% and 10%. Cellulose composites have received a great deal of interest in

recent years due to the abundance and low cost of cellulose [92]. Cellulose is lightweight and, unlike PTFE, is biodegradable and possesses outstanding values of strength and stiffness. For these reasons, cellulose composites have been used extensively in both structural and biomedical applications [93–95]. Whilst the production of low volume fraction (below 50% vol.) ferrite composites can be trivially achieved by mixing ferrite powders with elastomers before curing [7], producing high volume fraction (above 70% vol.) composites is more challenging due to the viscosity of the mixture increasing and cannot be achieved by a wet mixing method alone. For example, Tsutaoka [8] details a recipe for producing composites with volume fractions up to 75% vol. of filler using a PPS host matrix that involves mixing the two powders, melting the composite at up to 350°C before pressing the mixture at 1000 kg/cm^2 while allowing it to cool over a 30 minute period. In addition to this added complexity, air can become trapped in the sample, altering the density and electromagnetic properties of the composite. In order to achieve even higher % vol. samples, porous sintered ferrite composites are often used. These samples are comprised of solid sintered ferrite with an air matrix, making the sintered ferrite porous, however, to produce these samples requires temperatures of approximately 1150°C to sinter the powder [9].

4.2.3 Ferrite-Cellulose composites

The following sub-section looks at methods for producing ferrite-cellulose composites with superior structural properties. Methods for producing 80% vol. ferrite-cellulose composites have been reported which can involve complex fabrication techniques [96] [97]. S. Galland *et al.* [98] produced cobalt ferrite-cellulose composites by decorating individual strands of cellulose with ferrite particles. This three hour process involves an in-situ precipitation method that takes place in a chamber heated to 90°C. Pure cellulose fibres are then added to the ferrite-cellulose fibers to dilute the mixture to the desired concentration before the mixure is pressed at 50 MPa for 30 minutes at 120°C. M. Rubacha [99] presents a method for producing barium ferrite-cellulose nanofibre composites. The cellulose was dissolved in N-oxide hydrate at a temperature of 110°C for 80 minutes. The resultant mixture is then spun with barium ferrite at 115°C to produce the barium ferrite-cellulose nanofibres of varied concentrations (between 10 and 50% wt). Both methods described above rely on elevated temperatures and chemical reactions to produce the cellulose composites. Although methods for producing magnetic cellulose composites with superior structural properties are of great interest, if the desired outcome is to produce magnetic composites for EM characterisation, simpler and more time efficient methods are advantageous. S. Liu *et al.* investigated the EM response of nanocomposite fibres containing magnetic Fe_2O_3 par-

ticles dispersed on cellulose fibres. The fibres were set in epoxy to form solid samples with the % vol. of the nanofiber filler varied between 10 and 55% vol.. In the frequency range of 2.0 to 4.3 GHz, the relative real permittivity for a 10% vol. concentration of the nanofibers decreases from 3.20 to 3.05, however, above 4.3 GHz, the permittivity increases to a maximum of 3.35 at 18 GHz. The frequency-dependent permittivity of cellulose composites is indicative of a series of relaxation phenomena that occur due to the water content in the cellulose. The dielectric relaxation that has been observed at low GHz and MHz frequencies can usually be attributed to Maxwell-Wagner-type processes involving charge transfer at dielectric boundaries [100, 101].

The method used for producing PTFE-ferrite composites with % vol. fractions of ferrite filler between 0 and 80% has been outlined in Chapter 3 and is used in this study. It can be highlighted as a unique method for fabricating ferrite composites due to its use across the full range of % vol. of filler. Previous methods for producing composites across a wide range of volume fractions [102] rely on different matrix materials and methods depending on the % vol. of filler which becomes problematic when making direct comparisons between the EM properties of samples. The cold pressing method provides a simple and reliable method for fabrication of electromagnetic materials with user-specified permittivity and permeability values, important in the field of metamaterials. The technique can be extended to many different filler materials and three part composites and avoids the need to use elevated temperatures.

4.3 Methods

In this study, the commercially available sintered MnZn ferrite powder (grade F44) supplied by MagDev Ltd (UK) was used to produce MnZn ferrite-PTFE composites. Extensive tests on this powder presented in Chapter 3, found the phase composition to be $Zn_{0.2}Mn_{0.8}Fe_2O_4$ with some minor impurity phases (Fe_3O_4, Fe_2O_3, MnO). The median ferrite particle diameter was 35 µm while the range of particle sizes spanned from less than 1 µm to 500 µm, with the mean particle diameter of the PTFE powder determined by the manufacturer (Sigma Aldrich Ltd) being 35 µm. The static real permeability and permittivity values as specified by the manufacturer were 1.5×10^3 and 1.0×10^5 respectively. Using the cold pressing technique, five pairs of samples (as the stripline technique requires two identical samples for each measurement) were made for each ferrite fraction to verify reproducibility.

Backscattered scanning electron microscopy (840A SEM, JEOL tungsten filament at 20 kV) images (Figure 4.1) of ferrite composites for (a)-(b) 10% vol. filler and (c)-(d) 70% vol. filler were examined to visualise ferrite particle distribution in the PTFE matrix. Samples were cut using a diamond saw (Isomet 1000, Buehler), mounted

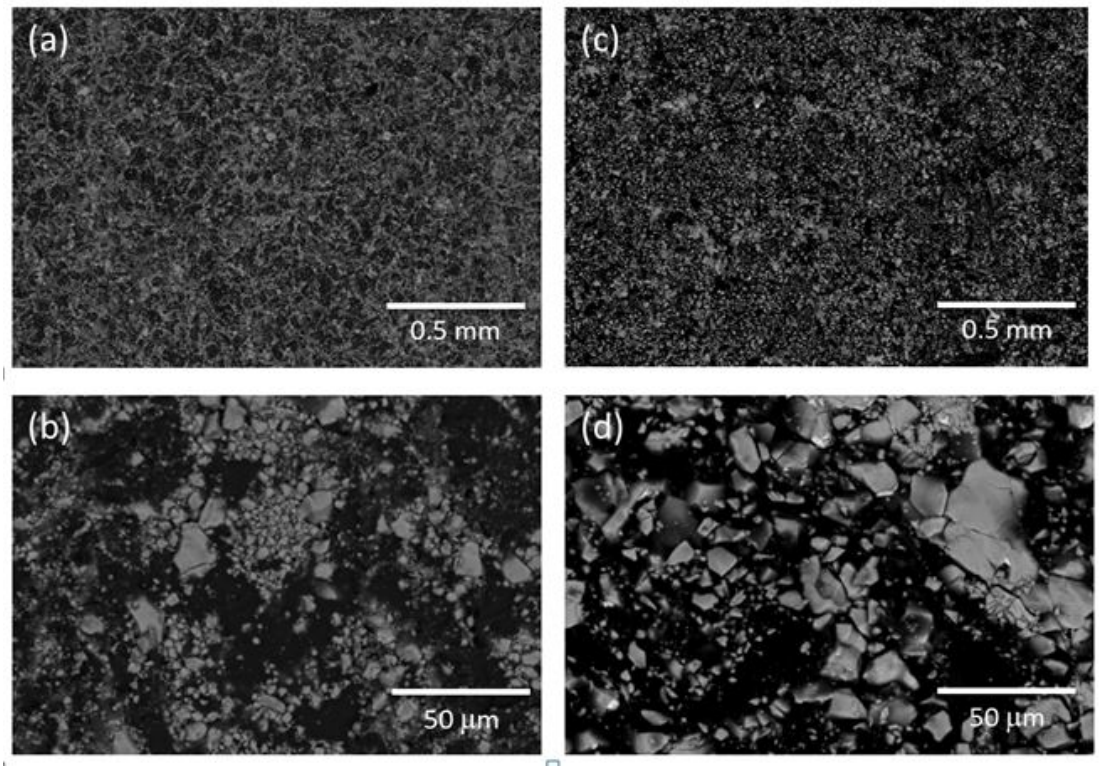

Figure 4.1: Backscattered scanning electron microscopy images showing cross-sections through MnZn ferrite composites of different volume fractions. (a-b) 10% vol. sample; (c-d) 70% vol. sample.

using silver paint and coated with a thin layer of carbon to prevent charging in the SEM. The images show ferrite particles as light regions in the darker PTFE matrix. Although there is evidence of agglomeration of ferrite particles, as well as a slightly uneven distribution, the PTFE has spread throughout the ferrite sufficiently such that there were no large clusters of MnZn ferrite particles.

4.4 The Implications of Air Gaps in the Stripline

Chapter 3 introduced a stripline technique developed by Barry in 1986 [73] that is used to electromagnetically characterise bulk materials, and is used in this chapter to electromagnetically characterise ferrite composites. For stripline characterisation, two identical samples are required with one of the sample-pair positioned above the signal line, and the other sample below. The stripline is connected to a calibrated Vector Network Analyser (VNA) that quantifies the complex reflection and transmission amplitude coefficients of samples. The complex reflection and transmission amplitude coefficients, together with the frequency and the thickness of the sample, allows the

relative complex permittivity and permeability to be obtained using the Nicholson, Ross, Weir (NRW) extraction method [67, 68]. Due to the geometry of the stripline, the sample must be the same height as the distance between the signal line and the ground plane (this distance is parallel to the applied electric field) as shown in Chapter 4.3. If the sample is too small, even on the order of microns, air gaps between the sample and the ground plane will cause erroneous results when deducing the permittivity. Note that these errors are most significant when the permittivity of the sample is large (approximately 50 or larger). The micron sized air gaps are due to the surface roughness, hence the sample will not be uniformly in contact with the ground plane. A simple analytic formula can be used to describe the permittivity dependence on the air gap size. The expression is derived by considering a stack of differing permittivity values and thicknesses of the materials. The electric field (in the $\underline{z}$ direction) is applied perpendicular to the stack of the two slabs, with the total distance in this direction equal to W_z. In the magnetic field direction ($\underline{x}$ direction) and propagation direction ($\underline{y}$ direction) the slabs are infinite in length. It can be assumed that $\underline{D}_z$ is continuous for this geometry and therefore, in the $\underline{z}$ direction;

$$\underline{D} = \varepsilon_1 \underline{E}_1 = \varepsilon_2 \underline{E}_2 \tag{4.1}$$

and

$$\underline{D}_{\text{eff}} = \varepsilon_{\text{eff}} \underline{E}_{\text{eff}} \tag{4.2}$$

By simple manipulation, (derived in full in Chapter 6) one can deduce the following relationship for the measured 'effective' permittivity of the two-material stack where;

$$\frac{1}{\varepsilon_{\text{eff}}} = \frac{1}{\varepsilon_1} + \left(\frac{1}{\varepsilon_2} - \frac{1}{\varepsilon_1}\right)\frac{\delta w}{W_z} \tag{4.3}$$

where ε_{eff} is the effective permittivity of the ferrite sample plus the air gap size, ε_1 is the permittivity of the ferrite composite, ε_2 is the permittivity of the air gap, W_z is the sample size plus the air gap size and δw is the air gap size only. Note that a full derivation of this formula is presented in Chapter 6.

Equation 4.3 shows the importance of removing air gaps between the sample and the ground plane. A simple calculation reveals that δw only needs to be 6 µm to reduce the measured permittivity (ε_{eff}) from 120 to 100 (when $\varepsilon_1 = 120$). In order to remove this influence, the samples were metalised on the top and bottom faces over the area intended to be in contact with the stripline by depositing 60 nm of silver by vacuum evaporation (see Figure 4.3). The metalization provides a continuous conducting plane at the boundary of the composite sample, and ensures that any remaining small air gaps

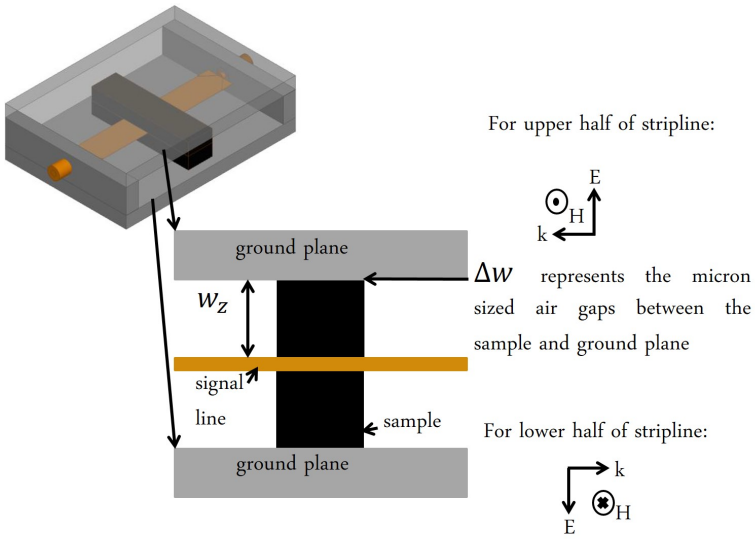

Figure 4.2: Schematic of the stripline geometry with W_z corresponding to the size of the sample plus the micron size air gap and δw corresponding to the micron size air gap.

between the high permittivity samples and the stripline arising from surface roughness are removed. The metalization short circuits gap caused by surface roughness and hence ensures the sample is in complete electric contact with the ground plane

It is not just the permittivity that suffers from air gaps, the permeability is equally sensitive to air gaps arising from the presence of the signal line sitting between the two halves of the sample. An air gap that is of equal size to the thickness of the signal line (100 μm) is sampled by the magnetic field which is applied perpendicular to this gap thickness. Again, a similar equation can be used to describe the permeability dependence on this air gap:

$$\frac{1}{\mu_{\text{eff}}} = \frac{1}{\mu_1} + \left(\frac{1}{\mu_2} - \frac{1}{\mu_1}\right)\frac{\delta x}{w_x} \tag{4.4}$$

where μ_{eff} is the effective permeability of the ferrite sample plus the size air gap, μ_1 is the permeability of the ferrite composite, μ_2 is the permeability of the air gap, W_x is the sample size plus the air gap size and δx is the air gap size only (which is equal to the thickness of the conducting plane). Equation 4.4 is derived in a similar manner to equation 4.3 however, it is now the magnetic field direction which is perpendicular to the two slabs. The two slabs now have differing permeability values and the electric field and the propagation direction are in $\underline{x}$ and $\underline{y}$. Note that the full derivations of equations 4.3 and 4.4 are presented in Chapter 6.

To overcome this problem one sample from each pair has a channel milled down its

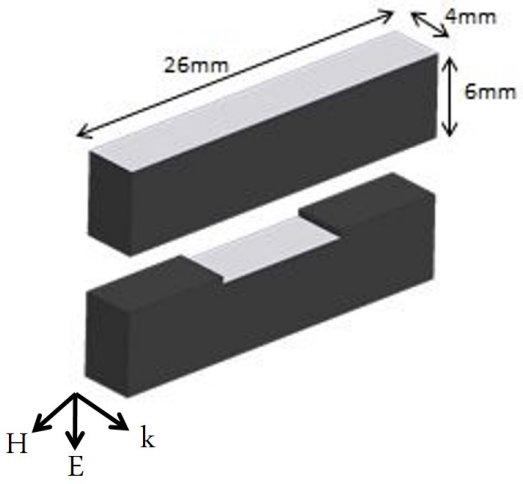

Figure 4.3: Illustration of both halves of the ferrite composite sample pair machined to fit above and below the signal line, for stripline characterisation. Top and bottom surfaces of both parts are metalised with 60 nm of silver over the areas intended to be in contact with the stripline.

center to fit the signal line is also shown in Figure 4.3.

4.5 Experimental Results

To verify that air was not trapped in any of the composite samples, the mass densities, ρ, of the samples was measured by determining the volume (using vernier calipers, capable of measuring to within 0.01 mm, the width, thickness and length of samples were measured at 3 different positions along each axis and averaged) and weight (using an electronic balance sensitive to within 0.1 g). These experimental values were compared with calculated densities to verify whether cold pressing had eliminated all air gaps (Table 4.1). To within the accuracy of measurement, all samples had the expected density, demonstrating that this cold pressing method produces fully dense samples across the full range of ferrite fractions.

The average values of the complex permittivity and permeability for each set of five samples is displayed in Table 4.2 determined by converting the complex reflection and transmission amplitude coefficients obtained from the stripline technique to complex permittivity and permeability using the NWR method (described in full in Chapter 2). The EM properties are given for all 5 different % volume fractions at 50 MHz.

% vol.	ρ predicted (g/cm^3)	Average ρ experiment (g/cm^3)
10	2.46	2.45 ± 0.02
30	2.90	2.87 ± 0.04
50	3.50	3.50 ± 0.02
70	4.02	4.02 ± 0.06
80	4.28	4.28 ± 0.11

Table 4.1: Predicted and experimental data (averaged over five pairs of samples for each concentration with the standard deviation) for densities ρ of ferrite-PTFE composites.

Complex ε and μ	10% vol.	30% vol.	50% vol.	70% vol.	80% vol.
ε'	5.2 ± 0.2	13 ± 1	46 ± 3	96 ± 4	177 ± 10
μ'	1.22 ± 0.20	2.90 ± 0.03	9 ± 1	16 ± 1	21 ± 1
ε''	0.02 ± 0.04	0.25 ± 0.17	0.63 ± 0.25	2.7 ± 1.7	5.2 ± 2.5
μ''	0.97 ± 0.04	0.17 ± 0.04	2.7 ± 0.1	2.8 ± 0.1	4.5 ± 0.3

Table 4.2: Average real and imaginary parts of the relative permittivity and permeability of the composite with standard deviation at 50 MHz determined from the stripline measurements of the sets of 5 samples for each % vol.

The uncertainties associated with the permeability presented in Table 4.2 are likely associated with the consequence of applying high pressures during the fabrication of the composites: it is well known that applying such pressures to soft ferrimagnetic materials like MnZn ferrite can alter their magnetic response [103] by introducing additional anisotropy, causing a shift in the gyromagnetic frequency. Since the fabrication process involves high pressure compression of a powder mix followed by subsequent milling some variations between samples are likely to be exhibited, particularly in the permeability results.

The average real permittivity as a function of frequency for five pairs of samples at each volume concentration is shown in Figure 4.4(a). For all samples, the permittivity remains approximately constant up to a cut-off frequency. Although the permittivity increases with increased % vol. of filler, the cut-off frequency for all the composites is also approximately the same as the concentration of the ferrite does not effect the electron hopping frequency which is localised to individual grains, which collectively form a particle. The ferrite powder consisting of semi-conducting grains encapsulated by dielectric layers. At low frequencies, electron hopping occurs between Fe^{3+} and Fe^{2+} on the octahedral sites [104]. The electrons reach the phase boundaries between the ferrite and PTFE through hopping and thus accumulate at these phase boundaries, which results in interfacial polarisation. As the frequency is increased, the hopping

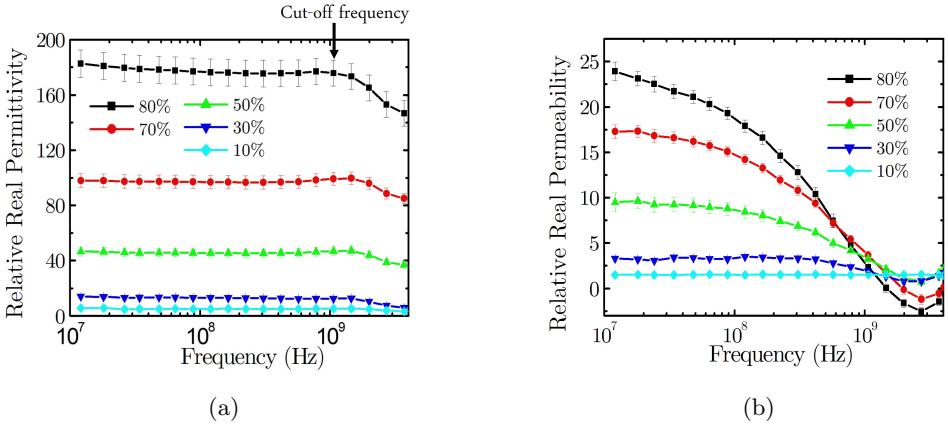

Figure 4.4: Frequency dispersion of (a) ε' and (b) μ' for different % vol. of MnZn ferrite in a PTFE matrix. Results for each % vol. are the average with the standard deviation from separate data sets for 5 independently made composites.

frequency increases until the electrons can no longer follow the applied electric field causing the real permittivity to drop.

The frequency dispersion of the real permeability is displayed in Figure 4.4(b), it is approximately constant from 10 MHz to 100 MHz for vol. % samples up to 70%, and from 10 MHz to 1 GHz for lowest vol. % sample (10% vol.) before dropping rapidly as the domain wall resonance frequency is approached. Note that a full description of the domain wall resonance is discussed in Chapter 2. The simultaneously high permittivity and permeability values at low frequencies make this material an excellent candidate to produce ultra-high refractive index and impedance matched materials required in the field of transformation optics.

The Lichtenecker mixing formula (previously described in Chapter 2 and shown in equations 4.5 and 4.6) is a widely used empirical and analytical model for predicting the filler fraction dependence of the permittivity and permeability of well dispersed composite materials [105, 106].

$$\ln(\varepsilon_{\text{composite}}) = f\ln(\varepsilon_{\text{MnZn}}) + (1-f)\ln(\varepsilon_{\text{PTFE}}) \tag{4.5}$$

$$\ln(\mu_{\text{composite}}) = f\ln(\mu_{\text{MnZn}}) + (1-f)\ln(\mu_{\text{PTFE}}) \tag{4.6}$$

Here f is the volume fraction of ferrite, $\varepsilon_{\text{composite}}$ and $\mu_{\text{composite}}$ are the relative permittivity and permeability of the composite, $\varepsilon_{\text{MnZn}}$ and μ_{MnZn} are the relative permittivity and permeability of the bulk MnZn ferrite, and $\varepsilon_{\text{PTFE}}$ and μ_{PTFE} are the

relative permittivity and permeability of bulk PTFE.

The Lichtenecker mixing formulas are used in this study to plot the complex permittivity and permeability as a function of the filler fraction for a fixed frequency. By inspection of Equation 4.5, a linear dependence between the natural logarithm of the real permittivity and the filler fraction is predicted. Similarly, a linear relationship is predicted between the natural logarithm of the square of the modulus of the complex permeability and the filler fraction is also predicted. The origin of these linear dependencies is shown in Equations 4.7, 4.8, 4.9 and 4.10 and 4.11. The Lichtenecker mixing formulas for the permittivity and permeability in their original form are given below in equations 4.5 and 4.6:

Figure 4.5 illustrates the validity of the Lichtenecker mixing formula for our data by demonstrating the linear relationship between the natural logarithms containing ε' (a), ε'' (b) and μ' and μ'' (c), against % vol. of the ferrite filler. From Figure 4.5 it is possible to predict the permittivity and permeability for this ferrite composite at all % vol.. Note that this logarithmic mixing law has been shown by previous workers for a range of materials including carbon fiber, γ-Fe_2O_3 and carbonyl iron composites [107–109]. Although Birks [108] studied iron-wax composite materials with the % vol. of iron varied between 0 and 60%, it was only the magnetic properties that were studied in relation to the Lichtenecker mixing law. The natural logarithm for the modulus of the permeability as a function of the % vol. of the iron did however show a linear relationship across the full range of % vol. fractions studied. Pitman et al. [109] observed a linear relationship between the natural logarithm of the modulus of the permittivity and the volume fraction for an iron-paraffin wax composite with the % vol. of iron varied between 0 and 25%. However, the logarithm of the modulus of the permeability as a function of % vol. for this composite did not show a linear relationship. The Lichtenecker mixing law fails for very high volume concentrations. Tsutoaka et al. [110] found that a linear relationship was observed between the natural logarithm of the permeability and the volume loading up to 76 % vol., however an exponential increase is observed for volume loadings between 95 and 100 % vol. indicating that the Lichtenecker mixing law is not valid for very high loadings.

To fit to the measurements of ε' in Figure 4.5(a), the relationship stated in Equation 4.7 is utilised, which is derived from Equation 4.5. Here it is assumed that the relative imaginary permittivity of the PTFE is zero and that it may be neglected for the ferrite as the real part is significantly higher than the corresponding imaginary part:

$$\ln(\varepsilon'_{\text{composite}}) = f \ln \frac{\varepsilon'_{\text{MnZn}}}{\varepsilon'_{\text{PTFE}}} \tag{4.7}$$

where $\varepsilon'_{\text{MnZn}}$ is the real part of the relative permittivity of the pure ferrite, $\varepsilon'_{\text{PTFE}}$ is

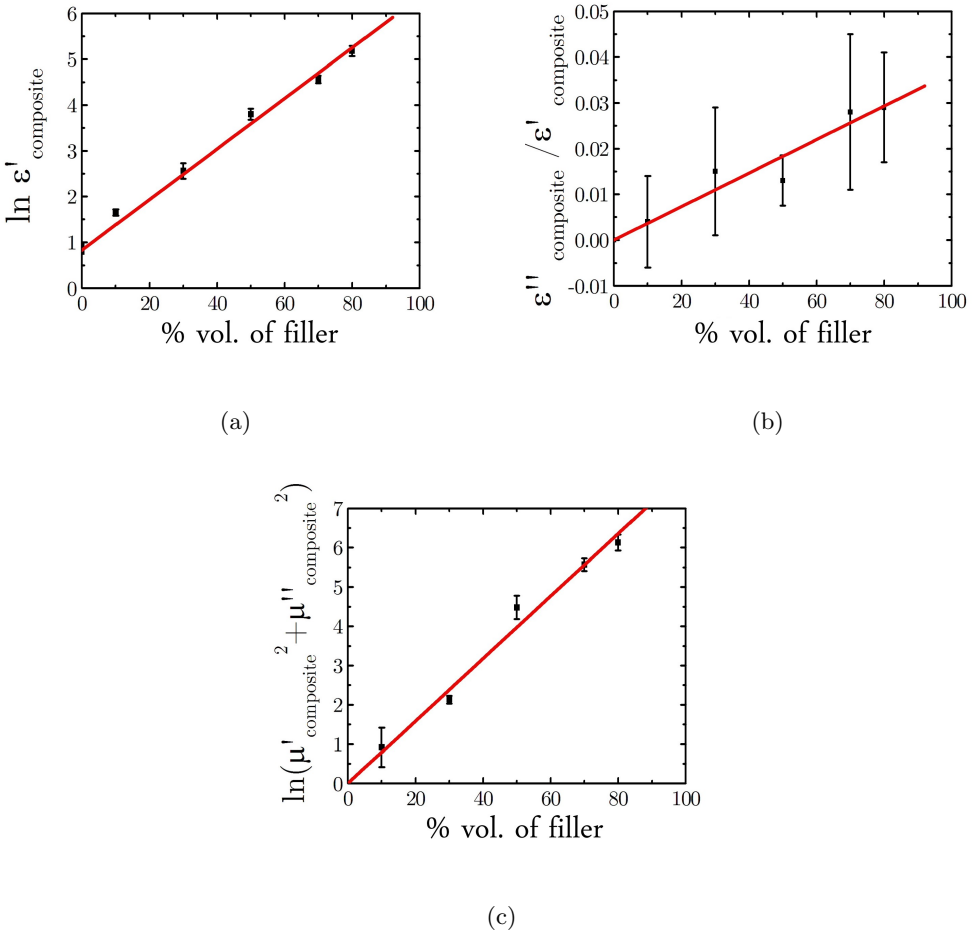

Figure 4.5: (a) Natural log of the average relative real permittivity of the composite samples $\ln(\varepsilon'_{\text{composite}})$ (b) average dielectric loss tangent of the composite $\varepsilon''_{\text{composite}}/\varepsilon'_{\text{composite}}$ and (c) natural log of the modulus of the average relative real permeability squared plus the average relative imaginary permeability squared for the composite $\ln({\mu'_{\text{composite}}}^2 + {\mu''_{\text{composite}}}^2)$ as a function of % vol. at 50 MHz for MnZn ferrite-PTFE composites. The average values represent the mean from 5 independently measured ferrite composite samples.

the real part of the relative permittivity of the pure PTFE, f is the volume fraction of the ferrite and $\varepsilon'_{\text{composite}}$ is the real part of the relative permittivity of the composite. The relationship was obtained as a result of a first order approximation, assuming $\varepsilon''_{\text{MnZn}}$ is much smaller than $\varepsilon'_{\text{MnZn}}$ in the Lichtenecker formula. A first order approximation is possible in this case as MnZn ferrite composites have a dielectric loss tangent of 0.03 (at 80% vol.) or smaller, classifying them as low dielectric loss materials. In order to obtain $\varepsilon''_{\text{composite}}$, the following relationship is used:

$$\frac{\varepsilon''_{\text{composite}}}{\varepsilon'_{\text{composite}}} = f\frac{\varepsilon''_{\text{MnZn}}}{\varepsilon'_{\text{MnZn}}} \tag{4.8}$$

where $\varepsilon'_{\text{MnZn}}$ is the relative real permittivity of the ferrite, and $\varepsilon''_{\text{composite}}$ is the relative real permittivity of the ferrite-PTFE composite at a given volume fraction of ferrite. This relationship was obtained by substituting ε_r into the Lichtenecker mixing formula, and assuming $\varepsilon''_{\text{PTFE}}$ is equal to 0.

The real and imaginary parts of $\mu_{\text{composite}}$ cannot be separated in the same way as for $\varepsilon_{\text{composite}}$ as, in the case of the permeability, the imaginary part is not much smaller than the real part as in the case of the permittivity ($\mu'_{\text{composite}} = 21 \pm 1$ and $\mu''_{\text{composite}} = 1.22 \pm 0.20$). From the Lichtenecker formula, the natural log of the sum of squares for μ'_{MnZn} and μ''_{MnZn} verses the volume fraction gives a linear relationship. This has been presented graphically in Figure 4(c) and analytically using the following relationship (assuming μ'_{PTFE} of PTFE is 1):

$$\ln({\mu'_{\text{composite}}}^2 + {\mu''_{\text{composite}}}^2) = f\ln({\mu'_{\text{MnZn}}}^2 + {\mu'_{\text{MnZn}}}^2) \tag{4.9}$$

where $\mu'_{\text{composite}}$ is the relative real permeability of the composite, $\mu''_{\text{composite}}$ is the relative imaginary permeability of the composite, μ'_{MnZn} is the relative real permeability of bulk ferrite and μ''_{MnZn} is the relative imaginary permeability of bulk ferrite.

To extract the relative real permeability at 100% vol. of filler, two relations containing both μ'_{MnZn} and μ''_{MnZn} terms are solved simultaneously. From the straight line fit from Figure 4.5(c) it is found that:

$$\ln({\mu'_{\text{MnZn}}}^2 + {\mu''_{\text{MnZn}}}^2) = 8 \pm 0.5 \tag{4.10}$$

Also the average magnetic loss tangent for all 5 data sets (10, 30, 50, 70 and 80% vol.) is:

$$\frac{\mu''_{\text{composite}}}{\mu'_{\text{composite}}} = 0.3 \pm 0.2 \tag{4.11}$$

This simple extraction of the effective real part of the relative permittivity and

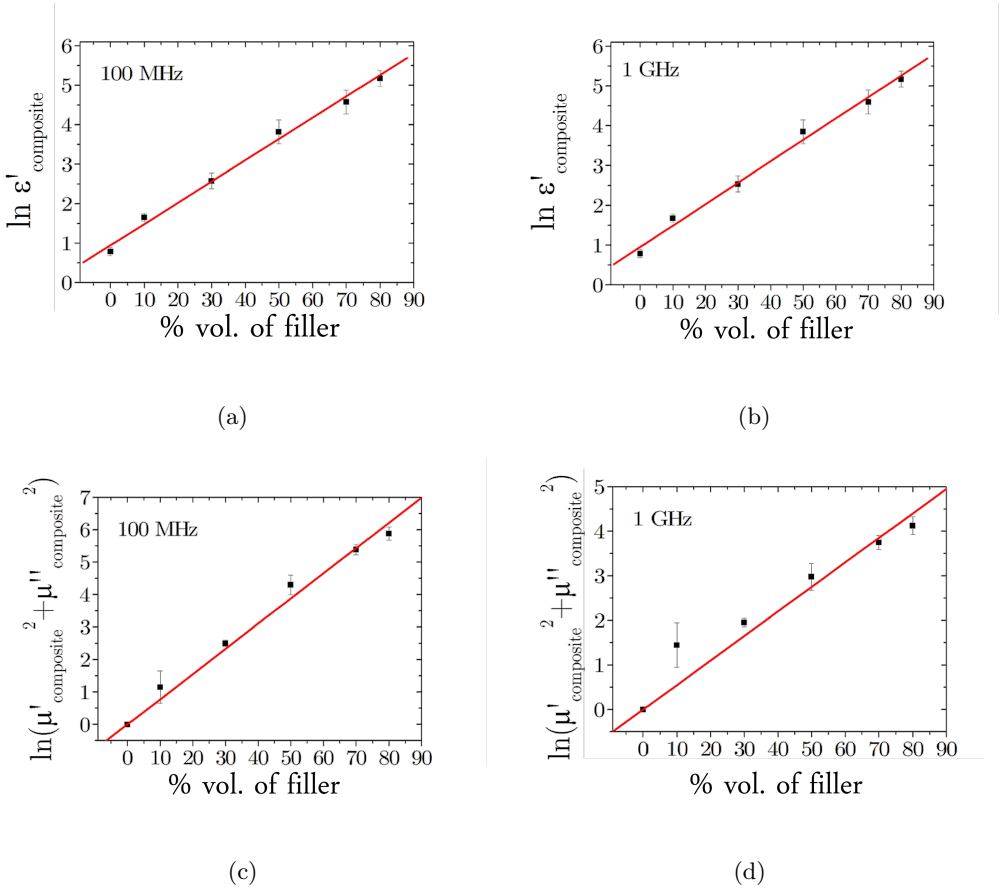

Figure 4.6: Lichtenecker plots for MnZn ferrite - PTFE composite material. (a) $\ln\varepsilon'_{\text{composite}}$ as a function of % vol. taken at 100 MHz, (b) $\ln\varepsilon'_{\text{composite}}$ as a function of % vol. taken at 1 GHz, (c) $\ln({\mu'_{\text{composite}}}^2 + {\mu''_{\text{composite}}}^2)$ as a function of % vol. taken at 100 MHz and (d) $\ln({\mu'_{\text{composite}}}^2 + {\mu''_{\text{composite}}}^2)$ as a function of % vol. taken at 1 GHz.

permeability for 100% vol. of the ferrite allows the estimation of the electromagnetic properties of ferrite composites with any % vol..

Next, the Lichtencker mixing formula has been applied to the MnZn ferrite composite data at 100 MHz and 1 GHz to verify the validity of the linear dependence between $\ln(\varepsilon'_{\text{composite}})$ and $\ln({\mu'_{\text{composite}}}^2 + {\mu''_{\text{composite}}}^2)$ with the % vol. at frequencies where the real permeability is strongly dispersive. The gradient for the permittivity (Figure 4.6(a) and (b)) does not vary as a function of frequency as the complex permittivity is non-dispersive. However, the gradient of the permeability plots (Figure 4.6(a) and (b)) decrease with increased frequency from 0.080 at 10 MHz to 0.078 at 100 MHz and falling to 0.056 at 1 GHz. The decrease in the gradient of the permeability data is due

to the complex permeability being dispersive which is a consequence of the limiting frequency predicted by Snoek's Law (see Chapter 2).

4.6 Alternative Filler and Matrix Materials

In the following section, the cold pressing method is extended to a variety of filler materials such as barium titanate ($BaTiO_3$), aluminium and graphite as well as an alternative matrix material (cellulose). The EM properties of these cold pressed samples are shown below.

4.6.1 Cellulose

The cold pressing method has been trialled with many different polymers as mentioned in Chapter 3 however the only dielectric powder that formed a solid under compression (apart from PTFE) was cellulose powder. Cellulose is one of the most abundant polymers on earth and is found in plant cell walls and algae [111]. It is a polysaccharide composed from long chains of glycosidic bonded glucose units and is widely used as it is a biodegradable material (unlike PTFE) which is cheap and readily available [112]. A systematic study was performed using MnZn ferrite-cellulose composites of varied % vol to compare the EM properties of these new composites with the EM properties of MnZn-PTFE studied earlier in this chapter.

Figure 4.7 shows the frequency dispersion of the relative real permittivity for both cellulose and PTFE. While the permittivity of PTFE is non-dispersive, within this frequency range the permittivity of cellulose decreases approximately linearly with frequency indicating a dielectric relaxation process [113]. Previous studies have found that the permittivity of cellulose is strongly dependent on the water content present within the cellulose and gives rise to a large and frequency dependent permittivity with the higher the water content contributing to larger low frequency permittivities. At frequencies on the order of kHz the enhanced permittivity is due to the polarisability of the water molecules while at frequencies between 10 - 100 MHz, a dielectric relaxation sets in. The relaxation time is strongly dependent on water content as this dictates the distance over which the mobile ions can move and hence the magnitude of the inter-facial polarisation [114–116].

As the permittivity of cellulose is frequency dependent, it will be inherent in any composite materials composed of it. In Figure 4.8 the cellulose has dramatically altered frequency dependent permittivity of the MnZn ferrite-cellulose composite that now decreases rapidly with frequency. Using a matrix with a high permittivity may be of interest for obtaining high refractive index materials since, importantly, it is the

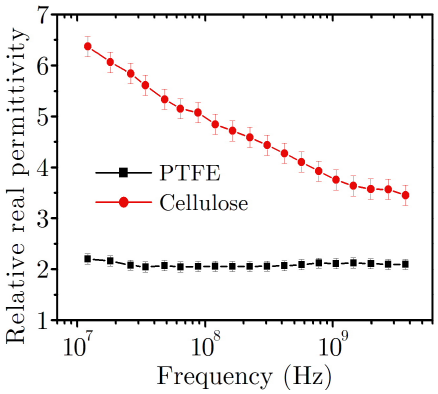

Figure 4.7: Comparison between the frequency dispersion of the average relative real permittivity for cellulose and PTFE matrices only.

product of the matrix and filler permittivities that give the effective permittivity of the composite. Note that the maximum % vol. of ferrite obtained using this method was 85 which is 5% higher than maximum achieved using PTFE. The drawback of this material is the strong frequency dependence that is sensitive to the water content. Figure 4.9 shows the natural log of the average relative real permittivity ($\ln \varepsilon'_{\text{composite}}$) as a function of the percentage volume of the MnZn ferrite. The resulting linear dependence agrees well with the Lichtenecker mixing formula discussed earlier in this chapter and can be used to predict the permittivity of this composite at any concentration of filler. The gradient of the linear plots presented Figure 4.9 decrease systematically with frequency from 0.048 at 10 MHz, to 0.045 at 100 MHz and to 0.044 at 1 GHz. This is due to the the absolute values of $\ln\varepsilon'_{\text{composite}}$ decreasing with increased frequency indicative of the dielectric relaxation in both the ferrite and the cellulose.

4.6.2 Alternative filler materials

Barium titanate is a widely used ferroelectric ceramic with high values of relative real permittivity and low dielectric loss at microwave frequencies [117]. The superior dielectric properties arise from the shift in the Ti^{+} ions from their equilibrium position due to an applied electric field. The position change of the Ti^{+} ions gives rise to permanent electric dipole moments hence increasing the polarisability of the material [118]. It was found that the maximum % vol. of barium titanate powder that could be added to the PTFE powder to form a solid sample when compressed was 50% vol., which is much lower than the maximum % vol. of ferrite. This could be due to the shape and hardness of the filler material. If the filler particles are hard and non uniform in shape, the local pressure at sharp points of the filler particle surface can cause the soft PTFE

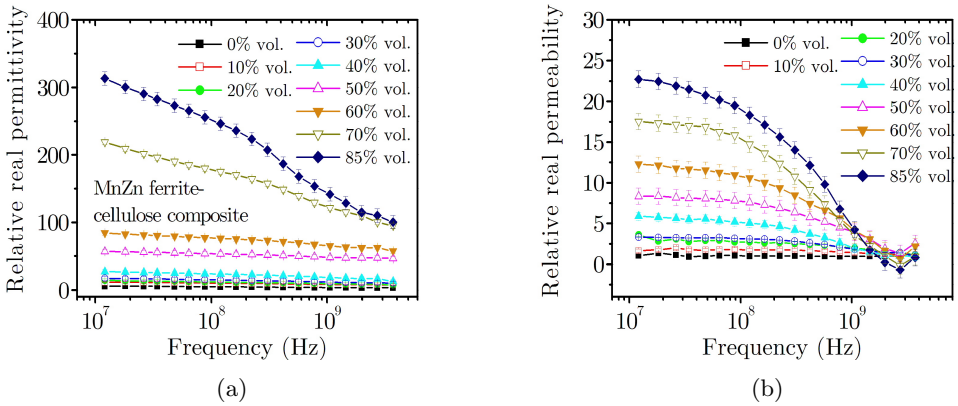

Figure 4.8: Frequency dispersion of (a) the average relative real permittivity, and (b) the average relative real permeability for different % vol. of MnZn ferrite filler in a cellulose matrix.

to deform and flow under pressure. This creates a continuous matrix around the filler particles. It is thought that the local pressures at sharp points are far higher for ferrite than for barium titanate, which leads to the fabrication of higher %vol. fractions for ferrite-PTFE composites. The relative real permittivity of the 50% vol. $BaTiO_3$-PTFE sample was frequency independent (between 10 MHz and 1 GHz) and possessed a value of 31 $\pm$ 5 while the relative imaginary permittivity was 2.1 $\pm$ 0.7. Graphite, iron, and aluminium powders were also trialled as filler materials and found to produce fully dense composites, although due to electrical percolation, these composites were only produced up to 40% vol.. The two main drawbacks of metallic inclusions, in comparison to ferrite, is firstly the high losses at MHz frequencies due to the propagation of eddy currents and secondly, they possess a percolation threshold which severely limits the maximum % vol. fractions obtainable. The purpose of studying the EM properties of ferrite composites was to develop a impedance matched materials with a high permeability, aluminium and graphite are not ferro/ferrimagnetic and hence to not possess a permeability greater than 1.

4.6.3 Three part composites

Three part composites or hybrid polymer composites are a less well studied type of composite that can have superior EM properties over conventional two part composites due to the extra degree of freedom obtained for controlling the permittivity and permeability values [119–124]. Three part composites containing two different ferrite filler materials are investigated in Chapter 5 to achieve impedance matching, while in this

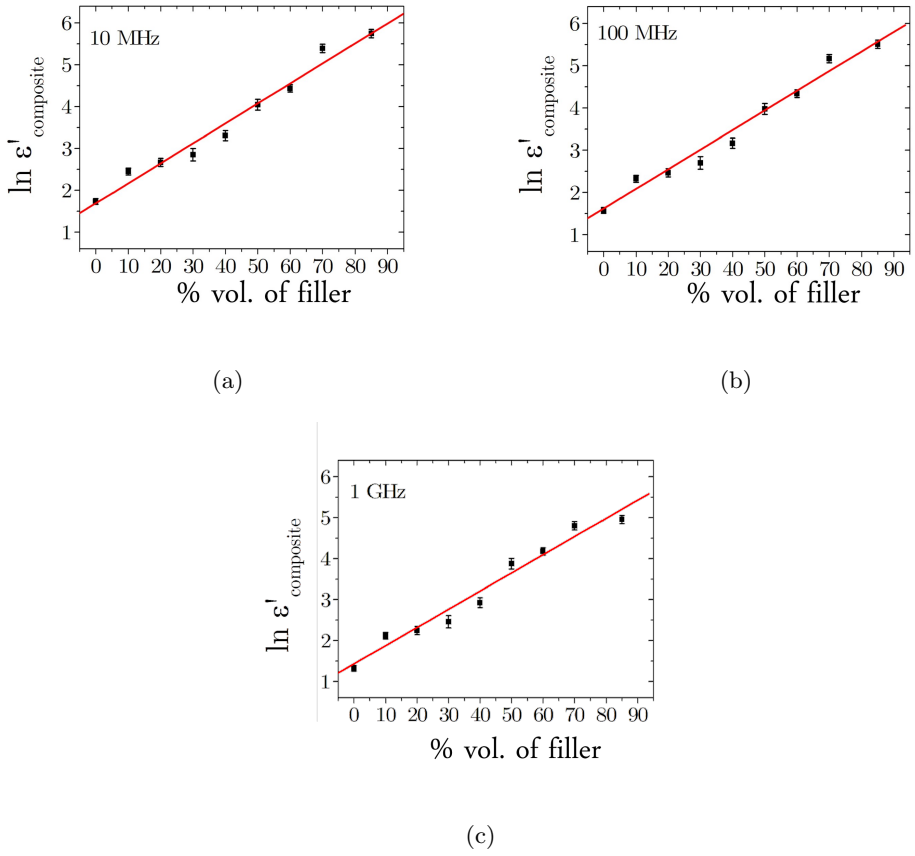

Figure 4.9: Natural log of the average relative real permittivity $\ln(\varepsilon'_{\text{composite}})$ of MnZn ferrite-cellulose composite as a function of the fill fraction of MnZn ferrite at (a) 10 MHz, (b) 100 MHz and (c) 1 GHz.

chapter, aluminium-MnZn ferrite-PTFE composites have been investigated to provide a route to independently controlling the complex permittivity and permeability. Two composites were prepared, one containing 40% vol. MnZn ferrite and 60% vol. PTFE and the second containing 40% vol. MnZn ferrite, 5% vol. aluminium and 55% PTFE. It was found that the addition of aluminum to a ferrite composite increases both the real and imaginary permittivity from 20 ± 1 to 64 ± 3 (for the real permittivity) and from 0.8 ± 0.04 to 13 ± 1 (for the imaginary permittivity) at 10 MHz. The addition of aluminium increases the real permittivity as the aluminium particles are highly polarisable [125]. Capacitive coupling between neighbouring aluminium particles will also enhance the permittivity. It is also noted that the permittivity decreases with increased frequency which is explained by the fact that as the frequency is raised, the inter-facial dipoles have less time to orient themselves in the direction of the alternating

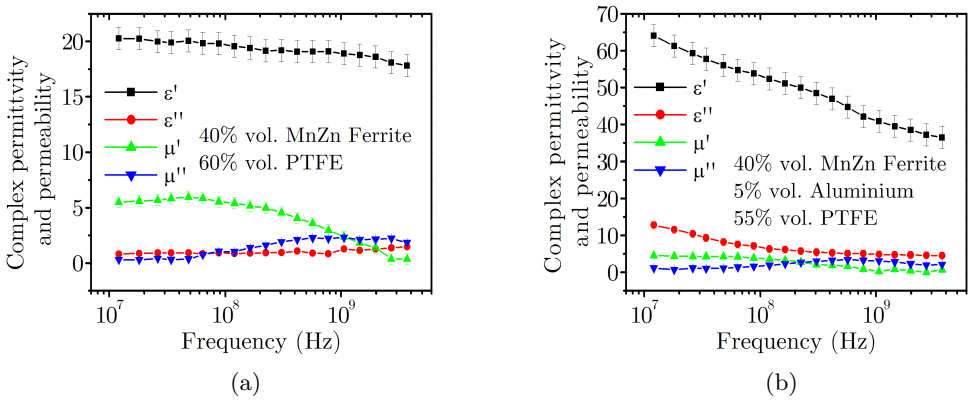

Figure 4.10: Frequency dispersion of (a) the average complex permittivity and permeability for a 40% vol. MnZn ferrite-PTFE composite, and (b) the average complex permittivity and permeability for a 40% vol. MnZn ferrite, 5% aluminum-PTFE composite.

electric field [126]. When the dipoles become out of phase with the alternating field, the material is not longer effective at becoming polarised and hence the permittivity decreases.

The real permeability decreases from 6 ± 0.5 to 5 ± 0.4 with the addition of aluminium suggesting that the aluminium powder is diamagnetic and possesses a permeability of less than 1. The diamagnetic response could be due to the eddy currents inherent within the aluminium particles, however this requires further investigation to confirm the conductivity of the aluminium which varies depending on the amount of oxidation.

4.7 Conclusions

In summary, this chapter presented a simple and time-efficient method for producing composite materials with filler volume fractions ranging from 0 to 80% (for MnZn ferrite - PTFE composites) and 0 to 85% (for MnZn ferrite - cellulose composites). The EM properties of independently manufactured MnZn ferrite - PTFE samples have been compared to demonstrate the reproducibility of this method. The high static permittivity (180±10) and permeability (23±2) of 80% vol. MnZn ferrite - PTFE composites can be used to create high refractive index and impedance-matched devices important in the field of transformation optics. As part of this study, the EM properties of composites containing alternative fillers such as barium titanate and three part composites containing aluminium have also been studied. In the methods section of this chapter,

a flaw in the conventional stripline measurement technique has been highlighted. A new sample design has been proposed to address the problem of micron-sized air gaps in the stripline which impact the extracted EM properties. Permeability and permittivity data for MnZn ferrite - PTFE composites and MnZn - cellulose composites was in accordance with the Lichtenecker mixing formula, allowing it to be used as a way of predicting the EM properties of composites. The ability to predict the EM properties of such composites can be utilised in the manufacture of bespoke materials required in the design and construction of devices based on the principles of transformation optics.

Chapter 5

Tailoring the refractive index of impedance-matched composites

5.1 Introduction

This chapter investigates the effect of ferrite particle size on the electromagnetic (EM) properties of NiZn-ferrite-PTFE composites. NiZn-ferrite powder was sieved in eight size ranges from less than 20 μm up to 125 μm and used to produce composites containing 15, 30, 50 and 70 % vol. concentrations of the sieved NiZn-ferrite filler. Both the relative real permittivity and permeability increase as a function of ferrite particle size for all % vol. concentrations, however, the permeability shows a stronger dependence on the ferrite particle size while the permittivity shows a weaker dependence on particle size.

It was found that the permittivity and permeability could be varied by controlling the ferrite particle size and the % vol. of the ferrite to produce impedance matched composites with refractive index values of 6.1 (for a 50% vol. NiZn-ferrite composite when the average particle size was approximately 35 μm), 6.9 (for a 70% vol. NiZn-ferrite composite when the average particle size was approximately 20 μm).

The Lichtenecker mixing formula is used to show linear dependencies between the natural logarithm of the square of the modulus of the complex permeability and the volume fraction of the sieved NiZn-ferrite filler in the PTFE matrix. In total, 8 separate plots are shown for each particle size/diameter range from less than 20 μmto 125 μm. Similar plots are obtained for the natural logarithm of the real permittivity as a function of the volume fraction of NiZn-ferrite for each particle size/diameter range (taken at a fixed frequency of 20 MHz).

The Lichtenecker plots for permeability were investigated further, with the gradient for each of the eight data sets (corresponding to the eight particle size ranges) plotted

as a function of the average particle size at 20, 100 and 1000 MHz. This was done to observe the effect that Snoek's Law has on the frequency dispersion of the complex permeability for ferrite composites containing different particle size ranges.

Lastly, a high refractive index composite was fabricated to produce equal values of relative real permittivity and permeability. This was achieved by using 3-part hybrid polymer composites containing MnZn ferrite, NiZn ferrite and PTFE. The 3-part composite had a refractive index of 16.5 up to 50 MHz for filler fractions of 15% vol. MnZn ferrite, 65% vol. NiZn ferrite and 20% vol. PTFE.

By being able to manipulate the permeability as well as the permittivity, high refractive index materials (which traditionally rely on tuning the permittivity exclusively (via barium titanate loading for example), adding to loss in most cases) can be created that are impedance matched. By controlling the particle size in two part composites or by introducing a third component, a new degree of control is introduced which allows desired EM properties to be engineered. Such properties are required in transformation optics devices e.g. graded refractive index lenses.

5.2 Background

As discussed in the previous chapter, commercially available soft ferrites have been used extensively in telecommunications and antenna systems due to their simultaneously high permeability and low loss in the MHz frequency range. Ferrites possess large values of relative real permeability at low frequencies (typically up to 100 MHz for a ferrite composite) that is superior to iron due to the high resistivity of ferrites as discussed in Chapter 2 [80]. Despite ferrites providing an enhanced permeability within the MHz frequency range, many systems that typically operate at GHz frequencies would benefit from extending the frequency range over which the permeability remains high [127]. The reason for the permeability diminishing at higher frequencies is the onset of the domain wall resonance. As previously discussed in Chapter 2, there exists a trade off between the cut off frequency and the low frequency permeability known as Snoek's Law [6]. This simple law, based on an induced magnetic resonance that occurs in a fully magnetised spherical body, provides an upper limit for how large the real permeability can be at a given frequency. Since Snoek's original paper, there have been many studies on extending the Snoek limit in materials so that the real permeability may remain large at higher frequencies (above 100 MHz) [58, 128, 129]. Snoek's original law does not take into account any physical properties of the ferrite e.g. the size or the shape of the ferrite particles in the composite and how these features may affect the magnetic properties of the composite and the corresponding cut off frequency. Hence research into extending the Snoek's Limit by using non-spherical particles has been

conducted [129].

R. Dosoudil et al. [130] investigated the effect of the particle size and concentration on the complex permeability of 'hybrid' ferrite polymer composites. Three sets of composite samples were fabricated, each containing a different % vol. of a dual ferrite filler (MnZn and NiZn ferrite) in a PVC matrix. For each % vol. of the dual ferrite filler, three different ferrite particle size ranges were used (0 - 40 μm, 40 - 80 μm and 80 - 250 μm). As the ferrite particle size is increased, the relaxation frequency of the permeability decreased from 361 MHz (for the sample containing ferrite particles within the size range 0 - 40 μm) to 247 MHz (for the sample containing ferrite particles within the size range 80-250 μm). The real permeability at 20 MHz increased from 16 (for 0 - 40 μm sized particles) to 20 (for 80 - 250 μm sized particles).

A similar study by R. Dosoudil et al. [131] also investigated the particle size and concentration effect of LiZn/MnZn ferrite composite on complex permeability. It concluded that while the particle size of the ferrite weakly affected the frequency dispersion of the permeability, the concentration of the dual ferrite filler had a far stronger effect. These two studies by Dosoudil which measured permeability as a function of ferrite particle size follow the trend predicted by Snoek's Law as there is a trade off between the initial permeability and the cut off (resonant) frequency. This behaviour suggests that for a given % vol. of ferrite filler in a composite, the intrinsic magnetic properties, e.g. the coercivity and saturation magnetisation will differ depending on the size of the magnetic inclusions.

J. Slama et al. [132] investigated the coercivity and initial permeability (at 100 kHz) as a function of grain size for a bulk-sintered NiZn ferrite. A linear relationship between the initial permeability and the grain size (for a grain size range of 2-15 μm) was observed while an inverse relationship was observed between the coercivity and the grain size. This result indicates that the intrinsic magnetic properties are dictated by the microstructure of the ferrite which is discussed later in this chapter.

It is not just the magnetic properties that are affected by the ferrite particle size in composites, the dielectric properties are also altered. The effect of particle size on both the real permeability and permittivity of hexagonal ferrites has been investigated. B. W. Li et al. [133] controlled the particle size of a hexagonal ferrite ($Ba_3Co_2Fe_{24}O_{41}$ or Co_2Z) in a polyvinylidene fluoride polymer matrix over the three particle size ranges; 75 - 150, 38 - 50 and 10 - 30 μm. The real permeability increased from 3 (for a 70% vol. composite with a ferrite particle size range of 10 - 30 μm) to 4.8 (for a 70% vol. composite with a ferrite particle size range of 75 - 150 μm) at 20 MHz while the corresponding permittivity also increased from 50 to 75 (also at 20 MHz).

5.3 Method

5.3.1 Fabrication technique

In this study, the commercially available sintered NiZn-ferrite powder (grade F16) which is supplied by MagDev Ltd (UK), was used to produce NiZn-ferrite-PTFE composites in the same way as the MnZn-ferrite-PTFE composites were made in Chapters 3 and 4. In Chapter 3, X-ray diffraction measurement results were presented which found the phase composition to be $Ni_{0.4}Zn_{0.6}Fe_2O_4$ with minor impurity phases NiO_2, ZnO_2, Fe_2O_3 and Fe_3O_4. Laser-diffraction measurements, also presented in Chapter 3, show that the median ferrite particle diameter of the unsieved NiZn ferrite powder was 4 μm, with the mean particle diameter of the PTFE powder determined by the manufacturer (Sigma Aldrich Ltd) being 35 μm. The static values of permeability and permittivity as specified by the manufacturer were 125 and 100 respectively. In order to investigate particle size dependencies, NiZn ferrite powder was sieved using a stack of metal sieves of varying mesh size (125 - 90, 90 - 75, 75 - 63 and 63 - 53 μm). The smaller particle size ranges (53 - 45, 45 - 38, 38 - 20 and less than 20 μm) were obtained by MagDev Ltd (UK) using the same batch of NiZn ferrite powder. The sieves were stacked in increasing mesh size and attached on top of a vibrating plate. The unsieved power was fed in at the top and the sieved powder is collected in each sieve. The average particle size for each sieved fraction was measured using the Laser Diffraction method presented in Chapter 3.

Figure 3.4 plots the % volume of ferrite as a function of the equivalent spherical diameter of the particles and shows a series of Gaussian shaped curves, with the peak of each curve agreeing with the mesh sieve size. The uncertainty of the average particle size for each size range is obtained by using the full width half maximum value deduced from Figure 3.4. Each sieved NiZn ferrite powder fraction is mixed with PTFE in the following % volume fractions; 15, 30, 50 and 70, to produce 32 individual samples (8 per volume fraction). The cold pressing technique, introduced in the previous chapter (Chapter 4) was used to produce the solid composite samples.

5.3.2 Electromagnetic characterisation

The samples are electromagnetically characterised using the stripline technique developed by Barry [73] and introduced in Chapter 3. This technique is used in Chapters 4 and 5 to electromagnetically characterise bulk materials and in Chapters 6 and 7 to electromagnetically characterise metamaterial samples. Each of the samples fabricated is divided into two identical samples as one of the sample-pairs is required to sit above the signal line, and the other sample below. The stripline is connected to a calibrated

Vector Network Analyser (VNA) that quantifies the complex reflection and transmission amplitude coefficients of samples. From the complex reflection and transmission amplitude coefficients together with the frequency and the thickness of the sample, the relative complex permittivity and permeability can be obtained using the Nicholson, Ross, Weir (NRW) extraction method [67, 68] (see Chapter 2).

5.4 Experimental Results

5.4.1 Permittivity and permeability dependence on ferrite particle size and volume fraction

Figure 5.1 shows the relative real permittivity and permeability as a function of the average NiZn-ferrite particle size for a NiZn-ferrite-PTFE composite at 20 MHz for (a) 15% vol., (b) 30% vol., (c) 50% vol. and (d) 70% vol.. All four plots show that both the permeability and permittivity increase as a function of the NiZn ferrite particle size however, the permeability is more sensitive to the increase in particle size in comparison to the permittivity, for example, in Figure 5.1 (d), the permittivity increases from 7.0 (for an average particle size of 4.2 μm) to 7.9 (for an average particle size of 147 μm) while the corresponding permeability value increases from 5.5 to 12.5 for the same particle size increase. The increase in permeability with increased particle size can be understood by considering the distribution of the demagnetising fields for particles containing differing numbers of domains. In general, the fewer the number of domains, the further the demagnetising fields extend outside of the particle and thus the larger the net demagnetising field, resulting in a smaller permeability.

The domain structure and number of domains is dictated by the internal energy of the particle. The magnetostatic energy and the exchange energy are in competition, the magnetostatic energy is minimised by diving the particle into more domains and the exchange energy is minimised by aligning adjacent spins, which is discussed in Chapter 2. In most materials the domains are generally microscopic in size and range between 10^{-4} and 10^{-6} m [2], and in ferrites, the domain size can be the same size as the particle. Studies into the domain structure of MnZn ferrite have found that monodomains exist in grains that are approximately 4 μm or less in size. Above this grain size, the grains became polydomain in structure [2].

The domain structure affects the coercivity of the ferrite particle, which can also impact the permeability. The coercivity is a measure of the magnitude of the applied magnetic field required to reduce the magnetisation of a material to zero after the magnetization of the sample has been driven to saturation.

For larger particle sizes (which are multi-domain), the coercivity decreases as the

particle subdivides into domains, in general, the larger the particle, the more domain subdivisions are present. The coercivity is large for small particles (which tend towards the single domain limit) as it is energetically hard to change the direction of the magnetisation vector of a single domain particle, or a particle with few sub divisions. This is because a relatively large amount of energy is required for complete rotation of the magnetisation vector within the particle. The coercivity is lower for multi-domain particles as translating the domain walls is an energetically easy process that can be achieved in relatively low fields. Therefore, the more subdivisions of the particle into domains, the less energy is required to fully magnetise the particle. Multi-domain particles have the characteristics of magnetically soft materials while the single-domain particles, and particles with few domains have the characteristics of magnetically hard materials [134, 135]. In general, magnetic materials with a low coercivity value possess a large permeability [136] as they can be magnetised more easily, hence larger particles containing more domains have a lower coercivity and higher permeability. Characterising the coercivity of ferrite composites is discussed in Chapter 9.

Figure 5.1 also shows a weak dependence on the permittivity with increased particle size. The increase in permittivity with increased particle size can be understood by considering the grain structure within each of the ferrite particles. It has previously been discussed (in Chapters 2 and 4) that the dielectric properties of ferrite originate from the grain structure, which is composed of semi-conducting grains where an electron hopping process takes place and from insulating grain boundaries that act to separate charge and behave as capacitors. It has been documented that the presence of the grain boundaries greatly increases the permittivity response of the ferrite, as capacitive effects arising from the separation of the charges enhance the permittivity. The larger ferrite particles in this study are composed of more grains and insulating grain boundaries compared to smaller ferrite particles, and in some cases, very small particles (less than 10 μm) can be mono-grain. Therefore, the permittivity of the smaller ferrite particles is reduced since the capacitive effects, which enhance the polarisability, are reduced due to the reduction in the number of grain boundaries.

Figures 5.1 (c) and (d) demonstrate that by controlling the ferrite particle size, the permittivity and permeability can be set equal, thereby providing an impedance-matched material (assuming the ferrite composite is low loss and the imaginary permittivity and permeability are both near zero). At 20 MHz, for a 50% vol. NiZn ferrite composite, the impedance matched condition occurs when the average particle size is approximately 35 μm (with a corresponding refractive index of 6.1), and in the 70% vol. NiZn ferrite composite, this condition occurs for an average particle size of approximately 20 μm (with a corresponding refractive index of 6.9). These figures demonstrate that impedance matching can be achieved for a variety of different refrac-

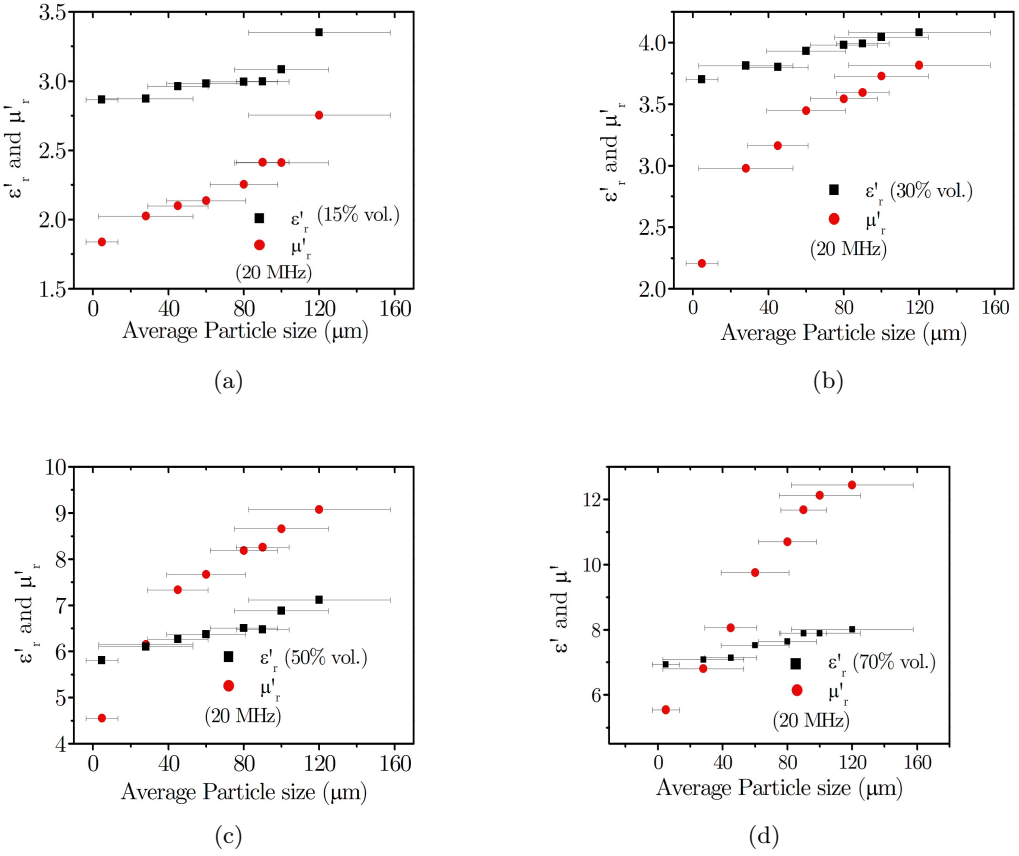

Figure 5.1: Plots of the relative real permittivity (ε') and permeability (μ') as a function of the average NiZn ferrite partice size for a NiZn ferrite-PTFE composite at 20 MHz for (a) 15 %vol., (b) 30 %vol., (c) 50 %vol. and (d) 70 %vol..

tive index values by controlling both the % vol. and particle size of NiZn ferrite. Later in this chapter, equalising of the permittivity and permeability is demonstrated by the addition of a third component, with a resulting refractive index for the three-part composite equal to 16.

The data from Figure 5.1 can be represented as two-colour magnitude plots to show how both the permeability and permittivity vary as a function of both particle size and % vol. of ferrite filler simultaneously. The colour magnitude contrast indicates the value of (a) the real permittivity and (b) the real permeability and is shown in Figure 5.2. Figure 5.2(a) shows that μ' is more sensitive to the average particle size of the ferrite in comparison to ε', which is less sensitive to this factor, however, as the colour magnitude varies along the x - axis (in the direction of increasing particle size) for both Figure 5.2 (a) and (b), both μ' and ε' increase as a function of average particle size.

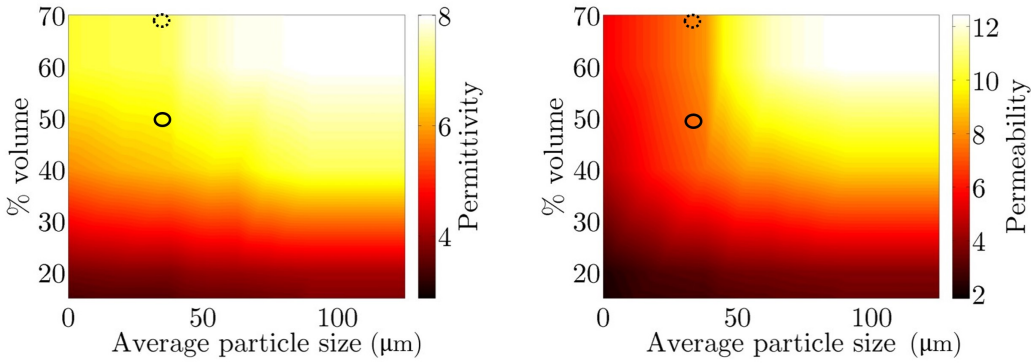

Figure 5.2: Colour magnitude plot of % vol. of NiZn ferrite filler in a PTFE matrix with the colour contrast indicating the value of (a) the relative real permittivity and (b) the relative real permeability at 20 MHz. The two black circles on each of the colour plots represent the impedance matched condition whereby the permittivity and permeability are equal for a given % vol. and particle size.

5.4.2 Fitting the Lichtenecker mixing formula to experimental data for different particle size ranges

The Lichtenecker mixing formula, previously discussed in Chapters 2 and 4, can be used to model the filler fraction dependence of the permittivity and permeability of well dispersed composite materials [105, 106]. It is used in this study to plot the real part of the permittivity and complex permeability as a function of the filler fraction for a fixed frequency. In their original form, the Lichtenecker mixing formulae for the permittivity and permeability as a function of the filler material are expressed as the following;

$$\ln(\varepsilon_{\text{composite}}) = f\ln(\varepsilon_{\text{NiZn}}) + (1-f)\ln(\varepsilon_{\text{PTFE}}) \tag{5.1}$$

$$\ln(\mu_{\text{composite}}) = f\ln(\mu_{\text{NiZn}}) + (1-f)\ln(\mu_{\text{PTFE}}) \tag{5.2}$$

where f is the volume fraction of ferrite, $\varepsilon_{\text{composite}}$ and $\mu_{\text{composite}}$ are the relative permittivity and permeability of the composite, $\varepsilon_{\text{NiZn}}$ and μ_{NiZn} are the relative permittivity and permeability of the bulk NiZn ferrite, and $\varepsilon_{\text{PTFE}}$ and μ_{PTFE} are the relative permittivity and permeability of bulk PTFE. Equations 5.1 and 5.2 can be re-written to describe a linear dependence between the natural logarithm of the real permittivity and the filler fraction (in the case of Equation 5.1), and a linear relationship between the natural logarithm of the square of the modulus of the complex permeability and

the filler fraction (in the case of Equation 5.2). The resulting equations (Equations 5.3 and 5.4) are used to produce Figures 5.3 and 5.4.

Figure 5.3 shows plots of the natural logarithm of the real permittivity as a function of the % vol. of NiZn ferrite in a PTFE matrix for the eight particle size ranges; (a) less than 20 μm, (b) 20 - 38 μm, (c) 38 - 45 μm, (d) 45 - 53 μm, (e) 53 - 63 μm, (f) 63 - 75 μm, (g) 75 - 90 μm and (h) 90 - 125 μm.

Figure 5.4 shows plots of the natural logarithm of the square of the modulus of the complex permeability as a function of the % vol. of NiZn ferrite in a PTFE matrix for the same eight particle size ranges; (a) less than 20 μm, (b) 20 - 38 μm, (c) 38 - 45 μm, (d) 45 - 53 μm, (e) 53 - 63 μm, (f) 63 - 75 μm, (g) 75 - 90 μm and (h) 90 - 125 μm.

$$\ln(\varepsilon'_{\text{composite}}) = f \ln \frac{\varepsilon'_{\text{NiZn}}}{\varepsilon'_{\text{PTFE}}} \tag{5.3}$$

$$\ln({\mu'_{\text{composite}}}^2 + {\mu''_{\text{composite}}}^2) = f \ln({\mu'_{\text{NiZn}}}^2 + {\mu'_{\text{NiZn}}}^2) \tag{5.4}$$

Figure 5.3 (a)-(h) shows approximate linear relationships between $\ln\varepsilon'_{\text{composite}}$ and the % vol. These results are consistent with the Lichtenecker plots in the previous chapter (Chapter 4) for unsieved MnZn ferrite-PTFE composites. Figure 5.4 (a)-(h) also shows approximate linear relationships between $\ln({\mu'_{\text{composite}}}^2 + {\mu''_{\text{composite}}}^2)$ and the % vol., however, a saturation at 70% volume of NiZn ferrite is observed indicating that, for NiZn ferrite-PTFE composites, the Lichtenecker mixing formula is not valid for loadings above 50%.

By extrapolating a line of best fit to 100% vol. of filler, an estimate of the real permeability of the pure ferrite can be determined. The 100% vol. NiZn ferrite condition is when the ferrite particles are in full contact, without the presence of air gaps or PTFE. This is different to the sintered NiZn ferrite as the oxide boundaries that surround each of the ferrite particles are not present in the sintered product but would be present in our 100 % ferrite "composite". By extrapolating a line of best fit to 100% vol. NiZn ferrite composite from the Lichtenecker plots, the real permeability of a 100% vol. NiZn ferrite composite was found to be approximately 15 (for a particle size range of 45-53 μm at 20 MHz) which is far smaller than the permeability of the sintered NiZn ferrite (that has a permeability of 125 at DC).

5.4.3 Deducing the gradients of the Lichtenecker plots

The gradient from each of the Lichtenecker plots for the natural logarithm of the square of the modulus of the permeability (Figure 5.4 (a)-(h)) can be reduced onto a single plot of gradient as a function of average particle size for the fixed frequency of

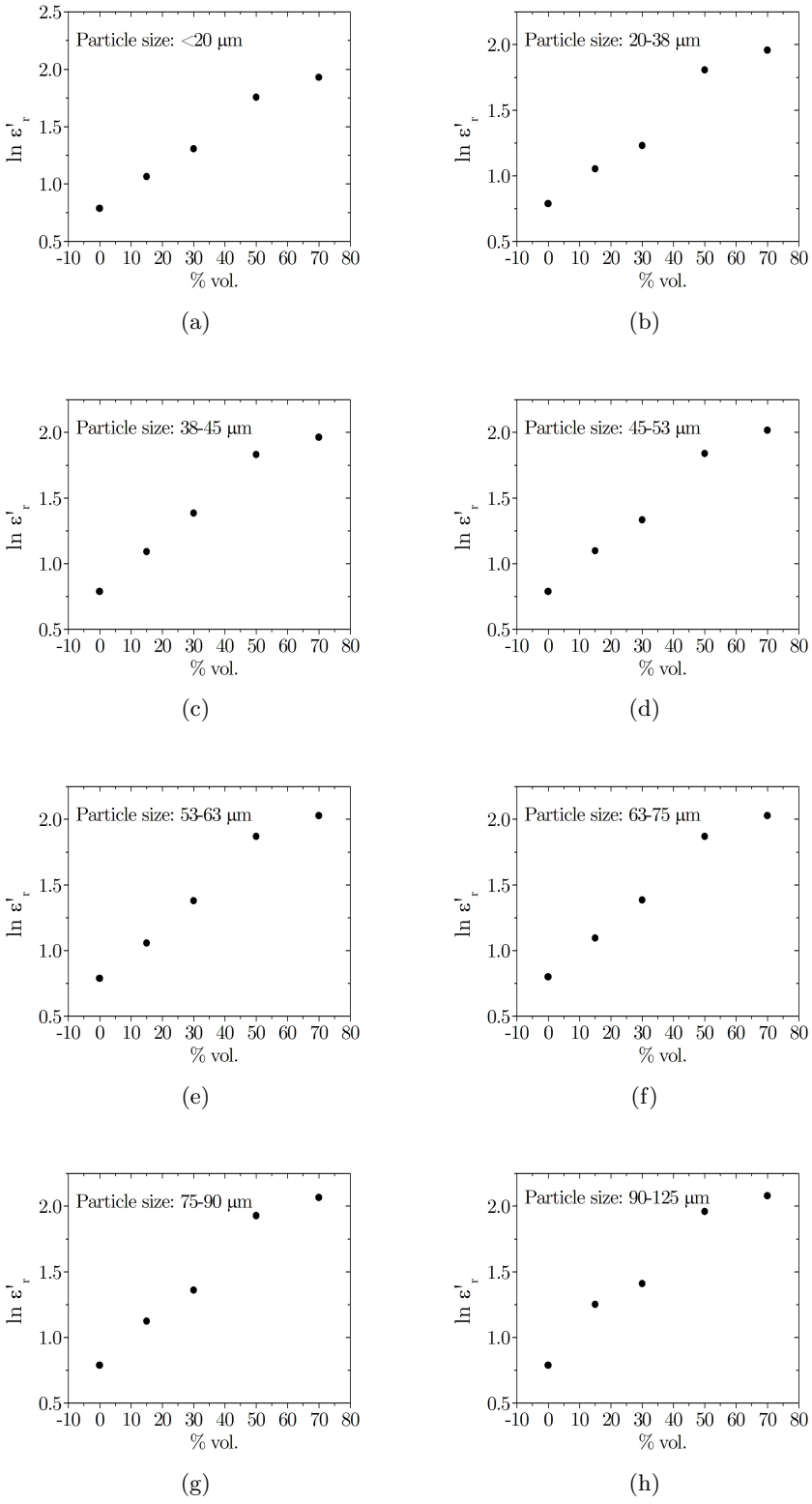

Figure 5.3: Plot of the square of the real permittivity as a function of the % vol. of NiZn ferrite in a PTFE matrix for the following particle size ranges; (a) less than 20 µm, (b) 20 - 38 µm, (c) 38 - 45 µm, (d) 45 - 53 µm, (e) 53 - 63 µm, (f) 63 - 75 µm, (g) 75 - 90 µmand (h) 90 - 125 µmtaken 20 MHz.

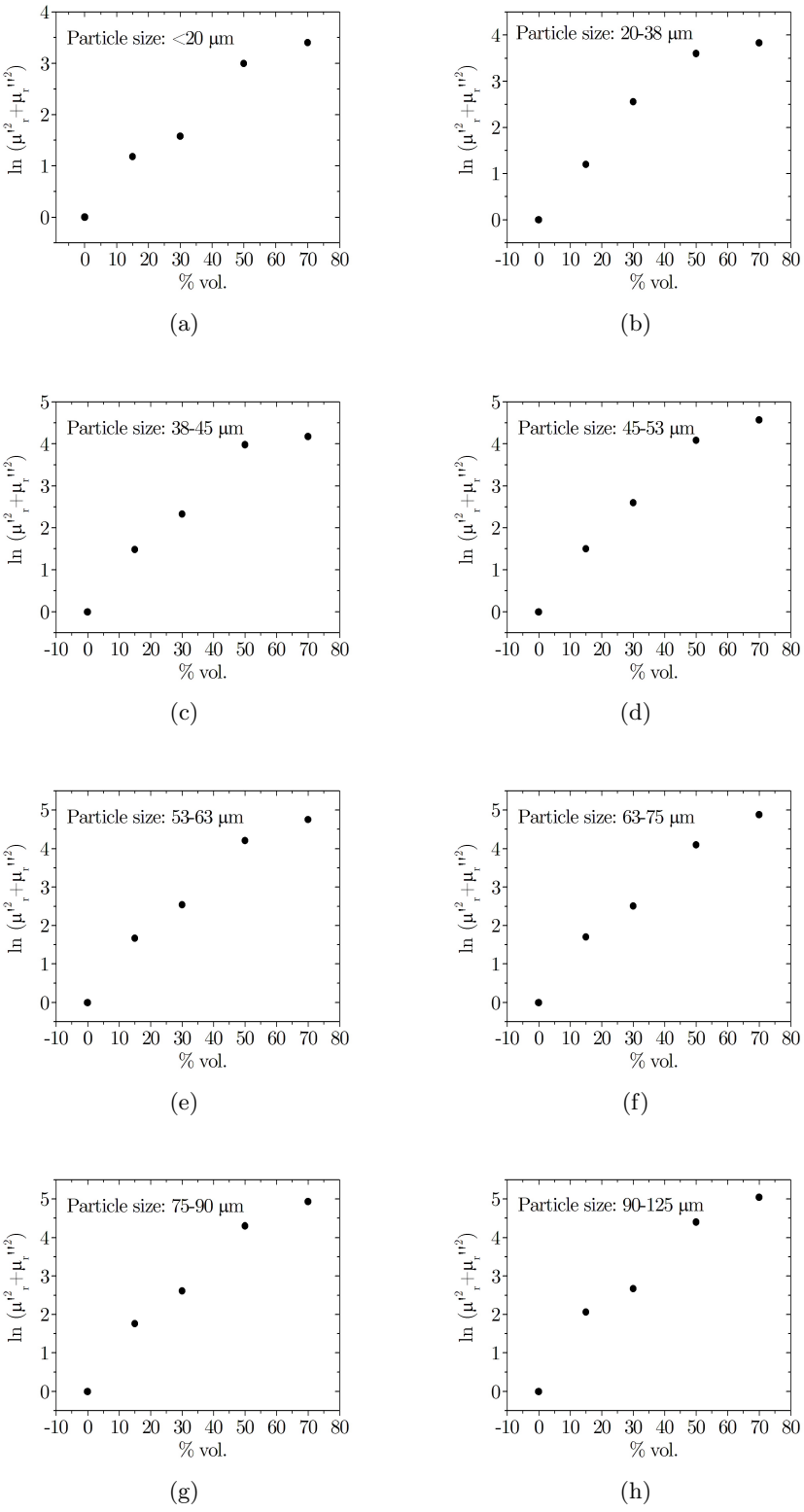

Figure 5.4: Plot of the natural logarithm of the square of the modulus of the complex permeability as a function of the % vol. of NiZn ferrite in a PTFE matrix for the following particle size ranges; (a) less than 20 μm, (b) 20 - 38 μm, (c) 38 - 45 μm, (d) 45 - 53 μm, (e) 53 - 63 μm, (f) 63 - 75 μm, (g) 75 - 90 μm and (h) 90 - 125 μm taken at 20 MHz.

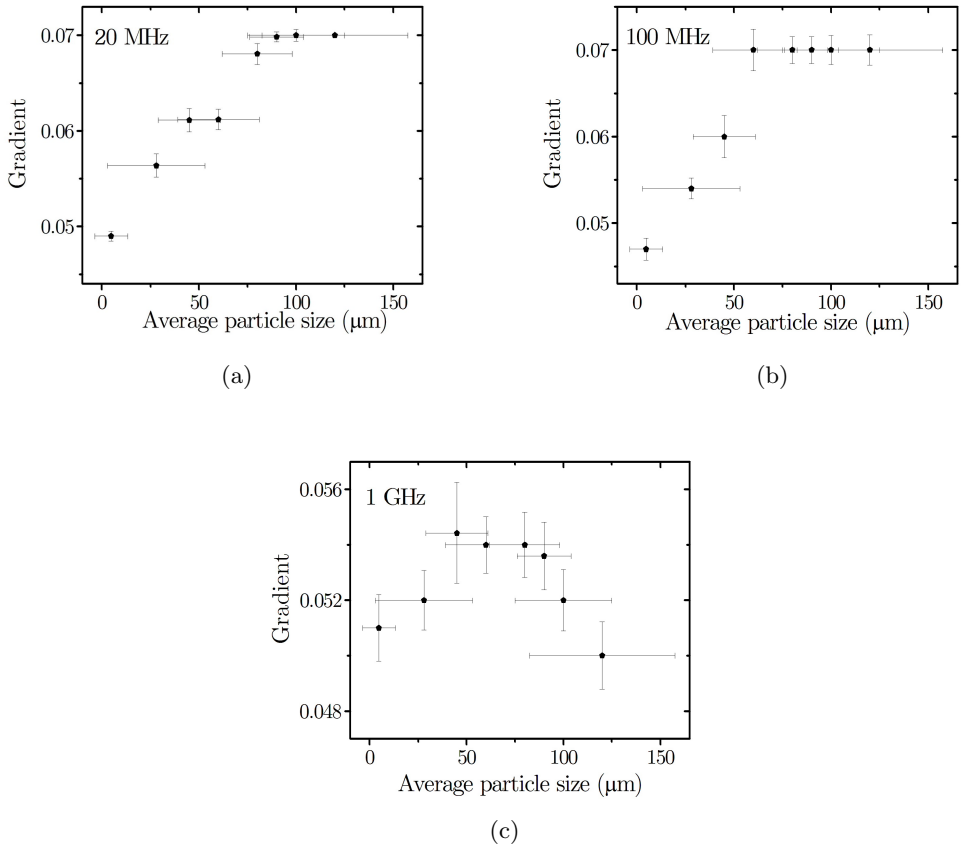

Figure 5.5: Plot of the gradient of the Licktenecker plots that are obtained by deducing the gradients from Figure 5.4(a)-(h) (plots showing the natural logarithm of the square of the modulus of the permeability as a function of % vol.) as a function of the average particle size taken at (a) 20 MHz, (b) 100 MHz and (c) 1 GHz.

20 MHz. Equivalent plots can be obtained from deducing the gradient of Lichtenecker plots for permeability taken at 100 MHz and 1 GHz, which are shown in Figure 5.5. Figure 5.5(a) (at 20 MHz) shows an increase in the gradient with increasing average particle size up to 75 μm, however, above 70 μm a saturation occurs in the gradient. In Figure 5.5(b), (at 100 MHz), the gradient saturates at a lower average particle size equal to approximately 60 μm. Increasing the frequency to 1 GHz (shown in Figure 5.5(c)) decreases the average particle size at which saturation of the gradient occurs to approximately 45 μm, the gradient also decreases as a function of the average particle size above 50 μm. The reason for a saturation of the gradient in these Lichtenecker plots is due to composites containing larger sized particles possessing a larger real permeability in comparison to smaller sized particles. The higher the permeability,

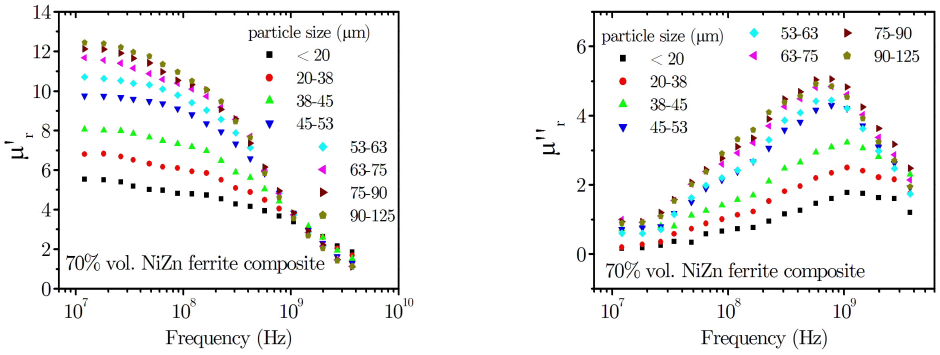

Figure 5.6: Plots of the complex permeability as a function of frequency for eight 70% NiZn ferrite-PTFE composites containing different particle size ranges: (a) shows the relative real permeability while (b) shows the relative imaginary permeability.

the lower cut off frequency at which the real permeability falls to unity, which is a consequence of Snoek's Law [6]. Note that although our data has been fitted to the Lichtenecker mixing formula, this formula does not take into account the size of the inclusions, just the % vol. of the filler, and assumes that the inclusions are much smaller than the wavelength of the incident EM radiation.

Figure 5.6 shows the complex permeability as a function of frequency for eight 70% NiZn ferrite-PTFE composites containing different particle size ranges, with (a) showing the relative real permeability and (b) showing the relative imaginary permeability. This plot shows that the change in the frequency dispersion of the complex permeability for composites containing different particle sizes follows Snoek's Law in a similar manner to the frequency dispersion of the complex permeability for composites containing different volume fractions of ferrite filler.

5.4.4 Three Part Composites

In the following section, three part composites containing MnZn ferrite, NiZn ferrite and PTFE are fabricated with a view to creating an impedance matched bulk material. Figure 5.7(a) shows the frequency dependent complex permittivity and permeability spectrum for a composite containing 65% vol. NiZn ferrite, 15% vol. MnZn ferrite and 20% vol. PTFE. The real permittivity and permeability are matched between 10 MHz and 50 MHz and the refractive index of this composite within that frequency range is 16.1. Figure 5.7(b) shows the reflected intensity, transmitted intensity, absorption and impedance as a function of frequency. In the impedance-matched frequency range (10 - 50 MHz), the transmitted intensity is 0.99 while the reflected intensity is 3.70 x 10^{-6} and

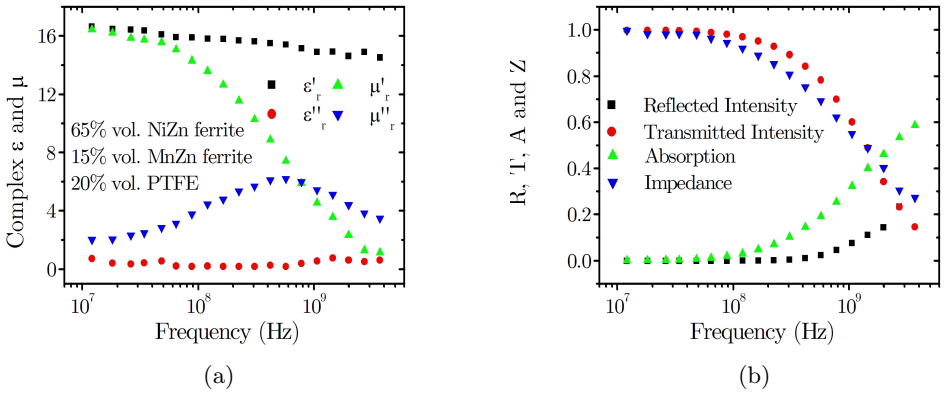

Figure 5.7: (a) Plot of the complex permeability and permittivity as a function of frequency and (b) reflected and transmitted intensity, absorption and impedance as a function of frequency for a 65% NiZn ferrite, 15% MnZn ferrite and 20% PTFE composite.

the absorption increases from 4.81 x 10^{-4} (at 1 MHz) to 0.61 (4 GHz) due to the onset of the domain wall resonance [8]. The relative impedance falls from 1.01 (at 1 MHz) to 0.28 at (at 4 GHz) due to the increasing mismatch of the complex permittivity and permeability with increasing frequency. The use of a third component has allowed for an otherwise non-impedance matched composite to be tuned, allowing for the complex permittivity and permeability to be set equal thus creating an impedance matched composite. By varying the proportion of each of the three components, impedance matching can be achieved for a variety of refractive indices of the composite. The proportions of each component were chosen in this specific study to provide the highest possible refractive index of the composite, using the assumption that samples can be fabricated with a % vol filler up to 80% vol..

5.5 Conclusions

This chapter has studied the effect of ferrite particle size on the electromagnetic properties of ferrite-PTFE composites. Both the permittivity and permeability were found to increase with increasing particle size. The real permittivity increased from 7.0 (for an average particle size of 4.2 μm) to 7.9 (for an average particle size of 147 μm) while the corresponding permeability increased from 5.5 to 12.5 for the same average particle sizes (for a 70% NiZn ferrite-PTFE composite at 20 MHz). It was found that all four volume fractions of NiZn ferrite (15% vol., 30% vol., 50% vol. and 70% vol) showed a similar trend for both the permittivity and permeability to

increase as a function of increased particle size. It was also noted that the permittivity and permeability were equal with a value of 6.1 when the average particle size was approximately 35 μm (for the 50% vol. composite) and equal with a value of 6.9 for an average particle size of approximately 20 μm (for the 70% vol. composite) at 20 MHz. These results demonstrate that impedance matching can be achieved for a variety of different refractive index values by controlling both the volume fraction of ferrite and particle size of NiZn ferrite.

The Lichtenecker mixing formula was utilised to plot the natural logarithm of the square of the modulus of the permeabiltiy and the natural logarithm of the real permittivity as a function of % vol. for each particle size range. Linear dependencies were obtained for these relations up to 50 % vol. of ferrite, above which a saturation occured. The gradient of each of the Lichtenecker plots for permeability was deduced at 20 MHz, 100 MHz and 1 GHz. A saturation in the gradient was observed 100 MHz and 1 GHz as the permeability of larger particles is greater than for smaller particles (for a fixed volume fraction of ferrite) resulting in larger particles possessing a lower cut-off frequency.

Lastly, three part composites were studied as a route to impedance matching ferrite composites via the addition of a third phase as opposed to controlling the ferrite particle size. It was found that an impedance matched material composed of 65% NiZn ferrite, 15% MnZn ferrite and 20% PTFE provided the highest refractive index of 16.1. from 10 MHz to 50 MHz.

The ability to alter the permeability and permittivity by controlling the particle size in magnetic composites, and by introducing a third component allows for desired EM properties e.g. impedance matching to free space to be engineered, which would not be possible by simply controlling the % vol. of a two part composite alone. By being able to manipulate the permeability as well as the permittivity, designs requiring high refractive index materials e.g. flat lenses (that traditionally rely on an all dielectric approach) may benefit from an added degree of freedom.

Chapter 6

Broadband impedance-matched electromagnetic metamaterial in the MHz range

6.1 Introduction

In this chapter, a high refractive index metamaterial is designed and fabricated that exhibits broadband impedance matching to free-space. The metamaterial is comprised of an anisotropic array of MnZn-ferrite cubes separated by dielectric spacers, which allows for the permittivity and permeability to be controlled independently. Such control enables the impedance matched condition to be met when both the permittivity and permeability are equal to each other. The refractive index of the metamaterial is 9.5, while the reflection is less than 1% and transmission is over 90% up to 70 MHz for normally incident radiation when one of the orthogonal linear polarisations lies in a symmetry plane of the array. A simple analytical theory is used to predict the effective permittivity and permeability dependence of the array of slabs and columns, which consist of alternating dielectric or alternating magnetic materials. The analytical theory has been compared to numerical modelling results using finite element method (FEM) modelling. The results presented in this chapter provide a route to the design of metamaterials with bespoke electromagnetic parameters for antenna miniaturisation and transformation electromagnetics.

6.2 Background

Impedance matching occurs when electromagnetic radiation at normal incidence travelling from free space strikes a substrate and is completely transmitted (and refracted) if the complex relative permittivity and permeability of the substrate are equal. To achieve this, one requires:

$$\frac{\mu_1}{\varepsilon_1} = \frac{\mu_2}{\varepsilon_2} \tag{6.1}$$

to ensure no reflection for normally incidence radiation, and

$$\sqrt{\varepsilon_1 \mu_1} \neq \sqrt{\varepsilon_2 \mu_2} \tag{6.2}$$

for refraction of the beam. In these equations, $\mu_j = \mu'_{\mathrm{j}} + i\mu''_{\mathrm{j}}$ and $\varepsilon_{\mathrm{j}} = \varepsilon'_{\mathrm{j}} + i\varepsilon''_{\mathrm{j}}$ are the relative complex permeability and permittivity respectively, where the subscript j identifies the media either side of the interface. In practice, such impedance matching conditions are difficult to achieve since they require electromagnetic material properties that are not widely found in nature. Such electromagnetic material properties requires the development and utilisation of bulk materials with equal and identically dispersive complex permittivity and permeability. While many naturally occurring materials have high permittivity values, there are far fewer with similarly high permeability values which might match the permittivities. It is the focus of this chapter to design, construct and characterise a broadband high-index material that is impedance-matched to air.

Ferrites, discussed and electromagnetically characterised in the previous two chapters, have been used extensively at microwave frequencies due to their high and reasonably non-dispersive permeability. Hence they are used in many applications, such as telecommunications and antenna systems [2]. Many ferrites also simultaneously have a non-dispersive and a high permittivity in the MHz and low GHz ranges since they are comprised of semiconducting grains encapsulated by insulating oxide barriers [137] that lead to charge separation and high polarisability of the grains. However, in order to equate μ and ε some material or chemical modification has conventionally been required. Thakur [138] has demonstrated broadband impedance matching using nano-sized ferrite particles sintered into a solid sample. Although μ' and ε' cannot be controlled independently, impedance matching between 100 and 500 MHz, with a refractive index of 4.8 is achieved. Kong et al. [11] showed that it is possible to independently control the real permeability of a 50% vol. $Ni_{0.95x}Zn_xCo_{0.05}Mn_{0.02}$ ferrite epoxy composite by varying the proportion of zinc in the ferrite, with impedance matching (at a refractive index of 6.5) achieved up to 30 MHz. More recently, impedance matching has been achieved by controlling the sintering temperature of a NiCuZn ferrite. Su et

al. [12] found that by utilising a 2 stage sintering process, equality of μ' and ε' at a value of 11.8 for 10 to 100 MHz was achieved. However, as well as this method being expensive and time consuming, the sintering process altered both μ' and ε' simultaneously, and hence independent control of these parameters was not possible. Zhang et al. [139] controlled μ' and ε' of BaCoTi substituted hexagonal ferrite by controlling the sintering temperature to between 900 and 950 °C. Although μ' and ε' were matched at a value of 24 over the frequency range 10 - 200 MHz, the method does not allow for the extra degree of freedom that our metamaterial structure provides as the permittivity and permeability can't be controlled independently.

Impedance matching does not necessarily require the use of ferrimagnetic materials. It can also be realised resonantly via artificial magnetism in specific metamaterial designs e.g. split ring resonators [140] or by implementing transmission line networks [141]. Impedance matching via transmission line networks uses a transmission line to allow power transfer from a source to a load. Such matched circuits are composed of 'matching networks' that link source to the transmission line and link the transmission line to the load so that no power is lost. Impedance matching can also be achieved using metamaterials that are artificially engineered composites with structured metallic inclusions that undergo resonance, and permit tailored values of μ and ε to be achieved. Landy et al. [142] provide an example of a resonant impedance-matched metamaterial. They employ a configuration of two metallic resonators comprising of two MM resonators that couple separately to electric and magnetic fields, where impedance matching is achieved by tuning both the resonant frequencies of the permeability and permittivity from the two separate elements. Although this metamaterial is impedance matched at a high frequency (11 GHz), it is a resonant effect, and therefore narrowband.

Kim et al. [143] have designed an ultra-thin ($\lambda/25$) antireflection coating by employing a pair of dispersive metamaterial layers on the face of a slab of Teflon. The dispersive metamaterial layer consists of a double layer of positive permittivity and negative permittivity metamaterials and comes from an approximation for a graded permittivity profile when the thickness of the material is very then. This technique is based on an analytical solution to a fundamental problem first studied by Rayleigh in 1879 [144], who considered the reduced reflection from a graded index layer.

The approach considered in this chapter is to incorporate a sub-wavelength structure into a bulk ferrite composite to create a metamaterial with a high refractive index, impedance matched over a broad band. This concept is similar to that considered by Matsumoto and Miyata in 1997 in order to reduce reflections from a resonant absorber [145] by reducing the effective permittivity, without greatly perturbing its permeability and magnetic loss. The approach of Matsumoto and Miyata involved the incorporation of experimental electromagnetic parameters from a ferrite composite into a numerical

model. This model was comprised of an infinite array (in the propagation direction) of alternating slabs of ferrite composite material and a low permittivity dielectric. The researchers obtained $\mu_{\text{eff}} = 3$ and $\varepsilon_{\text{eff}} = 10$ at 3 GHz for the array of slabs when the relative permittivity of the unstructured material was set to be 200 at the same frequency. This structuring did not make ε_{eff} and μ_{eff} equal, however the performance of the absorber was improved from 25% minimum reflection (at 300 MHz) when unlayered to 0.1% minimum reflection (at 3 GHz) when layered. Although it was not discussed in their work, the effective relative permittivity, ε_{eff} for their material (for an electric field normal to the slab plane) can be described by equation 6.3, which is derived in full later on in this chapter.

$$\frac{1}{\varepsilon_{\text{eff}}} = \frac{1}{\varepsilon_{\text{f}}} + \frac{\delta_z}{d_z}\left(\frac{1}{\varepsilon_{\text{s}}} - \frac{1}{\varepsilon_{\text{f}}}\right) \tag{6.3}$$

Here ε_{s} is the relative real permittivity of spacer material, ε_{f} is the relative real permittivity of the ferrite composite, d_z is the combined thickness of both slabs in the electric field direction and δ_z is the thickness of the low permittivity spacer only. It is clear that if $\varepsilon_{\text{f}} \gg \varepsilon_{\text{s}}$ small changes in δ_z will greatly alter ε_{eff}. The effective relative permeability, μ_{eff} dependence on these gap sizes takes a very different form. Here, the magnetic induction of the radiation lies in the plane of the slabs and is described by:

$$\mu_{\text{eff}} = \mu_{\text{f}} + \frac{\delta_z}{d_z}(\mu_{\text{s}} - \mu_{\text{f}}) \tag{6.4}$$

Here μ_{s} is the relative real permeability of the spacer material and μ_{s} is the relative real permeability of the composite. While equation 6.3 yields a strong dependence of the permittivity on the slab thickness, equation 6.4 Equivalent electrical circuits can be used to describe both Equations 6.3 and 6.4, which are shown in Figures 6.1(a) and (b). Both circuits represent an infinite stack of alternating spacer material with electromagnetic properties ε_{s} and μ_{s} and ferrite composite with electromagnetic properties ε_{f} and μ_{f}. C_s and C_f correspond to the capacitances of the spacer and ferrite composite while L_s and L_f are their inductances.

The structuring of these materials provides a degree of independent control (for one polarisation) of the relative permittivities and permeabilites by varying the thickness of one of the two materials.

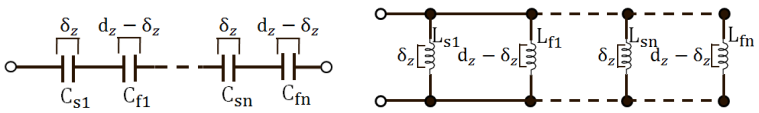

(a) (b)

Figure 6.1: Equivalent electrical circuits for structured ferrite composite with (a) capacitors representing the permittivity, and (b) inductors representing the permeability.

6.3 Method

6.3.1 Designing the metamaterial

In the following section, the concept of structuring bulk ferrite by producing arrays of slabs is extended to produce arrays of ferrite cubes that are anisotropically spaced in three orthogonal directions. This study focuses on varying the cube spacing in the electric field direction, with the spacings in the direction of the propagation vector and magnetic induction vector fixed to achieve impedance matching. For the alternate case of the propagation vector and electric field vector lying in the plane of the layers, μ_{eff} and ε_{eff} now obey the following dependency on δ_z:

$$\frac{1}{\mu_{\text{eff}}} = \frac{1}{\mu_{\text{f}}} + \frac{\delta_z}{d_z}\left(\frac{1}{\mu_{\text{s}}} - \frac{1}{\mu_{\text{f}}}\right) \tag{6.5}$$

$$\varepsilon_{\text{eff}} = \varepsilon_{\text{f}} + \frac{\delta_z}{d_z}(\varepsilon_{\text{s}} - \varepsilon_{\text{f}}) \tag{6.6}$$

Notice, that compared to equations 6.3 and 6.4, the dependencies of μ_{eff} and ε_{eff} on δ_z reverse roles when the orthogonal polarisation is incident. This simple slab model and exact analytical solution is derived in full later on in this chapter as well as being applied to a more complicated system consisting of anisotropic arrays of columns (assuming that the thickness of any dielectric spacers in directions perpendicular to δ_z are small compared to the column sizes and δ_z).

6.3.2 Fabrication of the metamaterial

The metamaterial is comprised of a commercially available sintered Manganese Zinc ferrite ($Mn_{0.8}Zn_{0.2}Fe_2O_4$) powder supplied by MagDev Ltd (UK) compressed at Exeter into a composite with standard PTFE powder (of uniform particle size 3 μm) chosen as the matrix material. The MnZn ferrite and PTFE powders were mixed together with a ferrite volume of 70% and pressed into samples using a steel mould at 55 MPa for 300

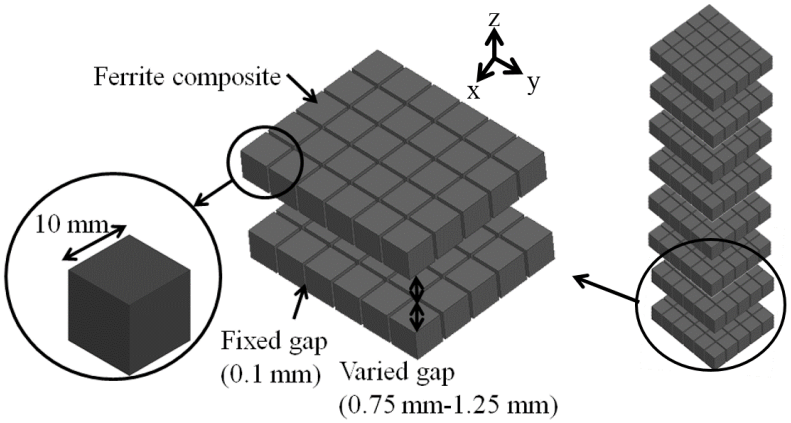

Figure 6.2: Anisotropic array of cubes comprised of ferrite composite material. The cubes are spaced in the x and y-directions by 0.1 mm thick adhesive tape ($\delta_x = \delta_y = 0.1$ mm), while the arrays are spaced in the z-direction from the ground plane and signal line in the stripline using polyester film ($\delta_z = 0.75$ mm to 1.25 mm).

s as described in Chapter 3 to produce $1 \times 1 \times 1$ cm cubic ferrite-composite elements [146]. Each cube in the x- and y- directions is spaced by double sided polyester adhesive tape of thickness 0.1 mm. Two 6×5 layers of cubes are shown in Figure 6.2.

6.3.3 Electromagnetic characterisation

Each of these planar arrays of cubes are positioned in a calibrated stripline (described in Chapter 3) to fill the void between the central signal line and one of the two symmetrically positioned ground planes. The impedance of this signal line is controlled by its width and is chosen to maintain 50 Ohms in an unloaded stripline. The stripline set up is optimised with a ground-plane-signal-line gap equal to the height of the cubes plus the spacer material. To ensure an infinite array (in the x- direction) is mimicked accurately, the metamaterial slabs, which are 5 cubes long, extend much further than the extent of the signal line in the y- direction, and hence its response will be indistinguishable from an infinite sample. The two ground planes above and below the cube arrays also replicate the response of an infinitely repeat period (z-direction) metamaterial slab. The S-parameters of the sample in the stripline are recorded as a function of frequency, with the Nicholson-Ross-Weir (NRW) extraction method [67], [68] once again used to deduce the effective complex permittivity and permeability. This was repeated for metamaterial designs with polyester inter-layer spacings varied between $\delta_z = 1.5$ mm and $\delta_z = 2.5$ mm, with the EM properties recorded for each spacing and hence the impedance matching condition was sought.

In Figure 6.2, the two slabs of ferrite cubes are shown as well as an array of many

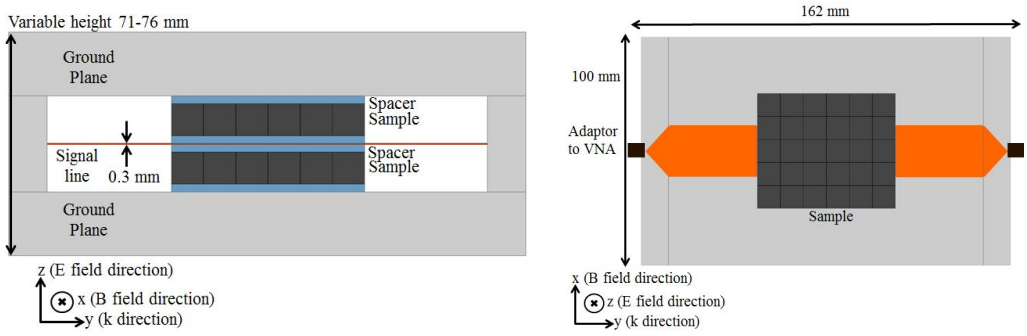

Figure 6.3: Schematic of the stripline set-up containing the array of ferrite cubes and Teflon spacers from (a) side on view and (b) a top down cross section. The stripline is connected to a Vector Network Analyser (VNA).

slabs. The two slab array of ferrite cubes is the exact sample geometry for the experimental sample, however, due to the stripline mirror planes an infinite stack of ferrite cubes is mimicked and also shown in Figure 6.2. For clarity, Figure 6.3 is included to show the ferrite cube arrays in the stripline. Here, the Teflon spacer thickness (in the z-direction) is varied between 1.5 mm and 2.5 mm, and denoted δ_z. The stripline ground planes are the mirror planes and thus an infinite stack of slabs is mimicked.

6.4 Experimental Results

6.4.1 Electromagnetic properties of bulk ferrite composite

In order to numerically model the EM response of this metamaterial to determine the effective permittivity and permeability, the frequency dependent complex permittivity and permeability of the bulk ferrite composite material must first be deduced. In our study we chose to use the 70% loaded composite because it was the highest loading of ferrite that could be made into cubic samples that were not too brittle. It can be seen in Figure 6.4 that the values of μ' and ε' remain approximately constant across the frequency range 10 MHz to 100 MHz while μ'' and ε'' remain relatively small from 10 MHz to 100 MHz. The high and non-dispersive permeability and permittivity of this ferrite composite up to 100 MHz makes it an excellent bulk material from which to fabricate a high refractive index and impedance matched structure. The origin of the high μ' of this ferrite material at low frequencies arises from the domain wall motion [8] and is described in full in Chapter 2. Although the resonant frequency associated with these phenomena occurs at frequencies above 100 MHz (approximately 300 MHz), the

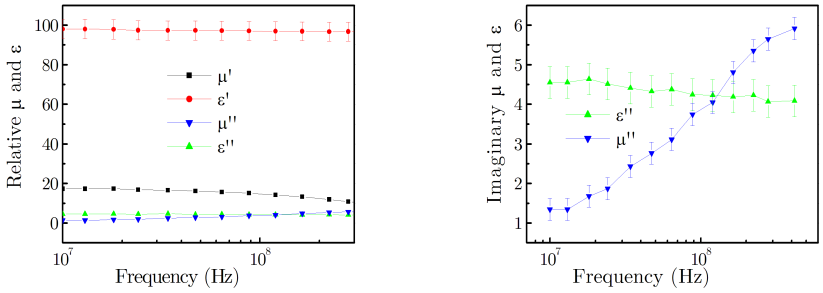

(a) (b)

Figure 6.4: (a) Frequency dispersion of the complex relative permeability and permittivity of the 70% vol. ferrite and 30% vol. PTFE composite, and (b) shows the frequency dispersion of the imaginary relative permeability and permittivity of the 70% vol. ferrite and 30% vol. PTFE composite.

resonance is broad, and there is an increase in μ'' at much lower frequencies. Importantly, up until 100 MHz, both μ' and ε' remain large and frequency independent. The high relative real permittivity is due to the semi-conducting ferrite grains encapsulated by dielectric layers. At low frequencies, electron hopping occurs between Fe^{3+} and Fe^{2+} on the octahedral sites [137]. The electrons reach the phase boundaries between the ferrite and PTFE through hopping, and thus accumulate at these boundaries, resulting in interfacial polarisation). A full discussion of the frequency dispersion of the permittivity can be found in Chapter 2.

6.4.2 Deducing the impedance matched condition experimentally

As mentioned earlier, for the impedance match condition to be found for the metamaterial, the spacing between the layers, δ_z, was varied between 0.75 and 1.25 mm. In order to deduce the number of meta-atoms (cubes) that are required to mimic the EM response of an infinite sample in the $\underline{k}$ direction, finite element method (FEM) numerical modelling [147] was used. It was found that a minimum of 6 cubes long in the $\underline{k}$ direction was required to mimic the infinite sample and the addition of more cubes did not change the extracted effective material parameters to 1 decimal place. This is presented in Figure 6.5 which shows the effective permittivity and permeability, as well as the refractive index as a function of number of cubes in the propagation direction ($\underline{k}$).

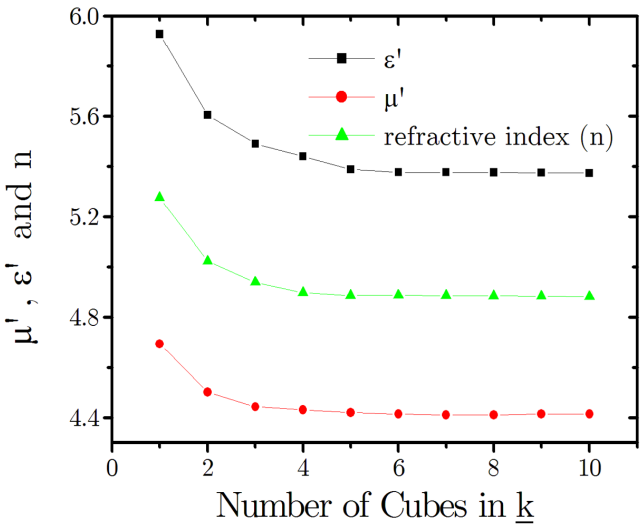

Figure 6.5: Modelling data showing the effective permittivity and permeability, and the refractive index (n) as a function of the number of cubes in the propagation direction (k).

6.4.3 Frequency dependent electromagnetic properties of the metamaterial

The predictions of the effective permittivity and permeability of the metamaterial from FEM modelling, which use the frequency dependent experimental material parameters of the bulk ferrite composite (from Figure 6.4), along with the experimental results, are both shown in Figure 6.6 . It should be noted that the comparison of experiment with simulation is good considering the sensitivity to δ_z in the experiment, especially for small values of δ_z . It should be noted that in the experiment, small variations in alignment of the cube array or spacer thickness will impact the $\varepsilon'_{\text{eff}}$ value of the metamaterial and would lead to differences between the experimental value of $\varepsilon'_{\text{eff}}$ and that extracted from the model. To achieve impedance matching, the imaginary parts of the permittivity and permeability must also be matched. Although Figure 6.6 shows the real parts of the permittivity and permeability only, the imaginary permittivity and permeability are both near zero and approximately equal at low frequencies. However, as the frequency increases, the imaginary permeability increases due to the relaxation of the domain wall motion (the trend of the real permeability to decrease with increased frequency is described by Snoek's law [6] which is discussed in full in Chapter 2). The metamaterial is therefore no longer impedance matched for these higher frequencies (above 70 MHz).

Equations 6.3 and 6.4 used to describe the permittivity and permeability depen-

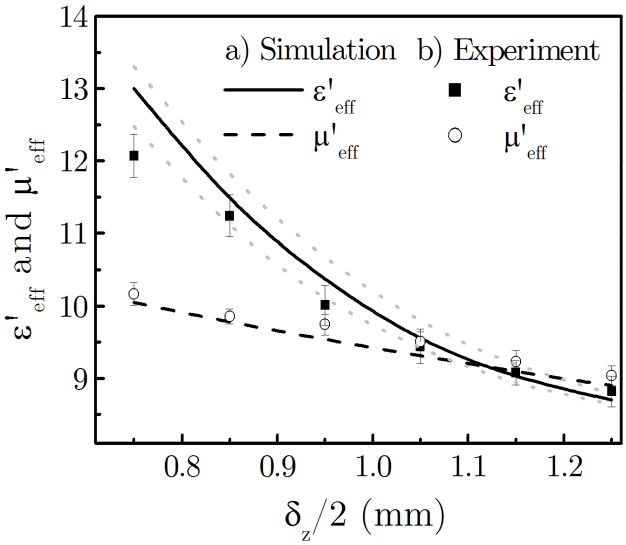

Figure 6.6: Effect of varying the separation between the layers δ_z 2 on the effective relative real permittivity($\varepsilon'_{\text{eff}}$) and permeability ($\mu'_{\text{eff}}$) for the anisotropic array of ferrite cubes at 50 MHz: (a) Predictions from FEM modelling with the uncertainty based on the range of ε' values for the ferrite composite indicated by dotted lines, and (b) averaged experimental results and standard deviation.

dence of a stack of alternating dielectric/magnetic material can be used to predict the strong dependence of $\varepsilon'_{\text{eff}}$ and relatively weak linear dependence of μ'_{eff} on δ_z giving independent control of ε' and μ' which is observed. The experimental results suggest that the metamaterial will have $\varepsilon'_{\text{eff}} = \mu'_{\text{eff}}$ when $\delta_z/2 = 1.15$ mm. (Note, the average ε'_r for the ferrite composite is 98 ± 5 (see Figure 6.4) hence $\varepsilon'_{\text{eff}}$ has an uncertainty associated with it, indicated by the dotted lines in Figure 6.6.)

Figure 6.7 shows the extracted value of μ'_{eff} and ε_{eff} for the anisotropic impedance matched, cube array ($\delta_z = 1.15$ mm) when the electric field is in the z-direction. Predictions from the FEM model (line) and the experimental data (points) are shown. From Figure 6.7 it can been seen that μ'_{eff} and $\varepsilon'_{\text{eff}}$ for the experiment are equal to within 4% across the frequency range 10 to 300 MHz and μ''_{eff} and $\varepsilon''_{\text{eff}}$ remain small but are dispersive beyond 70 MHz. Above 70 MHz, an increase in μ''_{eff} is accompanied by an associated decrease in μ'_{eff}, due to the domain wall relaxation. As μ'_{eff} and $\varepsilon'_{\text{eff}}$ are equal at a value of 9.5, the refractive index is also 9.5 from 10 to 300 MHz. The combination of this matched impedance and refractive index allows for the radiation to travel through the material without reflection while simultaneously slowing down the radiation by a factor of 9.5.

Figure 6.8 shows the experimentally measured reflected (black line) and transmitted (red line) intensity from the ferrite cube array metamaterial as a function of frequency.

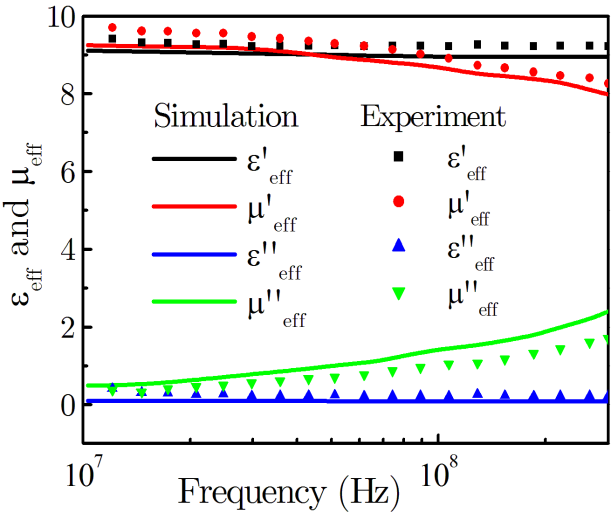

Figure 6.7: FEM modelling (line) (using the frequency dependent permittivty and permeability values from the stripline measurements for the bulk composite) and experimental results (points) of the complex relative permeability and permittivity as a function of frequency for the impedance matched anisotropic array of ferrite cubes. The cube spacings are 0.1 mm in both the x- and y-directions, and 1.05 mm in the z-direction (parallel to the incident electric field vector).

It is clear from this plot that the transmission remains above 95%, whilst the reflection remains at less than 0.3% for frequencies up to 70 MHz. Again, due to lossses arising from the permeability as the domain wall relaxation sets in the transmission intensity falls significantly above about 70 MHz. However, although the metamaterial is no longer impedance matched at higher frequencies, the absorbing properties of this metamaterial are very good at these higher frequencies. From Figure 6.8 it can be seen that 60.5 mm, the length of the metamaterial in the propagation direction (6 cubes long), maintains a reflection coefficient of less than 0.3% up to 300 MHz, despite becoming highly absorbing. Although the absorption for 6 layers at 200 MHz is 33% (see Figure 6.9(a)), it was also found using simulations that 22 layers of this metamaterial (200 mm) in the propagation direction is the required thickness to absorb 97% of the radiation at 200 MHz (corresponding wavelength 1.5 m) making it an excellent absorber at frequencies above 70 MHz.

6.4.4 Polarisation dependence

As previously discussed, the ferrite cube array is anisotropic and hence is dependent on the polarisation of the incident radiation. Figure 6.9 presents numerical modelling

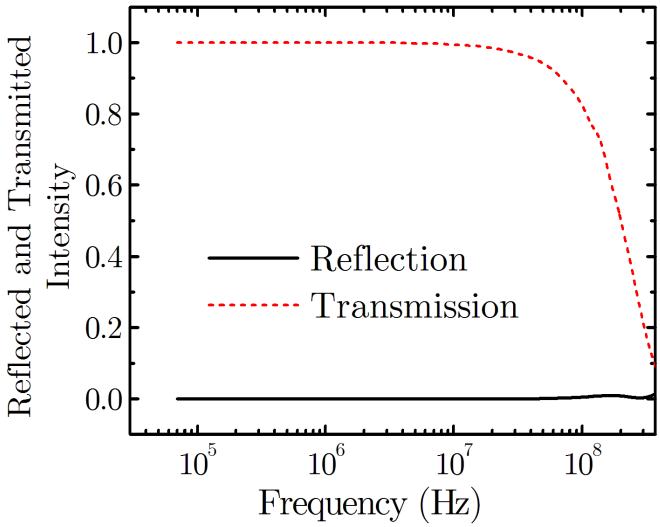

Figure 6.8: Experimentally determined reflected and transmitted spectra from the ferrite cubes metamaterial (6 cubes long) with the incident electric field vector parallel to the z-axis.

results for the reflected and transmitted intensity as well as the absorption of the ferrite cube array for two orthogonal polarisations of the electric field vector. While Figure 6.9(a) shows near 100% absorption for the array at 200 MHz when the array is 20 elements in length, Figure 6.9(b) shows a greatly reduced absorption of 65% because the metamaterial is no longer impedance matched and is now highly reflective. Polarisation dependent metamaterials are of interest for the creation of broadband, polarisation sensitive absorbers, and polarisation detectors [148–153].

6.5 An analytical theory for structured composite materials

Chapter 4 uses a simple analytical formula to describe the permittivity dependence on air gaps between a ferrite sample and the stripline. Earlier in this chapter, four equations (6.3, 6.4, 6.5 and 6.6) describing the permittivity/permeability dependence of an array of slabs on the relative thickness of each of the slabs were introduced. Here, a full description of the slab model (see Figure 6.10) will be given followed by an analytical description of a similar system where the slabs have been divided into columns (see Figure 6.15). In the latter case, the slabs are cut into infinitely tall columns, thus giving gaps in two orthogonal directions. Both analytic descriptions are used to predict the effective permittivity and permeability dependence of metamaterials with inhomo-

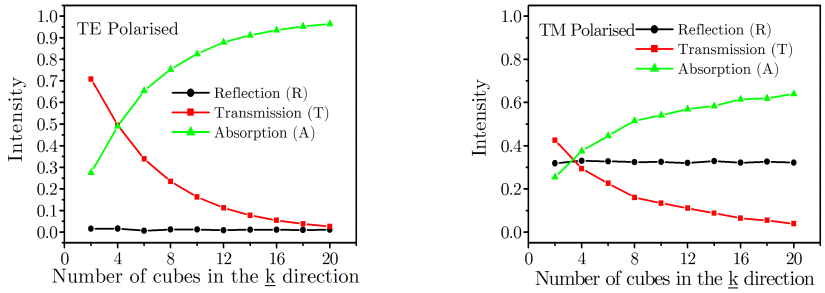

Figure 6.9: Numerical modelling results for reflected intensity (R), transmitted intensity (T) and absorption (A) as a function of the sample thickness in the propagation direction ($\underline{k}$) taken at 200 MHz. (a) for transverse electric field polarisation and (b) for transverse magnetic field polarisation.

geneous EM properties such as the anisotropic array of ferrite cubes discussed earlier in this chapter. It should be noted that an exact analytical description of the cube arrays is not possible due to the conflicting boundary conditions imposed on an array with alternating permittivity/permeability material in the three orthogonal directions. These conditions will be discussed in the following subsections.

6.5.1 The slab model for alternating dielectric layers

In the following subsection, equation 6.3 will be derived, followed by a similar derivation to deduce equation 6.6. In particular, equation 6.3 is important for understanding the effective permittivity response for the ferrite cube array, as well as for understanding the implication of air gaps in the stripline, which is discussed in Chapter 4. Equation 6.6 is also derived as it mirrors the permeability response in the ferrite cube array.

Let us start by considering the system shown in Figure 6.10(a) which shows two slabs of differing permittivity values (ε_1) and (ε_2), where the electric field is applied perpendicular to the slabs (in the z- direction). It can be assumed that $\underline{D}_z$ is continuous for this geometry and therefore, in the z- direction;

$$\underline{D} = \varepsilon_1 \underline{E}_1 = \varepsilon_2 \underline{E}_2 \tag{6.7}$$

where ε_1 and ε_2 are the relative real permittivity values of materials 1 and 2 and $\underline{E}_1$ and $\underline{E}_2$ are the electric field vectors in materials 1 and 2, and $\underline{D}$ is the displacement

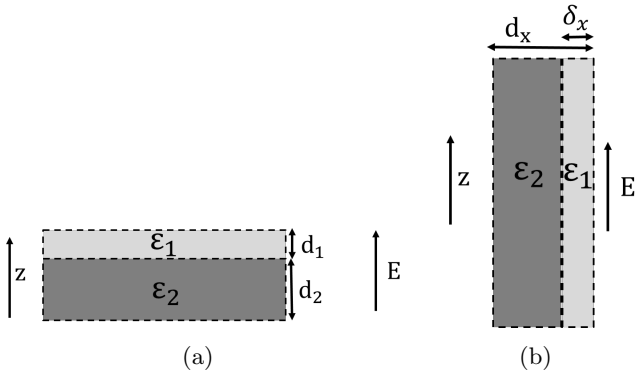

Figure 6.10: Diagram of the slab model consisting of layers of alternating permittivity material. In (a), the slabs of alternating permittivity material are perpendicular to the applied electric filed while in (b), these slabs are parallel to the applied electric field. In (a), the slabs are assumed to be finite in length in the electric field direction however in (b) the slabs are assumed to be infinite in length in the electric field direction.

vector. Similarly;

$$\underline{\mathrm{D}}_{\mathrm{eff}} = \varepsilon_{\mathrm{eff}}\underline{\mathrm{E}}_{\mathrm{eff}} \tag{6.8}$$

where $\varepsilon_{\mathrm{eff}}$ is the effective permittivity of the total array, $\underline{\mathrm{D}}_{\mathrm{eff}}$ and $\underline{\mathrm{E}}_{\mathrm{eff}}$ are the effective displacement vector and effective electric field vector of the total array. By re-writing $\underline{\mathrm{E}}_{\mathrm{eff}}$ in terms of $\underline{\mathrm{E}}_1$, $\underline{\mathrm{E}}_1$, d_1 and d_2 and using the relation $\underline{\mathrm{E}}= \frac{\underline{\mathrm{D}}}{\varepsilon}$; equation 6.9 is obtained;

$$\underline{\mathrm{E}}_{\mathrm{eff}} = \underline{\mathrm{D}}_{\mathrm{eff}}\left(\frac{d_1/\varepsilon_1 + d_2/\varepsilon_2}{d_1 + d_2}\right) = \frac{\underline{\mathrm{D}}_{\mathrm{eff}}}{\varepsilon_{\mathrm{eff}}} \tag{6.9}$$

Lastly, $\underline{\mathrm{D}}_{\mathrm{eff}}$ and $\underline{\mathrm{E}}_{\mathrm{eff}}$ are removed by substituting in $\varepsilon_{\mathrm{eff}}$ and by using the relation between d_1, d_2 and d_z ($d_1 + d_2 = d_z$) and by assuming $d_1 = \delta_z$ then equation 6.10 is obtained;

$$\frac{1}{\varepsilon_{\mathrm{eff}}} = \frac{1}{\varepsilon_2} + \frac{\delta_z}{d_z}\left(\frac{1}{\varepsilon_1} - \frac{1}{\varepsilon_2}\right) \tag{6.10}$$

Equation 6.10 demonstrates the strong dependence of $\varepsilon_{\mathrm{eff}}$ on δ_z. Figure 6.11 shows the dependence of the effective permittivity ($\varepsilon_{\mathrm{eff}}$) as a function of the gap in the electric field direction (δ_z). This figure shows both the analytical solutions (red points) to equation 6.10 assuming $\varepsilon_1 = 1$ and $\varepsilon_2 = 30$ and the FEM numerical modelling solutions (black points). Both methods for deducing $\varepsilon_{\mathrm{eff}}$ provide values that are in good agreement with each other.

The array of slabs likewise, can be modelled in the case where the slabs are parallel to

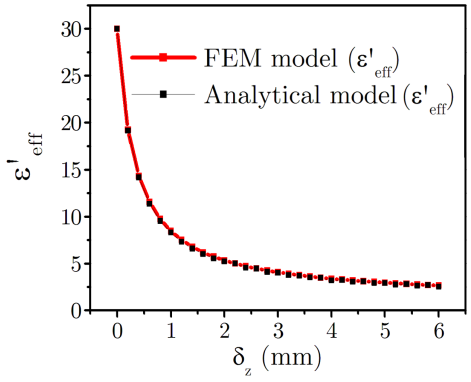

Figure 6.11: Effective permittivity (ε_{eff}) as a function of the gap in the electric field direction (δ_z) for an array of slabs of alternating dielectric material

the applied electric field as shown in Figure 6.10 (b) with the electric field now oriented parallel to the slabs of alternating dielectric material. In this case, the tangential electric field is now conserved, therefore the three following relations can be stated;

$$\underline{\mathrm{D}}_1 = \varepsilon_1 \underline{\mathrm{E}}_1 \tag{6.11}$$

$$\underline{\mathrm{D}}_2 = \varepsilon_2 \underline{\mathrm{E}}_2 \tag{6.12}$$

$$\underline{\mathrm{D}}_{\text{eff}} = \varepsilon_{\text{eff}} \underline{\mathrm{E}}_{\text{eff}} \tag{6.13}$$

As $\underline{\mathrm{D}}_{\text{eff}}$ is an average of $\underline{\mathrm{D}}_1$ and $\underline{\mathrm{D}}_2$, it can be written in terms of $\underline{\mathrm{D}}_1$ and $\underline{\mathrm{D}}_2$ and their relative thicknesses (d_x and δ_x);

$$\underline{\mathrm{D}}_{\text{eff}} = \frac{\underline{\mathrm{D}}_1 \delta_x + \underline{\mathrm{D}}_2 (d_x + \delta_x)}{d_x} \tag{6.14}$$

The electric displacement vectors ($\underline{\mathrm{D}}_{1,2,\text{eff}}$) can now be substituted for the electric field vectors ($\underline{\mathrm{E}}_{1,2,\text{eff}}$) and the relative real permittivity ($\varepsilon_{1,2,\text{eff}}$) due to the relations stated in equations 6.11, 6.12 and 6.13. Secondly, if $\underline{\mathrm{E}}_1$, $\underline{\mathrm{E}}_2$ and $\underline{\mathrm{E}}_{\text{eff}}$ are eliminated the following equation is obtained;

$$\varepsilon_{\text{eff}} = \frac{\delta_x}{d_x}(\varepsilon_1 - \varepsilon_2) + \varepsilon_2 \tag{6.15}$$

Equation 6.15 demonstrates an averaging of the effective permittivity (ε_{eff}) when the electric field is applied parallel to the array of slabs and reveals a linear dependence between ε_{eff} and δ_x.

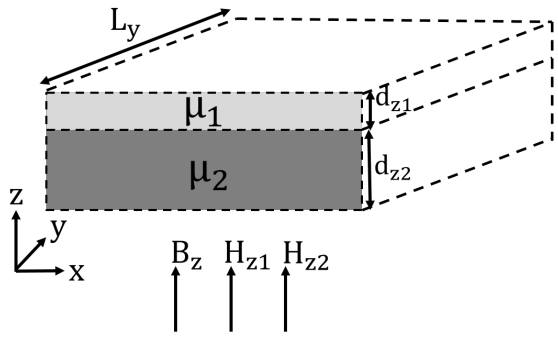

Figure 6.12: Diagram of the slab model consisting of layers of alternating permeability material, with the slabs are orientated perpendicular to the externally applied magnetic field. The slabs are assumed to be finite in length in the magnetic field direction.

6.5.2 The slab model for alternating magnetic layers

In the following subsection, an analytic formula will be derived for the effective permeability (μ_{eff}) as a function of slab thickness (δ_z) for an array of slabs of alternating magnetic material when the applied magnetic field is applied both perpendicular and parallel to the array of slabs.

To begin, the system shown in Figure 6.12 is considered which shows an array of slabs of alternating magnetic materials, with the magnetic field applied perpendicular to the slabs. In the following system, the external magnetic field ($\underline{\mathrm{B}}_x$) remains constant while the magnetic induction ($\underline{\mathrm{H}}$) is different in each of the two different materials, yielding the following relations;

$$\underline{\mathrm{H}}_{z1} = \frac{\underline{\mathrm{B}}_z}{\mu_1} \tag{6.16}$$

and

$$\underline{\mathrm{H}}_{z2} = \frac{\underline{\mathrm{B}}_z}{\mu_2} \tag{6.17}$$

Here, d_1 and d_2 are the thickness of each of the slabs of permeability μ_1 and μ_2. The next step is to find the average magnetic induction;

$$\underline{\mathrm{H}}_z = \frac{\underline{\mathrm{H}}_{z1} d_1 + \underline{\mathrm{H}}_{z2} d_2}{d_1 + d_2} \tag{6.18}$$

Now, assuming as before that $d_1 + d_2 = d_z$ and $d_1 = \delta_z$ then;

$$\underline{\mathrm{H}}_z = \frac{\underline{\mathrm{H}}_{z1} \delta_z + \underline{\mathrm{H}}_{z2} (d_z - \delta_z)}{d_z} \tag{6.19}$$

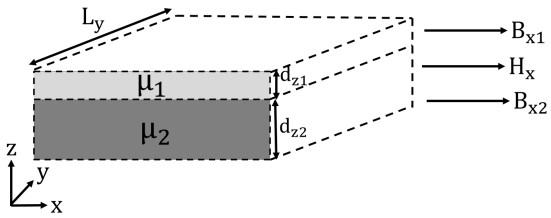

Figure 6.13: Diagram of the slab model consisting of layers of alternating permeability material, with the slabs orientated parallel to the applied magnetic field.

We also know that the average $\underline{\mathrm{H}}_z$ can be written in terms of $\underline{\mathrm{B}}_z$, μ_1 and μ_2 using Equations 6.16 and 6.17;

$$\underline{\mathrm{H}}_z = \frac{\underline{\mathrm{B}}_z}{\mu_1}\frac{\delta z}{d_z} + \frac{\underline{\mathrm{B}}_z}{\mu_2} - \frac{\underline{\mathrm{B}}_z}{\mu_2}\frac{\delta_z}{d_z} = \frac{\underline{\mathrm{B}}_z}{\mu_{\mathrm{eff}}} \tag{6.20}$$

Lastly, by dividing through by $\underline{\mathrm{B}}_z$, we yield the final relation;

$$\frac{1}{\mu_{\mathrm{eff}}} = \frac{1}{\mu_1}\frac{\delta_z}{d_z} - \frac{1}{\mu_2}\frac{\delta_z}{d_z} + \frac{1}{\mu_2} \tag{6.21}$$

$$\frac{1}{\mu_{\mathrm{eff}}} = \frac{1}{\mu_2} + (\frac{1}{\mu_1} - \frac{1}{\mu_2})\frac{\delta_z}{d_z} \tag{6.22}$$

Equation 6.22 demonstrates the strong dependence of μ_{eff} on δ_z and describes the same dependence as Equation 6.14.

Next, we turn our attention to the case where the array of slabs of alternating permeability material are aligned parallel to applied magnetic field, this arrangement is shown in Figure 6.13.

In the case shown in Figure 6.13, the magnetic induction is conserved and thus we state the following;

$$\underline{\mathrm{B}}_{x1} = \mu_1 \underline{\mathrm{H}}_x \tag{6.23}$$

and

$$\underline{\mathrm{B}}_{x2} = \mu_2 \underline{\mathrm{H}}_x \tag{6.24}$$

Where μ_1 and μ_2 are the permeabilities for each of the slabs. The next step is to calculate the total magnetic flux (ϕ_B) or ($\underline{\mathrm{B}}_x$);

$$\phi_B = (\underline{\mathrm{B}}_{x1} d_1 + \underline{\mathrm{B}}_{x2} d_2) L_y = \underline{\mathrm{B}}_T \tag{6.25}$$

Once again, we can say that $d_1 + d_2 = d_z$ and $d_1 = \delta_z$, hence Equation 6.25 becomes;

$$\underline{\mathrm{B}}_T = (\underline{\mathrm{B}}_{x1}\delta_z + \underline{\mathrm{B}}_{x2}(d_z - \delta_z))L_y \tag{6.26}$$

Equally, we can say that the total magnetic induction that passes through an area ($\underline{\mathrm{H}}_T$);

$$\underline{\mathrm{H}}_T = \underline{\mathrm{H}} \times d_z \times L_y \tag{6.27}$$

Now we know the total magnetic flux, we can deduce the effective permeability μ_{eff} using Equation 6.29;

$$\mu_{\text{eff}} = \frac{\underline{\mathrm{B}}_T}{\underline{\mathrm{H}}_T} \tag{6.28}$$

$$\mu_{\text{eff}} = \frac{\mu_1 \underline{\mathrm{H}}_x \delta_z + \mu_2 \underline{\mathrm{H}}_x (d_z - \delta_z) L_y}{\underline{\mathrm{H}}_x d_z L_y} \tag{6.29}$$

Equation 6.29 can be simplified by dividing through by $\underline{\mathrm{H}}_x$ and L_y to produce a familiar equation previously deduced for a similar system of alternating permittivity materials (Equation 6.15);

$$\mu_{\text{eff}} = \mu_2 + (\mu_1 - \mu_2)\frac{\delta_z}{d_z} \tag{6.30}$$

Equation 6.30 shows a linear dependence between the effective permeability (μ_{eff}) and the thickness of the slabs (δ_z) which is markedly different from the inverse relationship found between these two quantities in Equation 6.22. The slab model has been modelled numerically with the slabs orientated perpendicular to the applied electric field and parallel to the applied magnetic field with this equivalent system being described by Equations 6.10 and 6.30. The solutions to these two equations (assuming $\mu_1 = 1$, $\mu_2 = 15$, $\varepsilon_1 = 1$ and $\varepsilon_2 = 30$) are compared to FEM numerical modelling results, which is shown in Figure 6.14. As expected, a linear dependence between μ_{eff} and δ_z is obtained, while an inverse relationship is found between ε_{eff} and δ_z.

6.5.3 The column model for alternating dielectric materials

The slab model can be extended by cutting the slabs to produce an array of columns as shown in Figure 6.15 where the electric field is parallel to the array of columns. This geometry is a closer representation to the ferrite cube array as there are now two orthogonal directions that can be varied independently of each other. The relation between the area of the columns (perpendicular to the applied electric field) and the

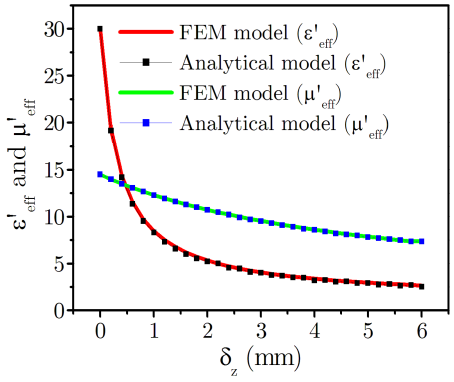

Figure 6.14: The effective permittivity and permeability as a function of the gap size (δ_z) for an array of slabs with the electric field applied perpendicular to the slabs and the magnetic field applied parallel to the slabs. Both numerical modelling and analytical data is shown.

effective permittivity can be deduced in a similar manner to the previously derived slab model.

Now;

$$\underline{\mathrm{D}}_1 = \varepsilon_1 \underline{\mathrm{E}}_1 \tag{6.31}$$

$$\underline{\mathrm{D}}_2 = \varepsilon_2 \underline{\mathrm{E}}_2 \tag{6.32}$$

As the effective electric displacement vector ($\underline{\mathrm{D}}_{\mathrm{eff}}$) is an average of the electric displacement vectors associated with each material, it can be written as the following;

$$\underline{\mathrm{D}}_{\mathrm{eff}} = \underline{\mathrm{D}}_1 \left(\frac{\delta_x \delta_y}{d_x d_y} \right) + \underline{\mathrm{D}}_2 \left(\frac{(d_x - \delta_x) - (d_y - \delta_y)}{d_x d_y} \right) \tag{6.33}$$

Or simply as;

$$\underline{\mathrm{D}}_{\mathrm{eff}} = \varepsilon_{\mathrm{eff}} \underline{\mathrm{E}}_1 \tag{6.34}$$

This can be re-expressed as;

$$\varepsilon_{\mathrm{eff}} \underline{\mathrm{E}}_1 = \varepsilon_1 \underline{\mathrm{E}}_1 \left(\frac{\delta_x \delta_y}{d_x d_y} \right) + \varepsilon_2 \underline{\mathrm{E}}_2 \left(\frac{(d_x - \delta_x) - (d_y - \delta_y)}{d_x d_y} \right) \tag{6.35}$$

Finally, in order to write an equation for the effective permittivity ($\varepsilon_{\mathrm{eff}}$) in terms of each material's permittivity value (ε_1 and ε_2) and their relative areas ($\frac{\delta_x \delta_y}{d_x d_y}$) and ($\frac{(d_x - \delta_x) - (d_y - \delta_y)}{d_x d_y}$), the electric field vectors ($\underline{\mathrm{E}}_{\mathrm{eff},1,2}$) must be removed. This results in

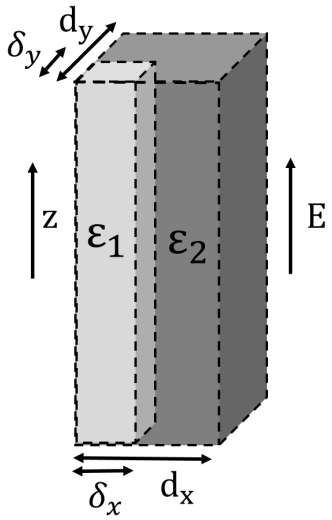

Figure 6.15: Schematic of the column model consisting of blocks of alternating permittivity material with the columns assumed infinite in the electric field direction.

the following relation;

$$\varepsilon_{\text{eff}} = \varepsilon_2 + (\varepsilon_1 - \varepsilon_2)\left(\frac{\delta_x \delta_y}{d_x d_y}\right) \tag{6.36}$$

Equation 6.36 is equivalent to equation 6.15 in the case of arrays of slabs parallel to the applied electric field and results once again in a linear dependency between the effective permittivity (ε_{eff}) and the area of each of the two columns. This array of columns was once again modelled numerically using FEM modelling with the values obtained for (ε_{eff}) compared to the analytically modelled solutions to produce Figure 6.16. Figure 6.16 shows the effective permittivity (ε_{eff}) as a function of the ratio of the area of material 1 of permittivity $\varepsilon_1 = 1$ to the total area (material 2 has a permittivity of $\varepsilon_2 = 30$).

6.5.4 The column model for alternating magnetic materials

The model for columns of alternating permittivity materials can be extended to the case where the columns consist of alternating magnetic materials (of alternating permeability values) as shown in Figure 6.17.

In Figure 6.17, the applied magnetic field direction is in the z- direction and the magnetic induction vector ($\underline{\mathrm{H}}_z$) is conserved, thus we can say:

$$\underline{\mathrm{B}}_{z1} = \mu_1 \underline{\mathrm{H}}_z \tag{6.37}$$

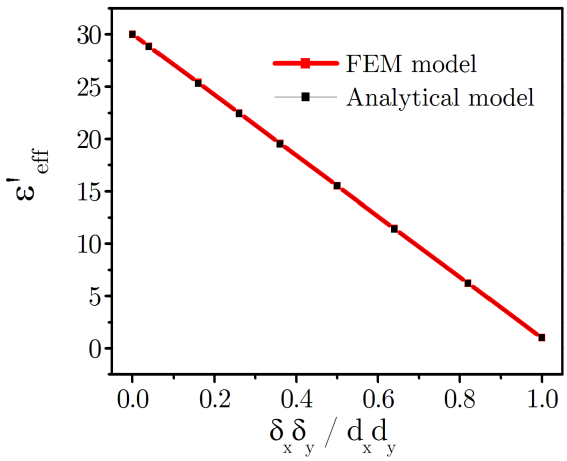

Figure 6.16: The effective permittivity of an array of columns as a function of the ratio of the area of material 1 with a permittivity of ε_1 to the area of material 2 with a permittivity of ε_2 and is denoted α. The applied electric field is applied parallel to the columns. Both FEM numerical modelling solutions and analytical solutions are shown.

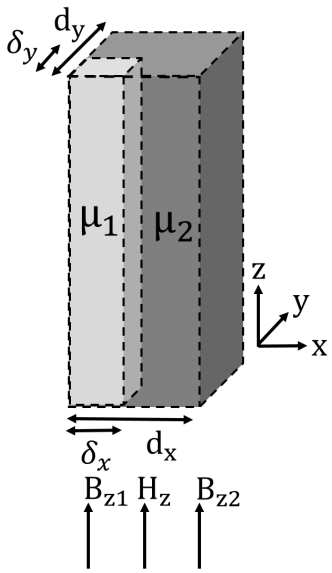

Figure 6.17: Schematic of the column model consisting of blocks of alternating permeability material with the columns assumed infinite in the magnetic field direction.

and

$$\underline{B}_{z2} = \mu_2 \underline{H}_z \tag{6.38}$$

The next step is to deduce the total magnetic flux ($\underline{B}_T$) passing through the columns;

$$\underline{B}_T = (\underline{B}_{z1}\delta_x\delta_y + \underline{B}_{z2}(d_x d_y - \delta_x\delta_y)) \tag{6.39}$$

To deduce the effective permeability (μ_{eff}), we utilise Equation 6.40 along with Equations 6.37 and 6.38;

$$\mu_{\text{eff}} = \frac{\underline{B}_T}{\underline{H}_T} \tag{6.40}$$

Hence;

$$\mu_{\text{eff}} = \frac{\mu_1 \underline{H}_z \delta_x\delta_y + \mu_2 \underline{H}_z (d_x d_y - \delta_x\delta_y)}{\underline{H}_z d_x d_y} \tag{6.41}$$

In order to produce a relation between the effective permeability (μ_{eff}) and the permitivities of each material (μ_1 and μ_2) and their relative areas, we must divide Equation 6.41 by $\underline{H}_z$. This produces Equation 6.42;

$$\mu_{\text{eff}} = \mu_1 \frac{\delta_x}{d_x}\frac{\delta_y}{d_y} + \mu_2 - \mu_2 \frac{\delta_x}{d_x}\frac{\delta_y}{d_y} \tag{6.42}$$

Equation 6.42 can be simplified further to produce an expression for μ_{eff} in a simple form;

$$\mu_{\text{eff}} = \mu_2 + (\mu_1 - \mu_2 \frac{\delta_x\delta_y}{d_x d_y}) \tag{6.43}$$

Equation 6.43 is comparable to Equation 6.36 for the permittivity case and demonstrates the linear dependence between the effective permeability on the area of the columns of alternating permeability material.

The six equations (Equations 6.14, 6.22, 6.24, 6.30, 6.36 and 6.43) derived in this section that describe the dependence of the effective permittivity or permeability on the physical dimensions of a structured composite material can be used to design anisotropic materials with bespoke EM properties.

6.6 Conclusions

In this chapter, a simple anisotropic array of ferrite cubes is used to demonstrate broadband impedance matching up to 70 MHz. This metamaterial had a refractive in-

dex of 9.5 while the reflection, for one specific linear polarisation, is less than 0.3% over the frequency band. The metamaterial design also provides potential for exploitation as an electromagnetic absorber of sub-wavelength thickness as 22 layers of this metamaterial (200 mm) in the propagation direction is the required thickness to absorb 97% of the radiation at 200 MHz (corresponding wavelength 1.5 m). The permittivity of the metamaterial was controlled by altering the spacings between the cube elements in the electric field direction. The dependence of the EM properties on spacings in these two orthogonal directions were derived analytically and compared to numerical modelling results. While there was an inverse relationship between the effective permittivity and the gap between cubes in the electric field direction, a linear dependence of the permeability on the gap between cubes in the electric field direction was found. Although simple, these equations which describe arrays of slabs and columns of alternating dielectric or magnetic materials are valuable for the creating materials with bespoke EM properties. These two simple models for arrays of slabs and columns cannot be extended to arrays of cubes because of the problem of conflicting boundary conditions i.e. both $\underline{E}$ parallel and $\underline{D}$ perpendicular must be conserved. Although arrays of ferrite slabs rather than cubes could have been used experimentally to produce the highest refractive index metamaterial possible, such a design would not provide independent control of $\varepsilon'_{\text{eff}}$ and μ'_{eff} simultaneously, whilst splitting the metamaterial into cubes provides control in three orthogonal directions. To increase the refractive index of this metamaterial further, a sintered ferrite could be used as the cube material however this would also decrease the impedance matching frequency range, similarly, a hexagonal ferrite composite would provide a reduced refractive index over a broader impedance matched frequency range. Further investigations may overcome the limits of Snoek's law [6] (discussed in full in Chapter 2) will likely yield a ferrite material with a higher resonant frequency, and the prospect of a broader impedance matched region.

Chapter 7

Controlling permittivity and diamagnetism using broadband, isotropic, low-loss metamaterials

7.1 Introduction

In this chapter, a metamaterial comprised of metallic cube-shaped elements (a design first proposed theoretically by Shin et al. [154] in 2009) is designed and fabricated to provide independent control of it's complex permittivity and permeability (ε and μ). This metamaterial is comprised of an isotropic array of hollow metallic cube-shaped elements with each face detached from it's nearest neighbours, but with opposite faces that are electrically connected through the center of the cube. The permeability can be simply tailored through appropriate patterning of the faces, thereby controlling the propagation of eddy currents around the cubic elements that determine the strength of the diamagnetic response. The permittivity is controlled by altering the spacing between the cubic elements, or varying the size of the faces. The arrays of cubic elements are electromagnetically characterised between 10 and 500 MHz using a stripline technique via two different parameter extraction methods, with the results for complex permittivity and permeability in good agreement with each other. The electromagnetic (EM) properties for the cubic metamaterials is investigated to observe the dependence of the frequency range over which the array is non-dispersive with the refractive index of the cube array.

The initial work by Shin et al. [154] has been extended by studying the electromagnetic properties of a simpler structure which is comprised of an array of 'dumbbell' shaped elements. This study uses numerical modelling to analyse the impact of

varying the geometric dimensions of the dumbbell elements on the electromagnetic response of the array when oriented perpendicular and parallel to the applied magnetic field. By understanding the contributions of the individual components that make up the cube structure, the cubic elements can be optimised to provided the desired electromagnetic response of the metamaterial. The ability to independently tune the effective permeability and permittivity in a metamaterial without relying on inherently narrow-band resonant behaviour is crucial for the development of broadband, microwave transformation-optics-based devices.

7.2 Background

The concept of metamaterials was introduced in Chapter 1. It describes metamaterials as artificial structures whose electromagnetic properties are dictated by geometry in addition to the composition of the material [24–26]. Metamaterials are typically comprised of arrays of sub-wavelength elements where the electromagnetic (EM) properties of the material are dictated by the interaction between individual elements with the incident electromagnetic radiation, this collective effective-medium response can yield bespoke values of complex relative permeability ($\mu = \mu' + i\mu''$) and complex relative permittivity ($\varepsilon = \varepsilon' + i\varepsilon''$). The development of metamaterials has led to new ways of creating exotic properties such as negative refractive index [24, 27], very high refractive index materials [28], and impedance-matched materials [155]. If these properties, specifically high refractive index materials, can be achieved in a non-resonant manner, and hence operate over a broad frequency range with low-losses, it makes their electromagnetic properties desirable for the creation of graded index devices [156]. Independent control of ε and μ is also very important when considering how to achieve high refractive index metamaterials. Consider an array of an array of sub-wavelength, metallic, cubic elements: ε' is relatively simple to control as it relies on the capacitive coupling between adjacent elements and the ε' of the material spacing the cubic elements. Such structures allow for values of $\varepsilon' \gg 1$ to be achieved [157], however, these cubic elements will produce a diamagnetic response ($\mu' \ll 1$) due to eddy currents that propagate around each cube. This severely limits the achievable refractive index ($n = \sqrt{\mu}\sqrt{\varepsilon}$) therefore metallic elements need to be designed which provide a far weaker diamagnetic response. Njoku *et al.* [158] previously investigated a non-resonant metamaterial consisting of perfectly electrically conducting cubes spaced by dielectric and experimentally verified that high values of $\varepsilon' = 47$ can be achieved. However, this study did not consider the large diamagnetic response of such a metamaterial which results in a low value of μ' and hence a greatly reduced refractive index. Lapine *et al.* [159] investigated non-resonant metamaterials theoretically, specifically tailoring

the diamagnetic response of a close packed hexagonal lattice of closed metallic loops. The aim was to produce a metamaterial with near zero values of μ'; a theoretical value of μ' of 0.05 was obtained. Belov *et al.* [160] further developed the idea of near-zero-permeability metamaterials by designing an isotropic metamaterial (as opposed to an anisotropic metamaterial designed by Lapine *et al.*) consisting of an array of metallic cubes which possessed a μ' of 0.15. Rather than producing a metamaterial with near zero values of μ', metamaterials with a greatly suppressed diamagnetic response were studied by Shin *et al.* [154], who aimed to produce a high refractive index metamaterial having a near-unity value of μ'. The metamaterial design by Shin *et al.* was a development on the design of Belov *et al.* since it is based on the concept of isotropic arrays of metallic cubic elements. The diamagnetic response of the array of metallic cubes in this particular theoretical study was significantly weakened by structuring the cube faces to reduce the area subtended by the eddy-current loops. This modification enhanced μ' towards 1, which allowed for the refractive index to be greatly increased. The modification process implemented by Shin *et al.* was split into two stages; their first metamaterial array was a simple cubic array of solid metallic cubes (a single cubic element is shown in Figure 7.1(a)) with $a = 10$ mm. Although the permittivity of the array is greatly enhanced with a value of approximately 20, μ' is approximately 0.1 from 10 to 500 MHz. To increase μ', the solid cubes were replaced with hollow cubes each having separated faces that were only electrically connected through the center of the cube by six conducting spokes (see Figure 7.1(b). This modification from the solid cube array to the array of hollow cubes with separated faces weakens the diamagnetic response and hence increases μ' from 0.1 to 0.57. The significant weakening of the diamagnetic response is due to the confining of the currents to the edge of two plates perpendicular to the applied magnetic field and to the faces of the four plates parallel to the applied magnetic field. This has been experimentally verified by Campbell *et al.* in 2013 [161].

In the second stage Shin *et al.* subdivided each face (see Figure 7.1(c)) to limit the area enclosed by surface currents, thereby decreasing the diamagnetic response and increasing μ' to a value of 0.97 whilst maintaining the large ε' value. In this study, it is verified experimentally and via numerical modelling, that subdividing the plates does indeed weaken the diamagnetic response as proposed by Shin *et al.*, as well as demonstrating that the EM properties can be independently controlled via appropriate structuring of the cubic elements. In this chapter three different metamaterial samples are studied, initially via numerical modelling, before fabricating and characterising their electromagnetic response over the frequency range from 10 MHz to 500 MHz. Schematics of the three individual elements of the three metamaterials studied are shown in Figure 7.1.

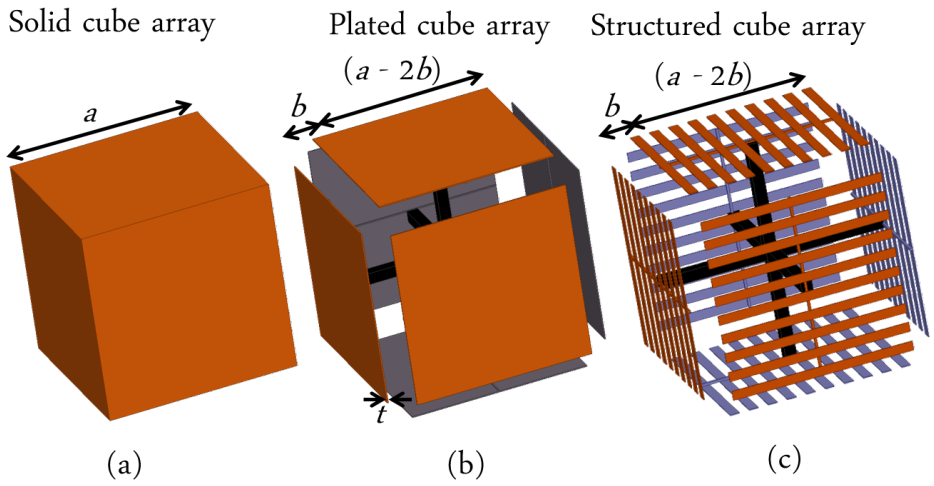

Figure 7.1: (a) A schematic of a solid copper cube metamaterial element with face areas of a^2. (b) A hollow copper cube metamaterial element with a face areas of $(a-2b)^2$. The faces of the cube are disconnected along the edges and joined together by a spoke that runs through the centre of the cube. The variable t denotes the plate thickness, which is 35 μm in both (b) and (c). (c) A progression from (b) where each face of the cube has now been subdivided to produce a comb like structured face. Once again, all six faces are electrically connected through the centre of the cube (Note that only 10 of the 20 rods on each face have been drawn for clarity).

For a plane-wave normally incident upon an array formed of solid metallic cubes, Figure 7.1(a), the propagation of eddy currents around the whole cube produces a strong diamagnetic response. However, in the case of Figure 7.1(b), the cubes are now hollow with faces that are disconnected along their edges which reduces the area enclosed by the induced currents by confining them to the individual faces (four faces parallel to the incident magnetic field direction and two faces perpendicular to the incident magnetic field). While the four plates parallel to the applied magnetic field provide a weak diamagnetic response, the two plates perpendicular to the applied magnetic field provide the largest contribution to the diamagnetic response since the induced current extends around the entire area of each plate with an area of $(a-2b)^2 = 64$ mm^2. The plate thickness also alters the diamagnetic properties of the two plates perpendicular to the applied magnetic field. In this case, increasing the plate thickness leads to the integral of the current density increasing, which strengthens the diamagnetic response. By contrast the four plates parallel to the applied magnetic field produce a far weaker effect since the current loops only extends around the narrow edge of the plates each presenting an area of $(a-2b)t = 0.56$ mm^2. Therefore, increasing the plate thickness t, increases the diamagnetic response induced in all 6 plates of the cube. When progress-

ing from the plated to structured cube array, the diamagnetic response is suppressed as rods further reduce the area of the current loops in the plates, which allows the magnetic field to penetrate deeper into the structure.

The permittivity of the metamaterial (ε') is dependent on the capacitive coupling between adjacent plate faces of neighbouring cubes i.e. the spacing between the plates (in the direction perpendicular to the incident electric field), the face size, and the permittivity of the spacer material between them. Practically, when switching the experiment from solid cubes to hollow cubes, the plate area must be reduced to maintain a constant pitch, this reduction in the area (100 mm^2 to 64 mm^2) reduces the capacitance between plates and hence the effective permittivity. In the case of progressing from cubes with solid plates, to cubes with structured plates, the permittivity is not greatly affected. Provided the rods are close enough together, the rods screen out the incident electric field (essentially acting like a wire grid polariser) and hence the dielectric response is close to that of a solid face.

7.3 Method

The fabrication technique used to construct the arrays of copper cubes can be found in Chapter 3. In this section, a more detailed description of the electromagnetic characterisation is presented. As previously discussed, the stripline technique is used to electromagnetically characterise cubic metamaterial samples by positioning two samples of the same design above and below the central conducting line in a calibrated stripline of a similar design to that of Barry [73]. The stripline was designed to have an impedance close to 50 Ohms by setting the height (as discussed in Chapter 3) and hence impedance-matched throughout the frequency range of interest (10 MHz to 4 GHz) with no sample present. The stripline and connecting coaxial cables are calibrated out before the metamaterial samples are characterised, therefore the impedance of the stripline is only 50 Ohms after calibration. The stripline was connected to a Vector Network Analyser (VNA) and the S-parameters (the complex reflection and transmission co-efficients) recorded. Since each cube array was much wider (width = 56.4 mm) than the signal line (width = 22 mm), and since the presence of the ground planes above and below the cube arrays mimic an infinitely repeating array of cubic elements in the electric field direction (z- direction), the measured S-parameters were equivalent to those that one would obtain from a sample of infinite extent in the y- and z- directions.

From the frequency-dependent values of the complex reflection- and complex transmission-amplitude coefficients, the effective permeability and permittivity of the metamaterials was determined in the frequency range 10 - 500 MHz. In previous chapters, the

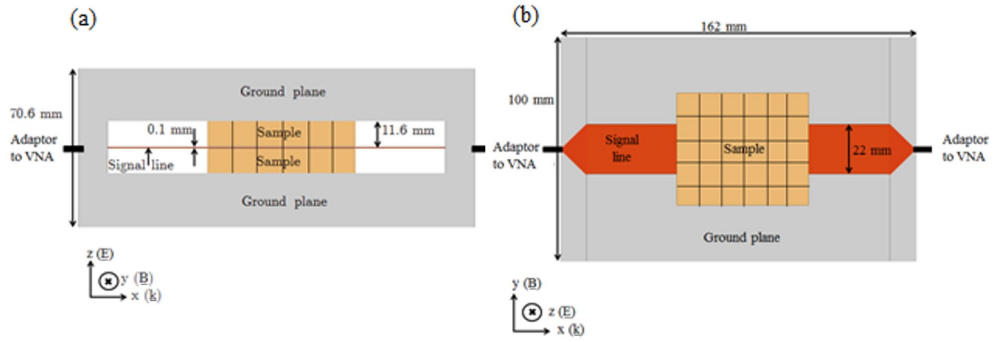

Figure 7.2: Schematic of the stripline set up containing the metamaterial sample: (a) side-on view, and (b) top-down view.

Nicholson-Ross-Weir (NRW) extraction method [67, 68] was used, however, in this study, a second method was utilised that simultaneously fits the real and imaginary parts of the S-parameters to the well-known three layer Fresnel equations for normal incidence reflection and transmission through a parallel-sided slab (see equations 7.1 and 7.2). Figure 7.3 shows a schematic of the reflection and transmission amplitude coefficients stated in equations 7.1 and 7.2 for the total reflection and transmission.

This fitting algorithm uses the sum of squares difference between the measured and calculated values as the objective function (implemented using the fmincon function in MATLAB [78]) and has been used as a comparison to the NRW method to verify that both methods are consistent and in agreement with each other.

$$r_{13} = r_{12} + \frac{t_{12}t_{21}r_{23}e^{2i\alpha}}{1 - r_{21}r_{23}e^{2i\alpha}} \tag{7.1}$$

$$t_{13} = \frac{t_{12}t_{23}r_{23}e^{2i\alpha}}{1 - r_{21}r_{23}e^{2i\alpha}} \tag{7.2}$$

Here t_{13}, t_{12}, t_{21} and t_{23} are the complex transmission amplitude coefficients, r_{13}, r_{12}, r_{21} and r_{23} are the complex reflection amplitude coefficients and $e^{2i\alpha}$ is the phase factor for three layers (A B A) where A is typically air and B is the dielectric layer (and in the case of this piece of work, the B later is the cubic metamaterial). A more generalised phase factor for multilayer interference is $e^{2ni\alpha}$ where n is the number of 'B' layers. This method is only valid when the material properties are non-dispersive over the frequency range for which all data points are simultaneously fitted to. This limits the frequency range over which this metamaterial can be electromagnetically characterised to between 10 and 500 MHz. It is noted that the same fitting routine has been successfully utilised previously by Campbell *et al.* [161] when investigating

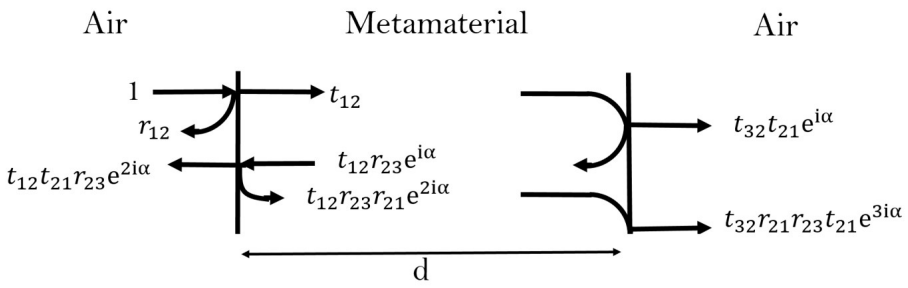

Figure 7.3: Schematic of the reflection and transmission amplitude coefficients for the three layer Fresnel model.

similar metamaterial structures.

7.4 Experimental Results

7.4.1 Transmitted and reflected intensity spectra for the three cubic metamaterials

To extract values of permeability and permittivity from the complex reflection- and transmission- amplitude coefficients for the copper cube arrays, both a fitting routine and the standard Nicholson-Ross-Weir (NRW) method are utilised. As the fitting routine assumes that the EM material being non-dispersive over a fitting window, this frequency range must first be deduced. This is done by plotting the reflected and transmitted intensities calculated from the S-parameters as a function of frequency for each of the 3 types of cubic metamaterial. In order to plot the reflected and transmitted intensities (R and T) as a function of frequency, the four measured reflection and transmission amplitude coefficents are squared and summed, i.e $r'^2 + r''^2 = \mathrm{R}$ and $t'^2 + t''^2 = \mathrm{T}$. The resulting plot should be composed of a series of peaks and minima that are equally spaced (known as Fabry-Perot modes) within the the frequency range that the permeability and permittivity are non-dispersive. However, the cubic metamaterials are dispersive at higher frequencies as can be observed in Figure 7.4 where the reflection minima (and corresponding transmission peaks) become closer together as the frequency of the incident radiation is increased. By plotting a graph of frequency against mode number (deduced from the frequency of each consecutive reflection min-

imum), it is possible to observe a linear, non-dispersive region at lower frequencies for the metamaterial as well as the non-linear dispersive region at higher frequencies. The frequency range over which the metamaterial is non-dispersive is directly related to the refractive index of the material, hence the array of solid copper cubes with the lowest refractive index (1.8 ± 0.2) has the largest frequency range over which the the array is non-dispersive. This is shown in Figure 7.4(a) where the first three modes are equally spaced in frequency and dispersion does not occur until 3.3 GHz. As the refractive index of the plated cube array is higher (3.7 ± 0.2), it is only the first two modes that are equally spaced in frequency, and the EM properties of the array become dispersive at a reduced frequency of 1.2 GHz as shown in Figure 7.4(b). Lastly, the structured cube array has the highest refractive index of 4.1 ± 0.1 and hence the EM properties of the array become dispersive at a frequency of 0.8 GHz (as shown in Figure 7.4(c)).

The peaks and minima are equally spaced for a non-dispersive material, however, for a dispersive material, the peaks and minima are not equally spaced and occur at different frequency intervals. Figure 7.5 shows experimental results for all three different metamaterials, along with finite element method modelling of the systems calculated using Ansys HFSS [162]. For the case of an array of solid cubes (Figure 7.5), 5 distinct transmission peaks (and corresponding reflection minima) associated with the five standing wave eigenmodes of the six unit cell repeat structure in the $\underline{k}$ direction are present as well a DC mode. All three metamaterial samples show the similar trend of transmission peaks that are initially equally spaced, however, at higher frequencies the peaks becoming closer together with increasing frequency as the Brillouin zone boundary (internal wavelength equalling twice the unit cell) is approached [163]. This non-uniform spacing is indicative of dispersive effective values of the permittivity and the permeability. The progression from Figure 7.5(a) to Figure 7.5(c) shows a compression in the spacing of the transmission peaks at lower frequencies due to the higher effective refractive index. It should also be noted that there will be photonic band gap around the Brillouin zone boundary at higher frequencies within which no power is transmitted through the metamaterial samples. The total scattered power (reflected intensity + transmitted intensity) is reduced in the experimental data at higher frequencies which suggests an increase in the inherent loss of the metamaterial. The origin of this inherent loss is most likely the frequency-dependent loss tangent present in the FR4 circuit board. From measuring the position in frequency of the first peak, the refractive index at low frequencies can be deduced for the metamaterials. The position in frequency of the first peak was found at 1.08 GHz for the solid cubes, 0.60 GHz for the plated cubes and 0.54 GHz for the structured plated cubes, corresponding to refractive indices of 2.0, 3.7 and 4.1 respectively.

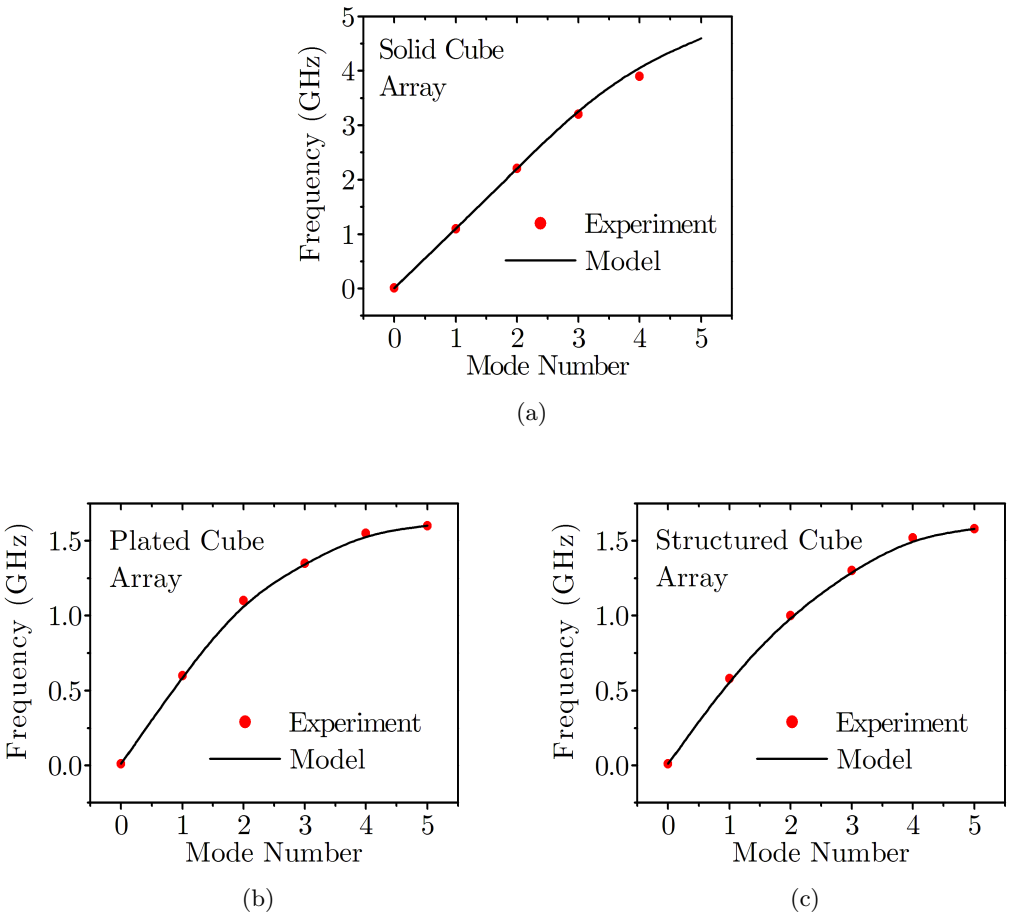

Figure 7.4: Plot of frequency as a function of the mode number for (a) the solid cube array, (b) the plated cube array and (c) the structured cube array. Each plot shows both experimental results (points) and FEM numerical modeling results (solid lines).

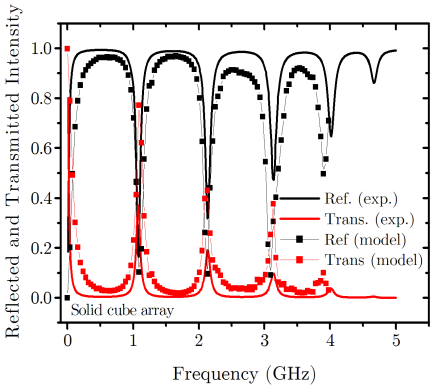

(a)

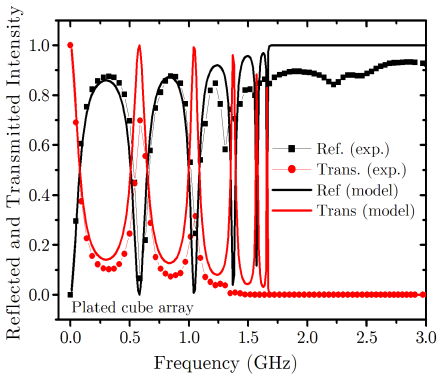

(b)

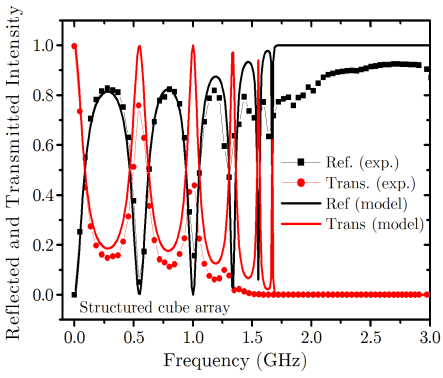

(c)

Figure 7.5: Reflected and transmitted intensity as a function of frequency for (a) the solid cube array, (b) the plated cube array, and (c) the structured cube array. Each plot shows both experimental results (points) and FEM numerical modeling results (solid lines).

Type of array	ε'	μ'	n
Solid cube array	26 ± 1	0.13 ± 0.02	1.8 ± 0.2
Plated cube array	19 ± 1	0.72 ± 0.02	3.7 ± 0.2
Structured cube array	18 ± 2	0.92 ± 0.03	4.1 ± 0.1

Table 7.1: The relative real permeability, permittivity and refractive index for the solid, plated and structured cube arrays in the frequency band from 10 to 500 MHz as extracted from the Fresnel fitting algorithm.

7.4.2 Deducing the permittivity and permeability for the three cubic metamaterials

Figure 7.5 allows the frequency range over which the metamaterial is non-dispersive to be determined, and hence the frequency over which the fitting routine can be implemented. Between 10 and 500 MHz, all three metamaterial samples were non-dispersive, hence the fitting routine method can be utilised over this frequency range for extracting the effective permeability and permittivity . The results over this range are shown in Figure 7.6 where both the experimentally measured reflection and transmission amplitudes (continuous line) are plotted as a function of frequency along with the data from the fitting routine (discrete symbols). From these three fits, for each of the three different metamaterials, values for the permeability and permittivity are deduced, as well as the effective refractive index, n, for each of the three types of cube array. It can be noted that the values given in Table 7.1 for the refractive index (n) are almost the same as the values estimated above from the first peak measurement.

The extracted electromagnetic parameters from each of the three different types of metamaterial sample are shown in Table 7.1, with the experimentally uncertainty deduced from each sample having been obtained from three independent measurements. The diamagnetic response is supressed in the structured cube array which supports the theory that this structuring greatly suppresses eddy currents.

As discussed earlier in this chapter, the diamagnetic response arises due to the propagation of eddy currents around the faces of the cubic elements. Using FEM modelling, the direction and magnitude of these currents have been analysed to deduce the impact of the plate thickness on the induced currents and hence the diamagnetic response. It was found that the influence of the diamagnetic response was weak for the 2 pairs of faces parallel to the applied magnetic field, as the current loops subtend a small area which leads to an approximately linear relationship between the real part of the permeability and the plate thickness, with the diamagnetic response increasing, and μ' decreasing as the plates thicken. The single pairs of faces that are perpendic-

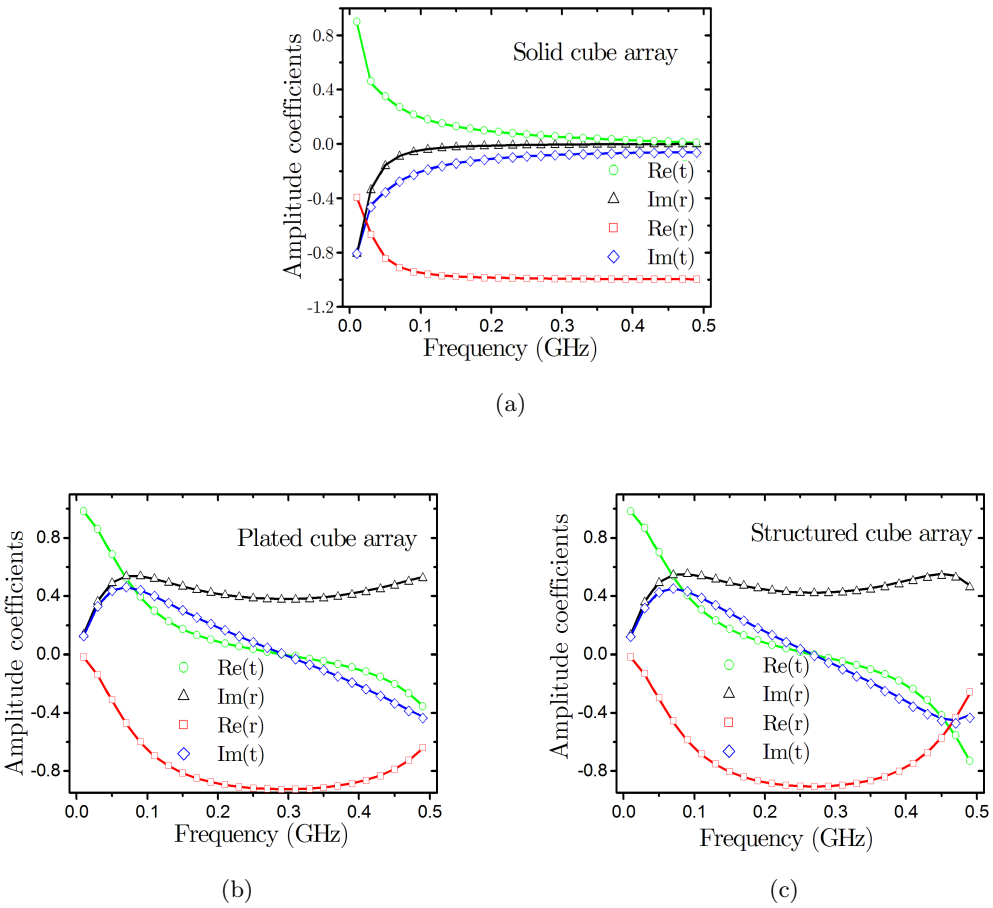

Figure 7.6: Comparison between experiment (lines) and the fit from the MATLAB fmincon fitting routine (open circles) for the reflected and transmitted amplitude coefficients a a function of frequency for; (a) the solid cube array, (b) the plated cube array, and (c) the structured cube array.

ular to the applied magnetic field has a different influence, the plate thickness does not impact the area of the current loop but instead alters the integrated magnitude of the current, which increases with increasing plate thickness, leading to an inverse relationship between the permeability and the plate thicknesses. The dependence on plate thickness of the diamagnetic response of the cubic elements is described in full in the next section in this chapter. From these results, it is apparent that the thinner the metal faces, say copper less than 20 μm thick, the closer the permeability can be to unity and thus higher refractive indices can be achieved. (Note that once the metal thickness is less than the skin-depth thick, this simplistic view fails). When progressing from the plated cube array to the structured cube array, the permittivity falls from 19 to 18. The reduction in permittivity is due to the metal area decreasing, however, the reduction is not as great as naively expected because the slats screening out the incident electric field and hence producing the same dielectric response as a solid face, as the slats essentially act like a wire grid polariser. This is possible as the slats on the structured cubes are close enough together that the fringing fields overlap. To further increase the permittivity, the spacer material can be replaced with a material of higher permittivity than FR4 or using a spacer of reduced thickness. These simple modifications of the existing structures will provide a route to exceptionally high refractive index metamaterials with independent control of the electromagnetic parameters within the constraints that $\varepsilon' > 1$ and $0 < \mu' < 1$. Due to their sub-wavelength size, they have the potential to be used in graded index devices.

7.5 Dumbbell Arrays

In this section, an array of dumbbell-shaped elements is modelled. The dumbbell elements each possess two plates, and, as individual plate pairs are isolated (unlike the cube models), the effective real permittivity and permeability for this array aligned parallel or perpendicular to the applied magnetic ($\underline{B}$) or electric field ($\underline{E}$) can be deduced. The reason for this systematic study is to fully understand how each pair of dumbbell plates affect the permittivity and permeability of the array at low frequencies (10 - 500 MHz) where the metamaterial is non-dispersive. The dumbbell structure was chosen as it allows individual pairs of faces to be tested in isolation. The array of dumbbells is modelled using FEM numerical modelling with the array infinite in $\underline{E}$ and $\underline{B}$ and 6 elements long in the propagation direction (in the same manner that the copper cube arrays were modelled). The plate thickness and central spoke thickness was varied in this model, with the dependence of the permittivity and permeability on the plate thickness and spoke width is quantified and repeated for the two orthogonal directions of $\underline{E}$ and $\underline{B}$ (i.e. for the case when the two dumbbell plates are first parallel

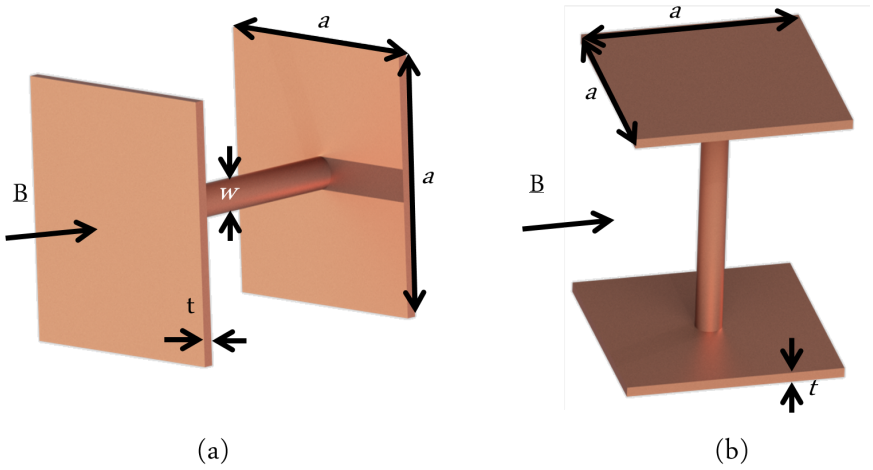

Figure 7.7: A copper dumbbell element comprising of two plates of thickness $'t'$ and length, $'a'$, electrically connected via a central rod of width $'w'$ orientated (a) with the plates perpendicular to the applied magnetic field and (b) with the plates orientated parallel to the applied magnetic field.

to $\underline{\mathrm{E}}$ and perpendicular to $\underline{\mathrm{B}}$ and vice-versa.

Figure 7.7 shows a single dumbbell orientated (a) with the dumbbell plates perpendicular to the applied magnetic field and (b) with the plates orientated parallel to the applied magnetic field. Three quantities are labelled; the plate thickness t, the plate area, a^2 and the width of the central spoke w. In the following study, both the plate-thickness and the central rod-width will be varied and values of permittivity and permeability deduced.

Figure 7.8 shows a single element of an array of dumbbells each orientated both parallel and perpendicular to $\underline{\mathrm{B}}$. The magnitude and direction of the surface currents are shown at an instantaneous point in phase plotted by FEM modelling at 10 MHz. It is noted that these dumbbell elements are part of an infinite array (in the electric and magnetic field direction) hence the electromagnetic parameters deduced later are the effective values from the collective response of the array.

The applied magnetic field induces eddy currents on the copper dumbbell which flow around the faces. Taking $a = 10$ mm and $t = 1$ mm, then, in the case of Figure 7.8 (a), the currents flow around each face which have an area of 100 mm^2 while in Figure 7.8(b) the area of the current loop is reduced to 10 mm^2. Therefore the area enclosed by the eddy current loops in Figure 7.8(a) is far larger than in Figure 7.8(b) hence dumbbells with faces perpendicular to $\underline{\mathrm{B}}$ provide a far stronger diamagnetic response compared to dumbbells with faces parallel to $\underline{\mathrm{B}}$. This is reflected by the corresponding permeability values which were found to be 0.43 (for Figure 7.8(a)) and 0.84 (for Figure 7.8(b)). This

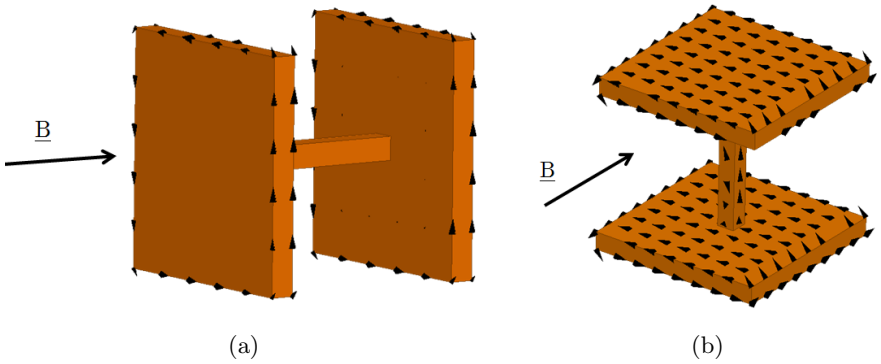

Figure 7.8: (a) A single dumbbell orientated with the applied magnetic field perpendicular to the dumbbell faces and (b) A single dumbbell orientated with the applied magnetic field parallel to the faces. The black arrows on each dumbbell show the induced eddy current flow direction at an instantaneous point in phase at a frequency of 10 MHz.

significant increase in permeability can be utilised in the original cubic metamaterials by removing the pair of faces perpendicular to $\underline{B}$ to enhance the permeability of the metamaterial. It should be noted that removing pairs of plates from the cubic structure means that the resulting dumbbell array is no longer isotropic, and the EM properties are dependent on the polarisation of the incident radiation.

Figure 7.9 shows FEM numerical modelling results for the dependence of permeability on the plate thickness for both orientations of $\underline{B}$ (with $\underline{B}$ perpendicular to the pair of plates in 7.9(a) and with $\underline{B}$ parallel to the pair of plates in 7.9(b)). A linear dependence between permeability and the plate thickness with $\underline{B}$ perpendicular to the parallel plates is observed in 7.9(b) as there is a linear change in area enclosed by the induced current loop and hence a linear variation in the diamagnetic field strength. An inverse relationship between μ' and the plate thickness is found in Figure 7.9(a). If the total magnetic moment of each individual dumbbell is considered, both the area subtended by the current loop (the plate area) and the magnitude of the current (which is dictated by the plate thickness) directly contribute. Hence, increasing the plate thickness leads to the integral of the current density increasing, which strengthens the diamagnetic response.

Also plotted in Figure 7.9 is the permeability dependence on the central rod width, w. The jack thickness in the case of Figure 7.9(a) where the plates are perpendicular to $\underline{B}$ as the central rod is screened from incident radiation by the presence of the plates. However, in the case of Figure 7.9(b) where the plates are parallel to $\underline{B}$, the central rod contributes further to the diamagnetic response as the induced currents are able to

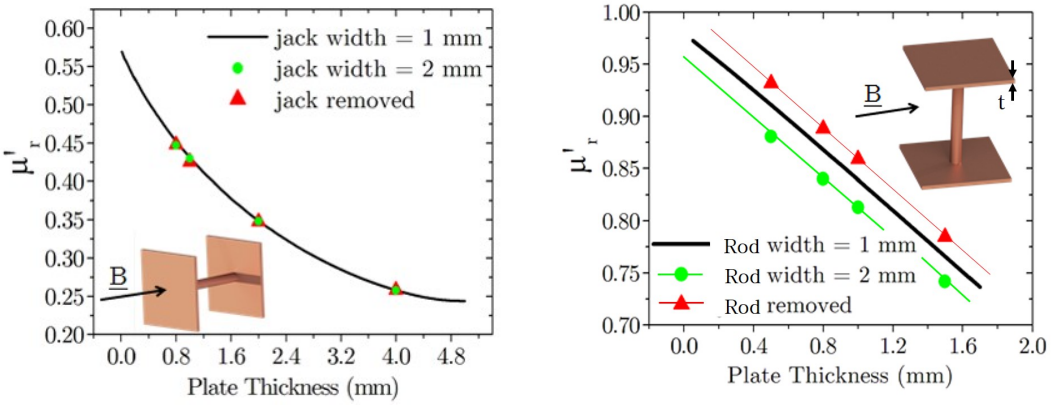

(a) (b)

Figure 7.9: Numerical modelling results for the real permeabillity (at 10 MHz) as a function of the plate thickness for an array of dumbbells for; (a) with the array of dumbbells orientated perpendicular to the applied magnetic field and (b) with the array of dumbbells orientated parallel to the applied magnetic field.

propagate around it, hence removing the central rod provides the largest permeability value.

Figure 7.10 shows FEM numerical modelling results for the dependence of the permittivity on plate thickness t and central rod width w. Figure 7.10(a) where the plates are perpendicular to $\underline{E}$, shows that permittivity is independent of the plate thickness and remains constant at a value of 5.8. This is due to the capacitive coupling between adjacent dumbbells being dominated by the plate area (10×10 mm). However in the case of Figure 7.10(b) where the plates are parallel to $\underline{E}$, the permittivity is linearly dependent on plate thickness and varies between 3.2 (at a plate thickness of 0.8 mm) and 5.7 (at a plate thickness of 4 mm). The increase in the permittivity with plate thickness is due to the capacitive coupling between the edges of adjacent dumbbell plates increasing with the edge area ($a \times t$).

With regards to the role of the central rod, Figure 7.10(a) demonstrates that removing the central rod inhibits the flow of charge between the two plates that form the dumbbell and hence stops the dumbbell from becoming effectively polarised, causing the permittivity to drop from 5.7 to 1.2 (for a plate thickness of 0.45 mm). However, the permittivity is not independent of the plate thickness as it gradually increases with increased plate thickness from 1.2 to 1.5. This is due to the distance between plates from a single dumbbell decreasing as the plates become thicker (for a fixed pitch), which increases the capacitive coupling between these plates (the capacitive coupling between plates of adjacent dumbbells remains constant). In the case of Figure 7.10(b),

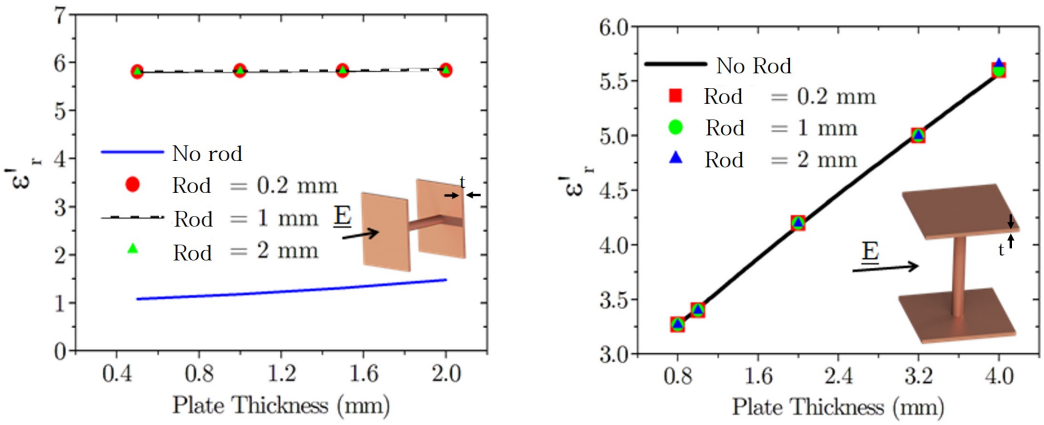

Figure 7.10: Numerical modelling results for the real permittivity (at 10 MHz) as a function of the plate thickness for an array of dumbbells for (a) with the array of dumbbells orientated perpendicular to the applied electric field and (b) with the array of dumbbells orientated parallel to the applied electric field.

the central rod does not impact the permittivity as, providing the central rod width is wide enough to conduct, it does not contribute to the capacitive coupling.

7.6 Conclusions

In conclusion, a broadband (10 to 500 MHz) metamaterial has been designed and fabricated that allows independent control of both its effective permeability and effective permittivity. The metamaterial is comprised of arrays of metallic cubes, with the EM properties controlled by appropriately structuring of the cube faces. The metamateral possesses a high effective permittivity whilst the effective permeability is held close to unity by suppressing the usual diamagnetic response. The permeability increases from a value of 0.13 ± 0.02 (strongly diamagnetic) for solid metallic cubes to 0.90 ± 0.05 for the cubes with faces that have been structured. Patterning the cube faces decreases the permittivity from 26 ± 2 to 18 ± 2 due to the reduction in face area. Together this results in an increase of the refractive index from 1.8 ± 0.2 to 4.1 ± 0.1.

To understand the role of the cube parameters, (such as the thickness of the cube faces and the width of the central conducting central rod) a simpler system containing arrays of dumbbells was modelled with the applied magnetic/electric field oriented both parallel and perpendicular to the plates of the dumbbell. From this simple study on arrays of dumbbells, it can be concluded that the central conducting central rod is crucial for maintaining a high permittivity however it does not effect the permeability.

The highest possible permeability is obtained by reducing the thickness of the pairs of dumbbell plates, and in the case of cubes, removing the two plates perpendicular to the applied magnetic field.

Understanding the EM response of both the dumbbell arrays and arrays of structured cubes allows for metamaterials to be designed with even high permittivity values and permeability values that can be easily tuned between near 0 and unity. Such an increase in the permittivity provides opportunities for designing ultra high refractive index materials, while the ability to control the refractive index provides a basis for the development of broadband metamaterials with bespoke electromagnetic parameters for applications in the field of microwave transformation optics.

Lastly, the dispersion of the EM properties in the three different cubic metamaterials is observed. While the solid cube array, with the lowest refractive index (1.8 ± 0.2) possessed the largest non-dispersive frequency range, (from 10 MHz to 3.3 GHz) the plated and structured cube arrays with increased refractive indices (of 3.7 ± 0.2 and 4.1 ± 0.1 respectively) had reduced non-dispersive frequency ranges of 1.2 GHz and 0.8 GHz.

Chapter 8

Conclusions

The work presented in this thesis documents original investigations separated into four experimental chapters, as well as chapters detailing the methodology and theory which underpins the experimental work. Controlling the electromagnetic (EM) response of magnetic materials and metamaterials was the main focus of the work, and has been demonstrated by utilising the magnetic properties of ferrites and the structuring of metallic and ferrite cubes to produce exotic material properties. These materials are impedance matched to free space, possess independently tailored values of permittivity and permeability or have a high refractive index at MHz and low GHz frequencies.

The first experimental chapter in this thesis (Chapter 4) uses MnZn ferrite and PTFE to produce ferrite composites with the % vol. of ferrite varied between 0 and 80%. A novel cold pressing method was used to fabricate the composite materials, which proved advantageous over previous methods as it is very simple to implement while allowing for the same filler material (PTFE) to be used across the full range of volume fractions of the ferrite filler. This fabrication technique was also reproducible and did not require elevated temperatures or pressures. The reproducibility of this method was confirmed by both measuring the density of 5 independently made composites (for each % vol.), as well as measuring the EM properties of each of the composites made. In total, 6 volume fractions were studied between 0 and 80% vol., and for each volume fraction, 5 independent samples were fabricated. The average complex permittivity and permeability of the 80 % vol. composites was 180 $\pm$ 10 and 23 $\pm$ 2 respectively (at 10 MHz). The Lichtenecker mixing formula was then shown to agree with the data in the form of a straight line graph of the logarithm of the complex permittivity and permeability as a function of % vol. of filler. This technique allowed the permittivity and permeability for any % vol. between 0 and 80 to be deduced from the plot, hence allowing the fabrication of materials with predetermined EM properties. A stripline connected to a vector network analyser was used to electromagnetically characterise

the composites between 10 MHz and 4 GHz. The implications of micron-sized air gaps between the stripline and the sample in this material characterisation method was investigated and led to modifications to both the sample shape and an analytical description of the permittivity and permeability dependence on these micron-sized air gaps. Lastly, the cold pressing technique was extended to use cellulose as the matrix material, which extended the upper limit of the % vol. of ferrite filler to 85%. Cellulose could be advantageous over PTFE in some cases as it possesses a higher permittivity than PTFE at MHz frequencies, as well as being biodegradable and abundant. Aluminium and barium titanate powders were also used as alternative filler materials as well as being combined with ferrite to produce three-part composites. The EM properties of these cold pressed composites were studied using the same stripline method, and, in the case of the cellulose composites, the Lichtenecker mixing formula was applied to observe a linear relationship between the natural logarithm of the permittivity/permeability and volume concentration of the filler.

The second experimental chapter in this thesis (Chapter 5) presents the use of the cold pressing method to fabricate NiZn ferrite-PTFE composites. The focus of this chapter is to study the effect of NiZn ferrite particle diameter on the complex permittivity and permeability of ferrite composites for a range of NiZn ferrite volume fractions. The NiZn ferrite was sieved into eight particle diameter ranges from less than 20 μm to 125 μm and for each ferrite particle diameter range, four different volume fractions were investigated. It was found that while the permittivity was weakly dependent on the ferrite particle diameter, the permeability was more strongly dependent on it, therefore the EM properties of the composites could be tuned to some degree by particle diameter control. One demonstration of this control was achieved by producing two impedance-matched composites, which could only be achieved via simultaneously controlling the ferrite volume fraction and particle diameter. A 50 % vol. composite containing NiZn ferrite of average particle diameter 35 μm and a 70 % vol composite containing NiZn ferrite of average particle diameter 20 μm were both impedance matched to free space, with their values of refractive index being equal to 6.1 and 6.9 respectively. The Lichtenecker mixing law was also used to plot linear dependencies between the natural logarithm of the permittivity/permeability and the volume fraction of ferrite, while, in contrast to Chapter 4, the Lichtenecker mixing law was tested for different particle diameter ranges. The gradient from each of the Lichtenecker plots (obtained from fitting linear dependencies), were plotted as a function of average particle diameter, and found to obey Snoek's law. This result suggested that both the Lichtenecker mixing law and Snoek's law are valid for all the particle diameter ranges studied in this chapter. Lastly, three-part composites consisting of NiZn ferrite, MnZn ferrite and PTFE were fabricated to demonstrate that the addition of a third compo-

nent can provide an extra degree of control required for impedance matching to free space. In this case, the refractive index of the impedance matched composite was 16.1 from 10 - 50 MHz. The control obtained from varying both the ferrite particle diameter and by adding a third component (MnZn ferrite) allows for desired EM properties to be engineered, which would not be possible by controlling the volume fraction of a two-part composite alone.

In the third experimental chapter in this thesis (Chapter 6) the concept of metamaterials is used to construct an anisotropic array of ferrite cubes, that demonstrated broadband impedance matching, whilst possessing a refractive index of 9.5 from 10 to 70 MHz (for a specific linear polarisation). While at low frequencies, the reflection was less that 0.3%, at higher frequencies (200 MHz), the metamaterial structure acted as an electromagnetic wave absorber of sub-wavelength thickness. The metamaterial designed allowed for independent control of the complex permittivity and permeability via the spacing of the ferrite cubes in three orthogonal directions. This design can be utilised for different materials where independent control of the EM properties is desired. The permittivity and permeability dependence of the metamaterial on the spacing of the cubes in the magnetic and electric field directions was investigated both analytically and numerically. The analytic solutions to similar metamaterial arrangements found that a linear dependence existed between the permittivity and the cube spacing parallel to the applied electric field and also between the permeability and the cube spacing parallel to the applied magnetic field. However, when the cube spacing is varied orthogonal to the applied electric field, an inverse relation between the permittivity and the cube spacing is observed (the same result is obtained between the permeability and the cube spacing orthogonal to the applied magnetic field). The dependence of the EM properties of this metamaterial on the cube spacing allows for independent control of the permittivity and permeability desired for engineering devices with tailored EM responses.

Lastly, in Chapter 7 the EM response of a broadband (10 - 500 MHz) metamaterial is investigated which allowed for the permittivity and the diamagnetic response to be controlled independently through appropriate structuring. The metamaterial was comprised of arrays of copper cubic elements, with the faces of the cubes structured in such a way as to suppress the diamagnetic response. It was found that by appropriate structuring of the cube faces, the permeability increased from 0.13 ± 0.02 (strongly diamagnetic) to 0.90 ± 0.05 (weakly diamagnetic). The permittivity was weakly affected by the structuring of the cube faces and was found to only decrease from 26 ± 2 to 18 ± 2, which was primarily due to the reduction of the plate area. In order to understand the effect of cube parameter variation on the permittivity and permeability of the metamaterial, a simpler metamaterial design was modelled to isolate specific pa-

rameters. The results from this modelling concluded that the central conducting spoke, which electrically connects adjacent cube faces, was crucial for maintaining a high permittivity, however it did not effect the permeability. The highest possible permeability was obtained by reducing the thickness of the pair of cube faces arranged perpendicular to the applied magnetic field. Numerical modelling determined in the latter part of this chapter enable metamaterials to be designed with far higher permittivity values, while the permeability of the metamaterial could be varied between near zero and unity. The ability to control the permittivity and diamagnetic response of this metamaterial via appropriate structuring allows for the design of broadband metamaterials with bespoke EM properties.

Chapter 9

Publications and Conferences

9.1 Publications and presentations

9.1.1 Refereed papers

- 'Heavily loaded ferrite-polymer composites to produce high refractive index materials at centimetre wavelengths', L. Parke, I. R. Hooper, R. J. Hicken, C. E. J. Dancer, P. S. Grant, I. J. Youngs, J. R. Sambles and A. P. Hibbins, APL Mater., 1, 042108 (2013) doi 10. 1063/1.4824039.

- 'Broadband impedance-matched electromagnetic structured ferrite composite in the megahertz range', L. Parke, I. J. Youngs, A. P. Hibbins and J. R. Sambles, App. Phys. Lett., 104, 221905 (2014) doi 10. 1063/1.4881186.

- 'Independently controlling permittivity and diamagnetism in broadband, low-loss, isotropic metamaterials at microwave frequencies', L. Parke, I. R. Hooper, E. Edwards, N. Cole, I. J. Youngs, A. P. Hibbins and J. R. Sambles, Appl. Phys. Lett., 106, 101908 (2015) doi 10.1063/1.4915097.

9.1.2 Oral presentations

- 'Broadband impedance-matched electromagnetic metamaterial in the MHz range', L. Parke. I. J. Youngs, A. P. Hibbins, J. R. Sambles, META - Singapore, 5th International Conference on Metamaterials, Photonic Crystals and Plasmonics (2014).

9.1.3 Poster presentations

- 'Magnetic Composites for Spatial Transformations and Impedance Matched Materials', L. Parke, I. R. Hooper, I. J. Youngs, A. P. Hibbins, J. R. Sambles,

NANOMETA - Austria, 4th International Topical Meeting on Nanophotonics and Metamaterials (2013).

- 'Independently Controlling Permittivity and Permeability in Broadband, Low-Loss, Isotropic Metamaterials at Microwave Frequencies', L. Parke, I. R. Hooper, I. J. Youngs, A. P. Hibbins, J. R. Sambles, NANOMETA - Austria, 5th International Topical Meeting on Nanophotonics and Metamaterials (2015).
- 'Independent Control of the Electromagnetic Properties in Magnetic Composites', L. Parke. I. J. Youngs, A. P. Hibbins, J. R. Sambles, NANOMETA - Austria, 5th International Topical Meeting on Nanophotonics and Metamaterials (2015).
- 'Independent Control of the Electromagnetic Properties in Magnetic Composites', L. Parke. I. J. Youngs, A. P. Hibbins, J. R. Sambles, The Royal Society at Chicheley Hall; Spatial transformations: from fundamentals to applications.

9.1.4 Oral presentations and posters - QUEST

The Quest for Ultimate Electromagnetics using Spatial Transformations (QUEST) is a five year, multi-disciplinary collaboration between Queen Mary, University of London, the University of Oxford and the University of Exeter (Programme Grant number EP/I034548/1). As part of this collaborative project, six oral presentations and 6 poster presentations were given between February 2012 and October 2014, and were accompanied by a series of bi-monthly reports which documents the work presented in this Thesis. These presentations were held in a range of locations throughout the UK including London, Oxford and Exeter.

Chapter 10

Future Work

10.1 Increasing the Resonant Frequency of Ferrite Composites

A number of exotic designs inspired by transformation optics are limited by their required material parameters. One such limitation is the requirement for a tunable permeability at GHz frequencies. This limitation means that many lens and cloaking devices rely on an all dielectric approach whereby the permeability is set to 1, hence the device is not impedance matched [164]. Having the ability to manipulate the permeability provides researchers with another degree of freedom when it comes to designing lenses, antennas and cloaks [127, 165].

Ferrites may provide the desired magnetic response if they can be modified in such a way as to increase the domain wall and gyromagnetic resonant frequencies. The ferrite composites studied in this thesis possess a resonant frequency that is dependent on the DC value of the real permeability: there is an inverse relationship between the DC permeability and the resonant frequency which is described by Snoeks Law [6]. The position of this resonant frequency is typically in the MHz range, resulting in poor magnetic performance above this frequency i.e. the real permeability above the resonant frequency falls to approximately unity.

Recent studies into exceeding the Snoek's limit [166, 167] have lead to research into the particle size and particle shape dependent magnetic properties in magnetic composites. Although the resonance frequency can be enhanced by introducing shape anisotropy, as shown in work by Guozhi *et al.* [58], it is a great challenge to increase both the resonance frequency and the permeability simultaneously.

It was found in Chapter 5 that varying the particle size of magnetic inclusions in a dielectric matrix altered both the resonant frequency and the permeability, however,

the magnetic particles were not small enough to be super-paramagnetic. When the volume of a particle is reduced so that it is on the order of nanometers, the magnetic anisotropy energy (described in Chapter 2) becomes comparable to the thermal energy (which dictates the probability that the magnetization vector will reverse in direction by thermal fluctuation.) For single domain particles, the frequency dependent permeability is dictated by both the magnetic anisotropy energy and the thermal energy. When the frequency dependent permeability becomes dominated by the thermal energy rather than the magnetic anisotropy energy, a relaxation time is introduced which describes how rapidly the superparamagnetic relaxation takes place. As there are two relaxation phenomena in superparamagnetic particles (the gyromagnetic resonant frequency and superparamagnetic relaxation) both of which are dependent on the magnetic permeability, a challenging study would be to determine whether the superparamagnetic relaxation frequency could be greater than the gyromagnetic resonant frequency, hence surpassing the Snoek Limit. A study by Ning-Ning *et al.* [166] has found that monodispersed magnetic nanoparticles of iron oxide (Fe_3O_4) possess a resonant frequency of 5.3 GHz, while the resonant frequency for bulk Fe_3O_4 is only 1.3 GHz.

A second route to exceeding the Snoek Limit in magnetic composites is to use a core shell structure. In fact, Ning-Ning *et al.* extended their study of magnetic nanoparticles by coating them with an insulating layer of silicon oxide (SiO_2) which further increased the cut-off frequency to 6.9 GHz (at which the real permeability fell from 1.3 to 1). The concept of the core-shell structure could provide significant improvements in the high frequency permeability of magnetic composites. Spherical carbonyl iron particles that have a core shell structure, in which there is a central core of pure iron surrounded by alternating layers of iron oxide, are effective at reducing eddy current losses whilst maintaining the large magnetic response of carbonyl iron. Initial studies into such 'onion skin' structured particles [168] have found that the frequency dispersion of both the permeability and permittivity is strongly dependent on their exact micro-structure. By understanding this dependence on microstructure, an optimum microstructure can by deduced that would give a response to exceed Snoek limit.

10.2 Measuring the Coercivity of Magnetic Materials

Chapter 2 investigated the effect of ferrite particle size on the EM properties of NiZn ferrite composites. The results showed that the permeability increased with increasing ferrite particle size. To explain this, the grain structure and domain structure within the ferrite particles were described with previous investigations into this phenomena documenting the coercivity dependence on the ferrite particle size. As an important

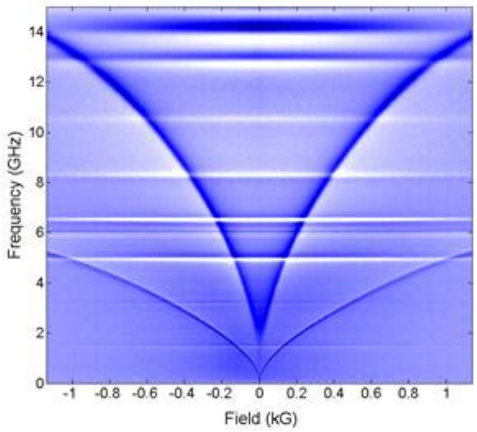

Figure 10.1: A plot of frequency as a function of the applied DC magnetic field for a sample of YIG/Cu/Co (a ferrimagnetic garnet). The colour represents the magnitude of the transmission with the dark bands representing minimum transmission. The upper and lower curves correspond to the Co and YIG resonances respectively. (This example data was taken by Dr Leigh Shelford from the Magnetics Group at Exeter University).

extension for this piece of work, the coercivity of ferrite composites should be measured. As a preliminary investigation, the coercivity of 70% vol. NiZn ferrite-PTFE composites containing different ferrite particle sizes was attempted using the VNA-FMR set-up. The set-up consists of an open waveguide that sits in a DC magnetic field supplied by an electromagnet, the waveguide is connected to a VNA which measures the complex reflection and transmission from the sample as a function of frequency. The direction of the DC magnetic field supplied by the electromagnet is perpendicular to the direction of the AC magnetic field associated with the open waveguide to provide the maximum torque to the magnetisation vectors present in the ferrite. In the experiment, the magnitude of the transmission is measured both as a function of frequency and as a function of the DC magnetic field. The applied magnetic field is swept from the minimum value (-1 kG) to 0 kG before being increased in the opposite direction from 0 kG to a maximum of 1 kG. The frequency of the ferromagnetic resonance is dependent on the magnitude of the DC magnetic field and decreases significantly to a minimum as the applied magnetic field is swept to zero before increasing again as the applied field is increased in the opposite direction. The minimum frequency point corresponds to the direction of the magnetisation switching by 180° (see Figure 10.1).

Figure 10.1 shows the position of the resonant frequency change as the applied DC field is swept for a sample of YIG / Cu / Co with the upper and lower curves in the figure corresponding to the Co and YIG resonances respectively. The minimum resonant frequency point occurs when the magnetic energy is at a minimum. The

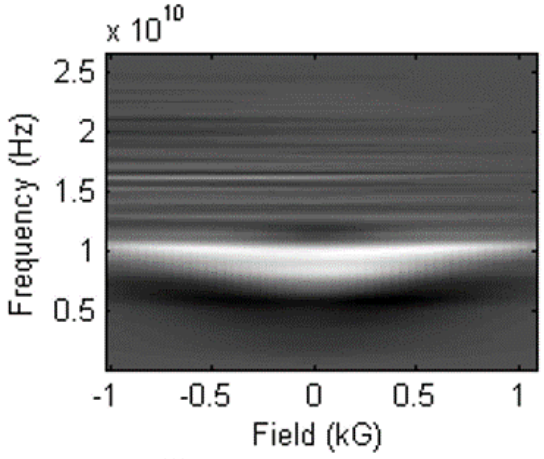

Figure 10.2: A plot of frequency as a function of the applied DC magnetic field for a sample of 70% vol. NiZn ferrite composite of particle size 63-75 μm. The colour represents the magnitude of the transmission with the single dark curve representing minimum transmission. The black curve corresponds to the gyromagnetic resonance.

position of this minimum frequency depends on a number of parameters, including the magnetic anisotropy, and does not always occur at zero external field, as in the case of Figure 10.1. The coercivity can be extracted where the frequency vs. field curve has a sharp change due to a switch in direction of the magnetisation vector. As the magnetisation switches suddenly at the coercive field the magnetic energy also falls, and with it the ferromagnetic resonance frequency. Observation of this behaviour depends on how sharp the switch is and how large the coercive field is. In the example shown in this figure, the coercivity is too small to see clearly.

The measurement technique outlined in the previous section works well for anisotropic samples that possess a magnetically easy crystal axis as the sample can be uniformly magnetized with relatively low fields. Problems arise when the sample of interest is isotropic and does not possess an easy axis, this is suspected to be the case for the ferrite composite samples as each individual particle will possess a crystal easy axis in a different direction.

Figure 10.2 shows the position of the resonant frequency (shown by the dark band) decrease as the magnitude of the applied DC field is decreased for a sample NiZn ferrite composite sample. It is clear that the effect of the applied magnetic field on the position of the resonant frequency is very weak with a loss of signal being observed at small values of applied field. This indicates that the sample is not fully magnetised and hence requires a much stronger field to observe a sharp switch in the magnetisation which is required to extract the coercivity. Extracting the coercivity for these samples will further verify the dependence of the magnetic properties of ferrite composites on

particle size.

10.3 Meta-ferrites

At present, split ring resonators are used to provide an artificial magnetic resonance at GHz frequencies, where each split ring resonator or meta-atom is on the order of mm [169]. Magnetic resonant behaviour can also occur in ferrites. Combining metamaterial structure with magnetic materials such as ferrites, may provide a route to creating magnetic metamaterials with a resonance in the GHz frequency range, but unlike split ring resonators, the meta-atoms in this design would be ultra sub-wavelength. Previous investigators [170–172] have studied the concept of combining metamaterial designs with magnetic materials to demonstrate sub-wavelength confinement of microwaves due to magnetic dipolar modes in 2D ferrite disks. In this case, mm-sized ferrite disk resonators were used to resonate at cm wavelength EM radiation (approximately 10 GHz). The future work concept presented here would involve fabricating nm sized ferrite disks (using a laser writer) and spacing them isotropically in a 2D array. Many of these arrays would then be stacked to form a 3D magnetic metamaterial. Unlike the ferrite composites fabricated in this thesis, this design would provide a much larger degree of control over the magnetic resonant properties as, in the case of these ferrite disks, the ferromagnetic resonance would rely on the shape and spatial arrangement of individual disks.

References

[1] Zouhdi, S., Sihvola, A., and Vinogradov, A. *Metamaterials and Plasmonics: Fundamentals, Modelling, Applications*. Springer (2008). 1

[2] Goldman, A. *Modern Ferrite Technology*. Springer (2010). 1, 2, 11, 16, 62, 85, 98

[3] The Ceramic Society of Japan. *Advanced Ceramic Technologies & Products*. Springer (2012). 1

[4] Clarricoats, P. *Microwave Ferrites*. Chapman and Hall (1961). 2

[5] Smith, J. and Wijn, H. *Ferrites*. John Wiley & Sons (1959). vii, 2, 17

[6] Snoek, J. Dispersion and absorption in magnetic ferrites at frequencies above one Mc/s. *Physica*, **4**, 207 (1948). 2, 21, 22, 62, 82, 93, 105, 119, 145

[7] Kruželák, J., Dosoudil, R., Hudec, I., and Sykora, R. Influence of strontium ferrite on properties of composites based on polar and non-polar rubber matrices. *Journal of Electrical Engineering*, **63**, 137 (2012). 3, 63

[8] Tsutaoka, T. Frequency dispersion of complex permeability in MnZn and NiZn spinel ferrites and their composite materials. *Journal of Applied Physics*, **93**, 2789 (2003). 3, 63, 94, 103

[9] Tsutaoka, T. Frequency dispersion of complex permeability in MnZn and NiZn spinel ferrites and their composite materials. *Journal of Applied Physics*, **93**, 2789 (2003). 3, 63

[10] Mosallaei, H. and Sarabandi, K. Magneto-Dielectrics in Electromagnetics: Concept and Applications. *IEEE Transactions on Antennas and Propagation*, **52**, 1558 (2004). 3

[11] Kong, L.B., Li, Z.W., Lin, G.Q., and Gan, Y.B. Ni-Zn Ferrites Composites With Almost Equal Values of Permeability and Permittivity for Low-Frequency Antenna Design. *IEEE Transactions on Magnetics*, **43**, 6 (2007). 3, 98

[12] Su, H., Tang, X., Zhang, H., Jing, Y., Bai, F., and Zhong, Z. Low-loss NiCuZn ferrite with matching permeability and permittivity by two-step sintering process. *Journal of Applied Physics*, **113**, 17B301 (2013). 3, 99

[13] Sihvola, A.H. *Electromagnetic mixing formulas and applications*. Institute of Electrical Engineers (1999). 4, 28

[14] Lagarkov, A. and Rozanov, K. High frequency behavior of magnetic composites. *Jounal of Magnetism and Magnetic Materials*, **321**, 2082 (2009).

[15] Rozanov, K.N. and Koledintseva, M.Y. Analytical representations for frequency dependences of microwave permeability. In *2012 IEEE International Symposium on Electromagnetic Compatibility*, volume 324. IEEE (2012). ISBN 978-1-4673-2060-3.

[16] Kiley, E.M., Yakovlev, V.V., Ishizaki, K., and Vaucher, S. Applicability study of classical and contemporary models for effective complex permittivity of metal powders. *The Journal of microwave power and electromagnetic energy : a publication of the International Microwave Power Institute*, **46**, 26 (2012). 4

[17] Garnett, J.C.M. Colours in metal glasses and metal films. *Transactions of the Royal Society*, **CCIII**, 385 (1904). 4, 25

[18] Koledintseva, M.Y., DuBroff, R.E., and Schwartz, R.W. A Maxwell Garnet model for dielectric mixtures containing conducting particles at optical frequencies. *Progress In Electromagnetics Research*, **63**, 223 (2006). 4

[19] Cai, N., Zhai, J., Nan, C.W., Lin, Y., and Shi, Z. Dielectric, ferroelectric, magnetic, and magnetoelectric properties of multiferroic laminated composites. *Physical Review B*, **68**, 224103 (2003). 4

[20] Paterson, J., Devine, R., and Phelps, A. Complex permeability of soft magnetic ferrite/polyester resin composites at frequencies above 1 MHz. *Journal of Magnetism and Magnetic Materials*, **394**, 196 (1999). 4

[21] Bruggeman, D.A.G. Berechnung verschiedener physikalischer Konstanten von heterogenen Substanzen. I. Dielektrizitätskonstanten und Leitfähigkeiten der Mischkörper aus isotropen Substanzen. *Annalen der Physik*, **416**, 636 (1935). 5

[22] Birchak, R., Gardner, L.G., Hipp, J.W., and Victor, J.M. High dielectric constant microwave probes sensing soil moisture. *Proceedings of the IEEE*, **62**, 93 (1974). 5

[23] Lichtenecker, K. Über Elektrische Leitfähigkeit und andere Körpereigenschaften desselben Typus bei binären Aggregaten. *Physikalische Zeitschrift*, **27**, 115 (1926). 5, 25, 28, 29

[24] Shelby, R.A., Smith, D.R., Nemat-Nasser, S.C., and Schultz, S. Microwave transmission through a two-dimensional, isotropic, left-handed metamaterial. *Applied Physics Letters*, **78**, 489 (2001). 5, 122

[25] Pendry, J., Holden, A., Robbins, D., and Stewart, W. Magnetism from conductors and enhanced nonlinear phenomena. *IEEE Transactions on Microwave Theory and Techniques*, **47**, 2075 (1999).

[26] Veselago, V.G. The electrodynamics of substances with simultaneously negative values of permittivity and permeability. *Soviet Physics Uspekhi*, **10**, 509 (1968). 5, 122

[27] Demetriadou, A. and Pendry, J.B. Taming spatial dispersion in wire metamaterial. *Journal of Physics: Condensed Matter*, **20**, 295222 (2008). 5, 122

[28] Choi, M., Lee, S.H., Kim, Y., Kang, S.B., Shin, J., Kwak, M.H., Kang, K.Y., Lee, Y.H., Park, N., and Min, B. A terahertz metamaterial with unnaturally high refractive index. *Nature*, **470**, 369 (2011). 5, 122

[29] Parke, L., Youngs, I.J., Hibbins, A.P., and Sambles, J.R. Broadband impedance-matched electromagnetic structured ferrite composite in the megahertz range. *Applied Physics Letters*, **104**, 221905 (2014). 5

[30] Schurig, D., Mock, J.J., Justice, B.J., Cummer, S.A., Pendry, J.B., Starr, A.F., and Smith, D.R. Metamaterial electromagnetic cloak at microwave frequencies. *Science*, **314**, 977 (2006). 5

[31] Jackson, R. *John Tyndall and the Early History of Diamagnetism*. Annals of Science (2014). 8

[32] Kittel, C. Introduction to Solid State Physics. John Wiley & Sons. (1986). 8

[33] Bertoldi, D.S., Bringa, E.M., and Miranda, E.N. Analytical solution of the mean field Ising model for finite systems. *Journal of physics. Condensed matter : an Institute of Physics journal*, **24**, 226004 (2012). 8

[34] Jia, G., Tu, C., Li, J., Lu, X., You, Z., Zhu, Z., and Wu, B. Spectroscopic properties of Er[3+] transitions in SrWO[4] crystal. *Journal of Applied Physics*, **98**, 093525 (2005). 10

[35] Hornbostel, B., Leute, U., Pötschke, P., Kotz, J., Kornfeld, D., Chiu, P.W., and Roth, S. Attenuation of electromagnetic waves by carbon nanotube composites. *Physica E: Low-dimensional Systems and Nanostructures*, **40**, 2425 (2008).

[36] Feng, Y.; T. Qiu, C. Shen; Li, X. Electromagnetic and absorption properties of carbonyl iron/rubber radar absorbing materials. *IEEE Transactions on Magnetics*, **42**, 363 (2006). 10

[37] Bacon, G.E. *Neutron Diffraction*. Claredon Press, London (1955). 11

[38] Fuller, A. Ferrites at microwave frequencies. Peter Peregrinus (1987). vii, 12

[39] Guillissen, J. and Van Rysselberghe, P.J. Studies on Zinc and Barium Ferrites. *Transactions of The Electrochemical Society*, **59**, 95 (1931). 11

[40] Cullity, B. and Graham, C. *Introduction to Magnetic Materials*. Wiley (2009). 13

[41] Feynman, R. *The Feynman Lectures on Physics Vol. I*. Basic Books (1963). 13

[42] Dunlop, D.J. The rock magnetism of fine particles. *Physics of the Earth and Planetary Interiors*, **26**, 1 (1981). 13

[43] Dionne, G.F. *Magnetic Oxides*. Springer (2009). 14, 15

[44] Ruderman, M.A. and Kittel, C. Indirect Exchange Coupling of Nuclear Magnetic Moments by Conduction Electrons. *Physical Review*, **96**, 99 (1954). 16

[45] Neel, L. Ferromagnetism and Anti-Ferromagnetism. *Nature*, **166**, 777 (1950). 16

[46] Feynman, R. *The Feynman Lectures on Physics, Vol. I*. Basic Books (1963). 17

[47] Loyau, V., Wang, G.Y., Bue, M.L., and Mazaleyrat, F. An analysis of Mn-Zn ferrite microstructure by impedance spectroscopy, scanning transmission electron microscopy and energy dispersion spectrometry characterizations. *Journal of Applied Physics*, **111**, 053928 (2012). 18

[48] Vishwanathan, B. and Murthy, V.R.K. *Ferrite Materials, Science and Technology*. Narosa Publishing House (1990). 19

[49] Wagner, K.W. Erklärung der dielektrischen Nachwirkungsvorgänge auf Grund Maxwellscher Vorstellungen. *Archiv für Elektrotechnik*, **2**, 371 (1914). 19

[50] Koops, C. On the Dispersion of Resistivity and Dielectric Constant of some Semiconductors at Audiofrequencies. *Physical Review*, **83**, 121 (1951). 19

[51] Loyau, V., Wang, G.Y., Bue, M.L., and Mazaleyrat, F. An analysis of Mn-Zn ferrite microstructure by impedance spectroscopy, scanning transmission electron microscopy and energy dispersion spectrometry characterizations. *Journal of Applied Physics*, **111**, 053928 (2012). 19

[52] Adams, T., Sinclair, D., and West, A. Giant Barrier Layer Capacitance Effects in CaCu3Ti4O12 Ceramics. *Advanced Materials*, **14**, 1321 (2002). 19

[53] Ganeshraj, C., Kavita, S., Mahendiran, R., Sharma, N., Das, A., and Santhosh, P.N. Jahn-Teller assisted polaron hopping and associated dielectric response of PrFe0.5Mn0.5O2.95. *Applied Physics Letters*, **103**, 112909 (2013).

[54] Chung, U.C., Elissalde, C., Mornet, S., Maglione, M., and Estournes, C. Controlling internal barrier in low loss BaTiO supercapacitors. *Applied Physics Letters*, **94**, 072903 (2009). 19

[55] Sabu Thomas, Kuruvilla Joseph, S. K. Malhotra, Koichi Goda, M.S.S. *Polymer Composites, Macro- and Microcomposites*. John Wiley and Sons (2012). ISBN 3527645233, 9783527645237. 21

[56] Landau, L. and Lifshits, E. On the theory of the dispersion of magnetic permeabiltiy in ferromagnetic bodies. *Physikalische Zeitschrift der Sowjetunion*, **8**, 1530 (1935). 22

[57] Gilbert, T. Classics in Magnetics A Phenomenological Theory of Damping in Ferromagnetic Materials. *IEEE Transactions on Magnetics*, **40**, 3443 (2004). 22

[58] Chai, G., Xue, D., Fan, X., Li, X., and Guo, D. Extending the Snoeks limit of single layer film in (Co[sub 96]Zr[sub 4]Cu)[sub n] multilayers. *Applied Physics Letters*, **93**, 152516 (2008). 25, 82, 145

[59] Sabu, T., Kuruvilla, J., Malhotra, S.K., Koichi Goda, M.S., and Sreekala, S. *Polymer Composites, Macro- and Microcomposites*. Wiley (2012). 25

[60] Mossotti, O.F. Mem. di mathem. e fisica in Modena. **24**, 49 (1850). 27

[61] Clausius, R. Die mechanische Ugrmetheorie. **2**, 62 (1879). 27

[62] Saviz, M. and Faraji-Dana, R. A Theoretical Model for the Frequency-Dependent Dielectric Properties of Corneal Tissue at Microwave Frequencies. *Progress In Electromagnetics Research*, **137**, 389 (2013). 28

[63] Simpkin, R. Derivation of Lichtenecker's Logarithmic Mixture Formula From Maxwell's Equations. *IEEE Transactions on Microwave Theory and Techniques*, **58**, 545 (2010). 28

[64] Birchak, J., Gardner, C., Hipp, J., and Victor, J. High dielectric constant microwave probes for sensing soil moisture. *Proceedings of the IEEE*, **62**, 93 (1974). 28

[65] Looyenga, H. Dielectric constants of heterogeneous mixtures. *Physica*, **31**, 401 (1965). 28

[66] Ebara, H., Inoue, T., and Hashimoto, O. Measurement method of complex permittivity and permeability for a powdered material using a waveguide in microwave band. *Science and Technology of Advanced Materials*, **7**, 77 (2006). 30

[67] Nicolson, A. and Ross, G. Measurement of the Intrinsic Properties of Materials by Time-Domain Techniques. *IEEE Transactions on Instrumentation and Measurement*, **19**, 377 (1970). 30, 52, 66, 85, 102, 126

[68] Weir, W. Automatic measurement of complex dielectric constant and permeability at microwave frequencies. *Proceedings of the IEEE*, **62**, 33 (1974). 30, 52, 66, 85, 102, 126

[69] Bragg, W.L. The Diffraction of Short Electromagnetic Waves by a Crystal. *Proceedings of the Cambridge Philosophy Society*, **17**, 43 (1913). 38

[70] Born, M. and Wolf, E. *Principles of optics*. Cambridge University Press (1999). 39

[71] Berthold, C., Klein, R., Lühmann, J., and Nickel, K.G. Characterization of Fibres and Fibre Collectives with Common Laser Diffractometers. *Particle & Particle Systems Characterization*, **17**, 113 (2000). 39

[72] Xu, R. and Di Guida, O.A. Comparison of sizing small particles using different technologies. *Powder Technology*, **132**, 145 (2003). 40

[73] Barry, W. A Broad-Band, Automated, Stripline Technique for the Simultaneous Measurement of Complex Permittivity and Permeability. *IEEE Transactions on Microwave Theory and Techniques*, **34**, 80 (1986). 48, 65, 84, 125

[74] The Maths Work Inc. MATLAB R2012a (2012). 52

[75] J. Baker-Jarvis, E. Vanzurd, W.K. Improved Technique for Determining Complex Permittivity with the Transmission / Reflection Met hod. *IEEE Transactions on Microwave Theory and Techniques*, **38**, 1096 (1990). 52

[76] Smith, D.R., Vier, D.C., Koschny, T., and Soukoulis, C.M. Electromagnetic parameter retrieval from inhomogeneous metamaterials. *Physical Review E*, **71**, 036617 (2005). 52

[77] Chen, X., Grzegorczyk, T.M., Wu, B.I., Pacheco, J., and Kong, J.A. Robust method to retrieve the constitutive effective parameters of metamaterials. *Physical Review E*, **70**, 016608 (2004). 52

[78] The MathWorks Inc. MATLAB R2012a (2012). 54, 126

[79] Ansys Inc. ANSYS HFSS V14 (2011). 54

[80] Dionne, G.F. *Magnetic Oxides*. Springer (2009). 62, 82

[81] Yang, M.C., Xu, B., Cheng, J.H., Pan, C.J., Hwang, B.J., and Meng, Y.S. Electronic, Structural, and Electrochemical Properties of LiNiCu MnO4 High-Voltage Spinel Materials. *Chemistry of Materials*, **23**, 2832 (2011). 62

[82] Schloemann, E.F. Mathematical Models of Microwave Ferrites. *Le Journal de Physique IV*, **07**, 433 (1997).

[83] Globus, A., Pascard, H., and Cagan, V. Distance between magnetic ions and fundamental properties in ferrites. *Le Journal de Physique Colloques*, **38**, 163 (1977).

[84] Mattei, J.L., Bariou, D., Chevalier, A., and Le Floch, M. Gyroresonance in unsaturated composite bodies: Experiments and theory. *Journal of Applied Physics*, **87**, 4975 (2000).

[85] Wohlfarth, E. *Ferromagnetic Materials: A Handbook on the Properties of Magnetically Ordered Substances*, volume 16. Elsevier (1980). 62

[86] Kong, L.B., Li, Z.W., Lin, G.Q., and Gan, Y.B. Ni-Zn Ferrites Composites With Almost Equal Values of Permeability and Permittivity for Low-Frequency Antenna Design. *IEEE Transactions on Magnetics*, **43**, 6 (2007). 62

[87] Ni, S., Wang, X., Zhou, G., Yang, F., Wang, J., and He, D. Designed synthesis of wide range microwave absorption Fe3O4 carbon sphere composite. *Journal of Alloys and Compounds*, **489**, 252 (2010). 62

[88] L. Valko, P. Bucek, R.D. and Ušáková, M. Magnetic properties of ferrite-polymer composites. *Journal of Electrical Engineering*, **54**, 100 (2003). 62

[89] Rekosova, J., Dosoudil, R., Usakova, M., Usak, E., and Hudec, I. Magnetopolymer Composites With Soft Magnetic Ferrite Filler. *IEEE Transactions on Magnetics*, **49**, 38 (2013). 62

[90] Yang, H.B., Lin, Y., and Wang, F. Electromagnetic Property of MnZn Ferrite/SrTiO3/PTFE Composites. *Key Engineering Materials*, **368**, 629 (2008). 62

[91] Youngs, I.J. A geometric percolation model for non-spherical excluded volumes. *Journal of Physics D: Applied Physics*, **36**, 738 (2003). 62

[92] Ebrahimi, F. (editor). *Nanocomposites - New Trends and Developments*. InTech (2012). 63

[93] JOHN, M. and THOMAS, S. Biofibres and biocomposites. *Carbohydrate Polymers*, **71**, 343 (2008). 63

[94] Czaja, W.K., Young, D.J., Kawecki, M., and Brown, R.M. The future prospects of microbial cellulose in biomedical applications. *Biomacromolecules*, **8**, 1 (2007).

[95] Kalka, S., Huber, T., Steinberg, J., Baronian, K., Müssig, J., and Staiger, M.P. Biodegradability of all-cellulose composite laminates. *Composites Part A: Applied Science and Manufacturing*, **59**, 37 (2014). 63

[96] Dimitrov, K.V. Fe3O4 Modification of Microcrystalline Cellulose for Composite Materials. *American Journal of Chemistry*, **5**, 140 (2013). 63

[97] Sun, N., Swatloski, R.P., Maxim, M.L., Rahman, M., Harland, A.G., Haque, A., Spear, S.K., Daly, D.T., and Rogers, R.D. Magnetite-embedded cellulose fibers prepared from ionic liquid. *Journal of Materials Chemistry*, **18**, 283 (2008). 63

[98] Galland, S., Andersson, R.L., Ström, V., Olsson, R.T., and Berglund, L.A. Strong and moldable cellulose magnets with high ferrite nanoparticle content. *ACS applied materials & interfaces*, **6**, 20524 (2014). 63

[99] Rubacha, M. Magnetically active composite cellulose fibers. *Journal of Applied Polymer Science*, **101**, 1529 (2006). 63

[100] Maxwell, J. A treatise on electricity and magnetism (1881). 64

[101] Wagner, K.W. Zur Theorie der unvollkommenen Dielektrika. *Annalen der Physik*, **345**, 817 (1913). 64

[102] Moučka, R., Lopatin, A.V., Kazantseva, N.E., Vilčáková, J., and Sáha, P. Enhancement of magnetic losses in hybrid polymer composites with MnZn-ferrite and conductive fillers. *Journal of Materials Science*, **42**, 9480 (2007). 64

[103] Le Floc'h, M., Loaec, J., Globus, A., and Pascard, H. Effect of the hydrostatic pressure on the coercive force of polycrystalline garnets. *IEEE Transactions on Magnetics*, **17**, 1218 (1981). 69

[104] Javed Iqbal, M., Ahmad, Z., Meydan, T., and Melikhov, Y. Physical, electrical and magnetic properties of nano-sized Co-Cr substituted magnesium ferrites. *Journal of Applied Physics*, **111**, 33906 (2012). 69

[105] Rother, K. and Lichtenecker, K. Die herleitung des logarithmis chen mischungsgesetzes als allegemeinen prinzipien der staionaren stromung. *Physikalische Zeitschrift*, **32**, 255 (1931). 70, 88

[106] Simpkin, R. Derivation of Lichtenecker's Logarithmic Mixture Formula From Maxwell's Equations. *IEEE Transactions on Microwave Theory and Techniques*, **58**, 545 (2010). 70, 88

[107] Neo, C. and Varadan, V. Optimization of Carbon Fiber Composite for Microwave Absorber. *IEEE Transactions on Electromagnetic Compatibility*, **46**, 102 (2004). 71

[108] Birks, J.B. The Measurement of the Permeability of Low-conductivity Ferromagnetic Materials at Centimetre Wavelengths. *Proceedings of the Physical Society*, **60**, 282 (1948). 71

[109] Pitman, K., Lindley, M., Simkin, D., and Cooper, J. Radar absorbers: better by design. *IEE Proceedings F Radar and Signal Processing*, **138**, 223 (1991). 71

[110] Tsutaoka, T., Ueshima, M., Tokunaga, T., Nakamura, T., and Hatakeyama, K. Frequency dispersion and temperature variation of complex permeability of Ni-Zn ferrite composite materials. *Journal of Applied Physics*, **78**, 3983 (1995). 71

[111] Peter Strunk. *Characterisation of cellulose pulps and the influence of their properites on the process and production of viscose and cellulose ethers.*

UmeåUniversity, Faculty of Science and Technology, Department of Chemistry. (2012). 75

[112] Klemm, D., Heublein, B., Fink, H.P., and Bohn, A. Cellulose: fascinating biopolymer and sustainable raw material. *Angewandte Chemie (International ed. in English)*, **44**, 3358 (2005). 75

[113] Le Bras, D., Strø mme, M., and Mihranyan, A. Characterization of Dielectric Properties of Nanocellulose from Wood and Algae for Electrical Insulator Applications. *The journal of physical chemistry. B* (2015). 75

[114] Atsumi, O., Mikami, S., Nitta, K., Shinmura, M., Washizu, S., and Wada, Y. Electrical conduction and polarisation in cellulose. In *Conduction and Breakdown in solid dielectrics*, pages 15–19 (1989). 75

[115] Pinto, R., Neves, M., Neto, C., and Trindade, T. Composites of Cellulose and Metal Nanoparticles. *InTech*, **4**, 73 (2012).

[116] Monroe, D. Water Molecules, Unite! *Focus*, **19**, 19 (2007). 75

[117] PANT, H., PATRA, M., VERMA, A., VADERA, S., and KUMAR, N. Study of the dielectric properties of barium titanatepolymer composites. *Acta Materialia*, **54**, 3163 (2006). 76

[118] Kwei, G.H., Lawson, A.C., Billinge, S.J.L., and Cheong, S.W. Structures of the ferroelectric phases of barium titanate. *The Journal of Physical Chemistry*, **97**, 2368 (1993). 76

[119] Moučka, R., Lopatin, A.V., Kazantseva, N.E., Vilčáková, J., and Sáha, P. Enhancement of magnetic losses in hybrid polymer composites with MnZn-ferrite and conductive fillers. *Journal of Materials Science*, **42**, 9480 (2007). 77

[120] Kasagi, T., Tsutaoka, T., and Hatakeyama, K. Complex Permeability of PermalloyFerrite Hybrid Composite Materials. *Journal of Magnetism and Magnetic Materials*, **272-276**, 2224 (2004).

[121] Babayan, V., Kazantseva, N., Sapurina, I., Moučka, R., Stejskal, J., and Sáha, P. Increasing the high-frequency magnetic permeability of MnZn ferrite in polyaniline composites by incorporating silver. *Journal of Magnetism and Magnetic Materials*, **333**, 30 (2013).

[122] Bespyatykh, Y. and Kazantseva, N. Electromagnetic properties of hybrid polymer composites. *Journal of Communications Technology and Electronics*, **53**, 143 (2011).

[123] Gheisari, K., Javadpour, S., Shokrollahi, H., and Hashemi, B. Magnetic losses of the soft magnetic composites consisting of iron and NiZn ferrite. *Journal of Magnetism and Magnetic Materials*, **320**, 1544 (2008).

[124] Dosoudil, R., Franek, J., Slama, J., Usakova, M., and Gruskova, A. Electromagnetic Wave Absorption Performances of Metal Alloy/Spinel Ferrite/Polymer Composites. *IEEE Transactions on Magnetics*, **48**, 1524 (2012). 77

[125] Elimat, Z.M., Zihlif, A.M., and Ragosta, G. Study of ac electrical properties of aluminiumepoxy composites. *Journal of Physics D: Applied Physics*, **41**, 165408 (2008). 78

[126] Singh, V., Kulkarni, A.R., and Rama Mohan, T.R. Dielectric properties of aluminum-epoxy composites. *Journal of Applied Polymer Science*, **90**, 3602 (2003). 79

[127] Tyc, T. and Leonhardt, U. Non-Euclidean Cloaking for Light Waves. *IEEE Journal of Selected Topics in Quantum Electronics*, **16**, 418 (2010). 82, 145

[128] Lagarkov, A. and Rozanov, K. High-frequency behavior of magnetic composites. *Journal of Magnetism and Magnetic Materials*, **321**, 2082 (2009). 82

[129] Acher, O. and Dubourg, S. Generalization of Snoeks law to ferromagnetic films and composites. *Physical Review B*, **77**, 104440 (2008). 82, 83

[130] Dosoudil, R., Usakova, M., Franek, J., Slama, J., and Gruskova, A. Particle Size and Concentration Effect on Permeability and EM-Wave Absorption Properties of Hybrid Ferrite Polymer Composites. *IEEE Transactions on Magnetics*, **46**, 436 (2010). 83

[131] Dosoudil, R., M. Ušáková, A.G., and Sláma, J. Complex permeability of LiZn/MnZn/PVC composite materials. *Acta Phys. Pol. A*, **118**, 1049 (2010). 83

[132] Sláma, J., Ušák, E., Dosoudil, R., Grusková, A., Ušáková, M., and Jan, V. The influence of particle size and substituent contents on the magnetic properties of Be or Cu substituted NiZn ferrites. pages 362–364 (2006). 83

[133] Li, B., Shen, Y., Yue, Z., and Nan, C. Influence of particle size on electromagnetic behavior and microwave absorption properties of Z-type Ba-ferrite/polymer composites. *Journal of Magnetism and Magnetic Materials*, **313**, 322 (2007). 83

[134] Uestuener, K., Katter, M., and Rodewald, W. Dependence of the Mean Grain Size and Coercivity of Sintered Nd, Fe & B Magnets on the Initial Powder Particle Size. *IEEE Transactions on Magnetics*, **42**, 2897 (2006). 86

[135] Bance, S., Seebacher, B., Schrefl, T., Exl, L., Winklhofer, M., Hrkac, G., Zimanyi, G., Shoji, T., Yano, M., Sakuma, N., Ito, M., Kato, A., and Manabe, A. Grain-size dependent demagnetizing factors in permanent magnets. *Journal of Applied Physics*, **116**, 233903 (2014). 86

[136] Cullity, B.D. and Graham, C.D. *Introduction to Magnetic Materials*. Wiley (2011). 86

[137] Khan, K., Maqsood, A., Rehman, M., Malik, M.A., and Akram, M. Structural, Dielectric, and Magnetic Characterization of Nanocrystalline NiCo Ferrites. *Journal of Superconductivity and Novel Magnetism*, **25**, 2707 (2011). 98, 104

[138] Thakur, A., Chevalier, A., Mattei, J.L., and Queffelec, P. Low-loss spinel nanoferrite with matching permeability and permittivity in the ultrahigh frequency range. *Journal of Applied Physics*, **108**, 014301 (2010). 98

[139] Liang, K., Tang, X., Wei, B., and Hu, W. Fabrication and characterization of a nanoporous NiO film with high specific energy and power via an electrochemical dealloying approach. *Materials Research Bulletin*, **48**, 3829 (2013). 99

[140] Kärkkäinen, M. and Ikonen, P. Patch antenna with stacked split-ring resonators as an artificial magneto-dielectric substrate. *Microwave and Optical Technology Letters*, **46**, 554 (2005). 99

[141] Alitalo, P., Luukkonen, O., Vehmas, J., and Tretyakov, S. Impedance-Matched Microwave Lens. *IEEE Antennas and Wireless Propagation Letters*, **7**, 187 (2008). 99

[142] Landy, N., Sajuyigbe, S., Mock, J., Smith, D., and Padilla, W. Perfect Metamaterial Absorber. *Physical Review Letters*, **100**, 207402 (2008). 99

[143] Kim, K.H. and Park, Q.H. Perfect anti-reflection from first principles. *Scientific reports*, **3**, 1062 (2013). 99

[144] Rayleigh, L. On The Instability Of Jets. *Proceedings of the London Mathematical Society*, **s1-10**, 4 (1878). 99

[145] Matsumoto, M. and Miyata, Y. Thin electromagnetic wave absorber for quasi-microwave band containing aligned thin magnetic metal particles. *IEEE Transactions on Magnetics*, **33**, 4459 (1997). 99

[146] Parke, L., Hooper, I.R., Hicken, R.J., Dancer, C.E.J., Grant, P.S., Youngs, I.J., Sambles, J.R., and Hibbins, A.P. Heavily loaded ferrite-polymer composites to produce high refractive index materials at centimetre wavelengths. *APL Materials*, **1**, 042108 (2013). 102

[147] Ansoft. www.ansoft.com/products/hf/hfss/., Ansoft Corporation, Ansoft HFSS, Pittsburgh, PA. [Online]. (1989). 104

[148] Xiong, X., Xue, Z.H., Meng, C., Jiang, S.C., Hu, Y.H., Peng, R.W., and Wang, M. Polarization-dependent perfect absorbers/reflectors based on a three-dimensional metamaterial. *Physical Review B*, **88**, 115105 (2013). 108

[149] Li, H., Yuan, L.H., Zhou, B., Shen, X.P., Cheng, Q., and Cui, T.J. Ultrathin multiband gigahertz metamaterial absorbers. *Journal of Applied Physics*, **110**, 014909 (2011).

[150] Landy, N., Sajuyigbe, S., Mock, J., Smith, D., and Padilla, W. Perfect Metamaterial Absorber. *Physical Review Letters*, **100**, 207402 (2008).

[151] Meng, L., Zhao, D., Li, Q., and Qiu, M. Polarization-sensitive perfect absorbers at near-infrared wavelengths. *Optics express*, **21 Suppl 1**, A111 (2013).

[152] Huang, L., Chowdhury, D.R., Ramani, S., Reiten, M.T., Luo, S.N., Taylor, A.J., and Chen, H.T. Experimental demonstration of terahertz metamaterial absorbers with a broad and flat high absorption band. *Optics letters*, **37**, 154 (2012).

[153] Tao, H., Bingham, C.M., Pilon, D., Fan, K., Strikwerda, A.C., Shrekenhamer, D., Padilla, W.J., Zhang, X., and Averitt, R.D. A dual band terahertz metamaterial absorber. *Journal of Physics D: Applied Physics*, **43**, 225102 (2010). 108

[154] Shin, J., Shen, J., and Fan, S. Three-Dimensional Metamaterials with an Ultrahigh Effective Refractive Index over a Broad Bandwidth. *Physical Review Letters*, **102**, 1 (2009). 121, 123

[155] Thakur, A., Chevalier, A., Mattei, J., and Queffelec, P. Low-loss spinel nanoferrite with matching permeability and permittivity in the ultrahigh frequency range. *Journal of Applied Physics*, **108**, 014301 (2010). 122

[156] Chen, H., Chan, C.T., and Sheng, P. Transformation optics and metamaterials. *Nature materials*, **9**, 387 (2010). 122

[157] Wood, B. and Pendry, J.B. Metamaterials at zero frequency. *Journal of Physics: Condensed Matter*, **19**, 076208 (2007). 122

[158] Njoku, C.C., Whittow, W.G., and Vardaxoglou, J.C. Effective Permittivity of Heterogeneous Substrates With Cubes in a 3-D Lattice. *IEEE Antennas and Wireless Propagation Letters*, **10**, 1480 (2011). 122

[159] Lapine, M., Krylova, A., Belov, P., Poulton, C., McPhedran, R., and Kivshar, Y. Broadband diamagnetism in anisotropic metamaterials. *Physical Review B*, **87**, 024408 (2013). 122

[160] Belov, P.A., Slobozhanyuk, A.P., Filonov, D.S., Yagupov, I.V., Kapitanova, P.V., Simovski, C.R., Lapine, M., and Kivshar, Y.S. Broadband isotropic μ-near-zero metamaterials. *Applied Physics Letters*, **103**, 211903 (2013). 123

[161] Campbell, T., Hibbins, A., Sambles, J., and Hooper, I. Broadband and low loss high refractive index metamaterials in the microwave regime. *Applied Physics Letters*, **102**, 091108 (2013). 123, 126

[162] Ansys Inc. ANSYS HFSS V14 (2011). 128

[163] Hibbins, A.P., Lockyear, M.J., and Sambles, J.R. Coupled surface-plasmon-like modes between metamaterial. *Physical Review B*, **76**, 165431 (2007). 128

[164] Leonhardt, U. Optical conformal mapping. *Science*, **312**, 1777 (2006). 145

[165] Leonhardt, U. and Philbin, T.G. General relativity in electrical engineering. *New Journal of Physics*, **8**, 247 (2006). 145

[166] Song, N.N., Yang, H.T., Liu, H.L., Ren, X., Ding, H.F., Zhang, X.Q., and Cheng, Z.H. Exceeding natural resonance frequency limit of monodisperse Fe(3)O(4) nanoparticles via superparamagnetic relaxation. *Scientific reports*, **3**, 3161 (2013). 145, 146

[167] Aliuzzaman, M., Haque, M.M., Ferdous, M.J., Hoque, S.M., and Hakim, M.A. Effect of Sintering Time on the Structural, Magnetic and Electrical Transport Properties of Mg0.35Cu0.20Zn0.45Fe1.94O4 Ferrites. *World Journal of Condensed Matter Physics*, **04**, 13 (2014). 145

[168] Abshinova, M.A., Lopatin, A.V., Kazantseva, N.E., Vilčáková, J., and Sáha, P. Correlation between the microstructure and the electromagnetic properties of carbonyl iron filled polymer composites. *Composites Part A: Applied Science and Manufacturing*, **38**, 2471 (2007). 146

[169] Kärkkäinen, M. and Ikonen, P. Patch antenna with stacked split-ring resonators as an artificial magneto-dielectric substrate. *Microwave and Optical Technology Letters*, **46**, 554 (2005). 149

[170] Kamenetskii, E.O., Sigalov, M., and Shavit, R. Tellegen particles and magnetoelectric metamaterials. *Journal of Applied Physics*, **105**, 013537 (2009). 149

[171] Kamenetskii, E.O., Joffe, R., Berezin, M., Vaisman, G., and Shavit, R. Magnetic-Dipolar-Mode oscillations for near- and far-field manipulation of microwave radiation. *Progress In Electromagnetics Research B*, **56**, 51 (2013).

[172] Sigalov, M., Kamenetskii, E.O., and Shavit, R. Magnetic-dipolar and electromagnetic vortices in quasi-2D ferrite discs. *Journal of Physics. Condensed matter : an Institute of Physics Journal*, **21**, 016003 (2009). 149